CHALMERS
UNIVERSITY OF TECHNOLOGY

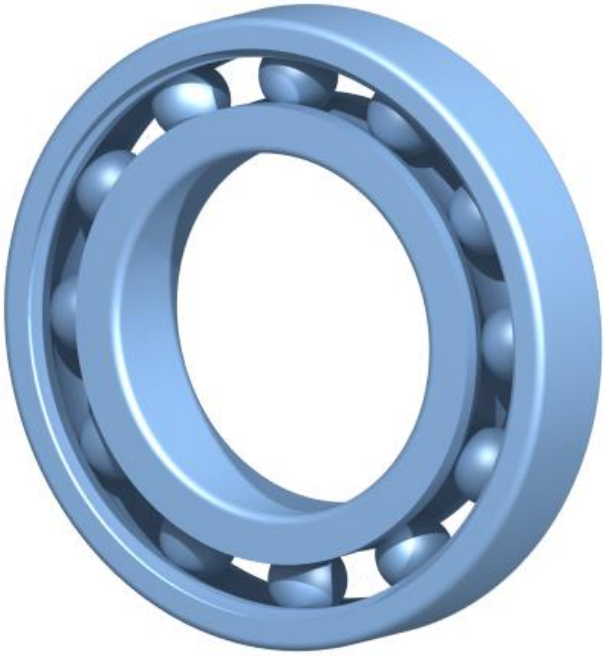

Abaqus Based Modelling of Ball Bearings

Master's thesis in Applied Mechanics

Arvid Angel
Jonathan Cederquist

DEPARTMENT OF INDUSTRIAL AND MATERIALS SCIENCE

CHALMERS UNIVERSITY OF TECHNOLOGY
Gothenburg, Sweden 2025
www.chalmers.se

MASTER'S THESIS 2025

Abaqus Based Modelling of Ball Bearings

ARVID ANGEL
JONATHAN CEDERQUIST

CHALMERS

Department of Industrial and Materials Science
Division of Material and Computational Mechanics
CHALMERS UNIVERSITY OF TECHNOLOGY
Göteborg, Sweden 2025

Abaqus Based Modelling of Ball Bearings
ARVID ANGEL
JONATHAN CEDERQUIST

Supervisor: Sven Norberg, Volvo Group Trucks Technology
Examiner: Magnus Ekh, Department of Industrial and Materials Science

Master's Thesis 2025
Department of Industrial and Materials Science
Division of Material and Computational Mechanics
Chalmers University of Technology
SE-412 96 Göteborg
Sweden
Telephone +46 (0)31-772 1000

Cover: Render of General Deep Groove Ball Bearing

Typeset in LaTeX
Printed by Chalmers Reproservice
Göteborg, Sweden 2025

Key words: axial, radial, ball bearing, spring, stiffness displacement

Abstract

This thesis investigates whether deep groove ball bearings can be accurately modeled in Abaqus by replacing rolling elements with non-linear springs. The main focus is on the transfer of radial, axial, and combined loads. Existing analytical stiffness models, such as those by Harris and Hamrock, were found inadequate for general use, prompting the development of a new stiffness model. This was achieved through a curve-fitting approach that correlates bearing geometry (e.g., ball diameter, pitch diameter, number of balls, radial play) with displacement data from reference simulations derived using the commercial gearbox software SABR. The final model showed an error margin of less than 5% for most load cases and misalignments. The outcome suggests that this method provides a flexible and accurate tool for simulating bearing stiffness, with potential for broader implementation and further refinement.

Acknowledgments

We would like to express our gratitude for the support and expertise provided by our supervisors, Sven Norberg and Erik Mc Guinness, at Volvo Group Trucks Technology, PE Driveline.

We also appreciate group manager Maria Petersson for giving us this opportunity and her assistance throughout the project.

Finally, we thank Professor Magnus Ekh from the Department of Industrial and Materials Science at Chalmers University of Technology for his insights and feedback, which guided us throughout this project.

Contents

List of Figures

List of Tables

Notations

Table 1: Table of Notations

Symbol	Description
$\alpha_{i,o}$	Radius ratio
$a^\star$	Dimensionless semimajor axis of contact ellipse
a, b	Semi-major and minor axes of elliptic area
$a^\star$	Dimensionless semimajor axis of contact ellipse
β	Contact angle
$b^\star$	Dimensionless semiminor axis of contact ellipse
$C3D20$	Second order, 20-node brick element
$CCL12$	First order, 12-node cylindrical element
$CCL24R$	Second order, 24-node cylindrical element with reduced integration
C	Dynamic Load Rating
$CG_{i,o}$	Curvature gain
$c_{i,o}$	Raceway's center point radially
δ	Deflection
$\delta^\star$	Dimensionless contact deformation
D	Ball diameter
D_m	Mean raceway diameter for inner and outer ring
D_0	Outside diameter
d	Roller diameter
d_1	Bearing shoulder diameter
d_m	Bearing pitch diameter
$\mathcal{E}(\kappa)$	Elliptic integral of the second kind
$\bar{\mathcal{E}}(\kappa)$	Approximate elliptic integral of the second kind
E	Modulus of elasticity
E'	Equivalent modulus of elasticity
$e_{i,o}$	Eccentricity of raceway centers
$\mathcal{F}(\kappa)$	Elliptic integral of the first kind
$\bar{\mathcal{F}}(\kappa)$	Approximate elliptic integral of the first kind
$F(\rho)$	Curvature difference
F_i	Inner race load
F_o	Outer race load
$f_{i,o}$	Raceway conformity's
γ	$= \frac{D\cos(\beta)}{d_m}$, dimensionless parameter

Symbol	Description
IR	Inner ring of the bearing
κ	Elongation of elliptic contact area
K_p	Ball stiffness
L_e	Effective length of roller (roller length minus edge radius)
N	Number of rolling elements
OR	Outer ring of the bearing
ψ	Azimuth angle
ρ	Curvature
$\sum \rho$	Curvature sum
P_d	Diametrical clearance
Q	Force
R	Equivalent radius
$R_{x,y}$	Curvature radii, x: lateral direction, y: rolling direction
r	Ball radius
$r_{i,o}$	Raceway radius
σ	Stress
σ_0	Stress at the center of contact
s_{sets}	Spring sets (Springs per ball circumferentially)
sp_{sets}	Springs per set (Springs per ball axially)
sp_b	Springs per ball ($s_{sets} \cdot sp_{sets}$)
θ	Roller element position in bearing
ν	Poisson's ratio
x	Distance along roller length
y	Rolling direction

Introduction

Transportation is a cornerstone of modern life. Society relies on goods and people being delivered with efficiency and reliability across the globe. Heavy trucks play a significant role in this regard, and their systems must undergo continuous development to meet modern demands. Bearings are critical components in these systems, facilitating rotation and supporting loads in gearboxes and drivelines.

At Volvo Group, finite element (FE) models of bearings have been developed over the years to improve the accuracy of stress and force distribution predictions. These models are used to optimize the performance of driveline components. It is crucial that the bearing models predict forces and stress distributions accurately when a gearbox assembly is simulated.

1.1 Background

The transmission simulation team at Volvo Group Trucks Technology (GTT) uses the finite element software Abaqus (n.d.) to model and simulate their gearboxes. The bearings used for modeling are generated using an in-house Matlab (n.d.) program including an intuitive graphical user interface (GUI) called Lincoln.

Ball bearings tend to be used more extensively in gearboxes coupled with electric machines as they cope better with high speeds. In contrast, for conventional drivelines with combustion engines, gearboxes are designed primarily with cylindrical and tapered roller bearings, which has led to a situation where the current Lincoln and Abaqus set up for ball bearings is not as mature as the models for roller bearings. As electric drivetrain volumes are increasing, the need for accurate ball bearing models has increased. See figure 1.1 for a generic deep groove ball bearing.

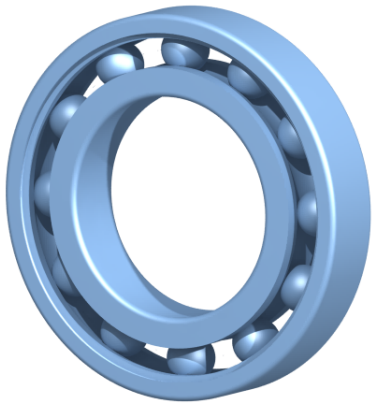

(a) SKF 6216 deep groove ball bearing illustrated from an ISO perspective. Rendered in CATIA v5.

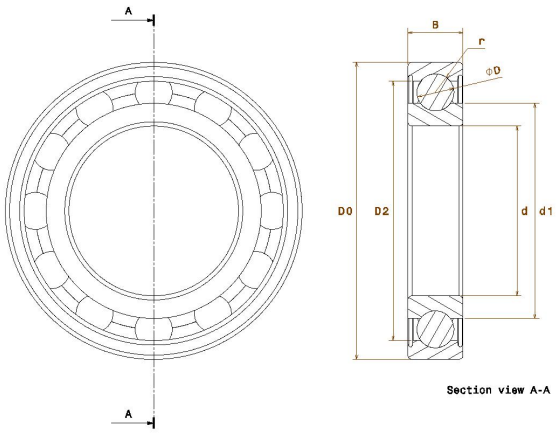

(b) Drawing of deep groove ball bearing with a section cut highlighting the essential geometry measurements.

Figure 1.1: Example of a Deep Groove Ball Bearing

1.2 Aim

The objective of this thesis work is to develop a ball bearing model that can accurately describe the behavior of bearings and provide detailed FE results of the bearings' seats. This includes investigating different methods of modeling deep groove ball bearings with Abaqus and identifying the methods that work satisfactorily for different load cases, e.g., pure radial load, radial load combined with axial load, and different types of misalignment between the inner and outer rings. The results of the derived models will be compared with results from a commercial gearbox software, called SABR (n.d.). The goal is to identify the factors that influence the behavior and to generalize the modeling parameters for bearings of different geometries.

1.3 Limitations

The results of the derived models will not be compared with a detailed finite element analysis (FEA) with solid modeling of the rolling elements. Furthermore, no physical tests will be conducted as the construction work required for building the test bench and verification of the results would be too extensive.

1.4 Specification of the Issue being Investigated

The following questions will be addressed throughout the course of this thesis work:

- First, is it possible to accurately model deep groove ball bearings using a set of linear or non-linear springs?
- If so, is this true for radial, axial, and combined loads with various misalignments?
- Finally, is it possible to find a generalized model that can be used for various sizes and geometries of deep groove ball bearings?

Theory

This chapter describes the fundamentals of deep groove ball bearing geometry. It presents the principles of Hertz contact theory and the mechanics of bearing contact stresses and deformations followed by two different load deflection relationships defined by Harris and Hamrock, respectively. The chapter concludes with a review of the modeling of springs in Abaqus. Table 2.1 contains notations relevant for this chapter.

Table 2.1: Table of Relevant Notation

Symbol	Description
α	Contact Angle
a, b	Semi-major and minor axes of elliptic area
$a^\star$, $b^\star$	Dimensionless semimajor/semiminor axis of contact ellipse
$CG_{i,o}$	Curvature gain
$c_{i,o}$	Raceway's center point radially
δ	Deflection
$\delta^\star$	Dimensionless contact deformation
D	Ball diameter
d_m	Pitch diameter
$\mathcal{E}(\kappa)$	Elliptic integral of the second kind
$\bar{\mathcal{E}}(\kappa)$	Approximate elliptic integral of second kind
E	Modulus of elasticity
E'	Equivalent modulus of elasticity
$e_{i,o}$	Eccentricity of raceway centers
$\mathcal{F}(\kappa)$	Elliptic integral of the first kind
$\bar{\mathcal{F}}(\kappa)$	Approximate elliptic integral of first kind
$F(\rho)$	Curvature difference
f_i, f_o	Raceway conformity's
γ	$= \frac{D\cos\alpha}{d_m}$, dimensionless parameter
κ	Elongation of elliptic contact area
K_p	Ball stiffness
ψ	Azimuth angle
ρ	Curvature
$\sum \rho$	Curvature sum
P_d	Diametrical clearance
Q	Force
R	Equivalent radius
$R_{x,y}$	Curvature radii, x: lateral direction, y: rolling direction
r	Ball radius
$r_{i,o}$	Raceway groove curvature radius
σ_0	Stress at the center of contact
ν	Poisson's ratio

2.1 Macrogeometry of Ball Bearings

A comprehensive understanding of the geometry of a deep groove ball bearing is necessary to ensure that it is modeled correctly. The subsequent section details raceway conformity, raceway radius, raceway center, and "play."

Raceway conformity $f_{i,o}$, detailed in equation 2.1, is closely tied to the contact stresses a ball experiences under load. It is the dimensional relationship between the radius of the raceways $r_{i,o}$ and the diameter of the ball D, with indices o and i referring to the outer and inner raceway, respectively.

$$f_{i,o} = \frac{r_{i,o}}{D} \tag{2.1}$$

A "perfect" fit between ball and raceway would require a conformity of 0.5, meaning the radius of the raceway is the same as the ball radius. According to Harris (2001, p.50) and Brändlein et al. (1985, p.215) a conformity of 0.5 provides optimal load carrying capacity but can lead to high friction torque and differential slip (sliding) of the ball. Therefore, raceways are typically designed with a ball conformity between 0.51 and 0.54, see figure 2.1.

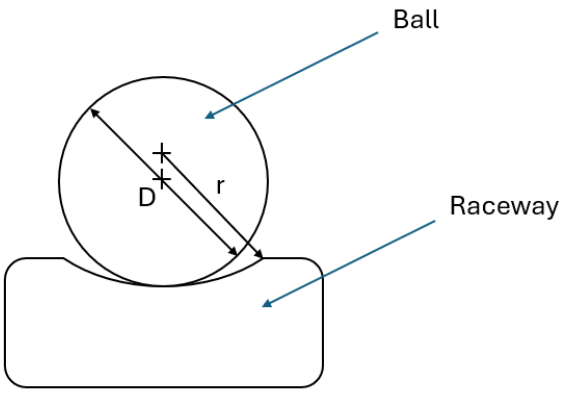

Figure 2.1: Conformity of an inner raceway visualizing the ball diameter and the inner ring radius, from their respective center points.

To achieve a conformity rating greater than 0.5, it is necessary to increase the radii of both the inner and outer rings beyond that of the ball radius, as illustrated in figure 2.1. The raceway radius is calculated by multiplying the ball radius by the curvature gain:

$$r_{i,o} = r \cdot CG_{i,o} \tag{2.2}$$

For example, if a bearing has an outer curvature gain of 6% and the ball radius is 10 mm, the raceway radius will be $r_o = r \cdot CG_o = 10 \cdot 1.06 = 10.6\ [mm]$. With the equation for $r_{i,o}$ the equation for conformity can be rewritten as the following:

$$f_{i,o} = \frac{r_{i,o}}{D} = \frac{r \cdot CG_{i,o}}{D} = \frac{r \cdot CG_{i,o}}{2 \cdot r} = \frac{CG_{i,o}}{2} \tag{2.3}$$

Additionally, there is a slight offset between the ball center and the ring centers when the ball is in contact with the raceways, which is due to the difference in radius between the two shapes. The deviation from the ball's center point is referred to as "eccentricity,"

which can be calculated using the two radii and any potential gap between the ball and the raceway:

$$e_{i,o} = r_{i,o} - r - \frac{P_d}{4} \tag{2.4}$$

The center of the groove of the inner and outer raceway is calculated from the pitch diameter plus or minus their respective eccentricity.

$$c_{i,o} = d_m \pm e_{i,o} \tag{2.5}$$

The gap between the ball and the raceway at any point along the raceway is referred to as "play" and the play tangent to the radial direction of the bearing through both sides of the rings is referred to as diametrical clearance or P_d. It can be calculated as the diameter to the outer raceway minus the diameter to the inner raceway minus ball diameters times two, see equation 2.6 and figure 2.2:

$$P_d = D2 - D1 - D * 2 \tag{2.6}$$

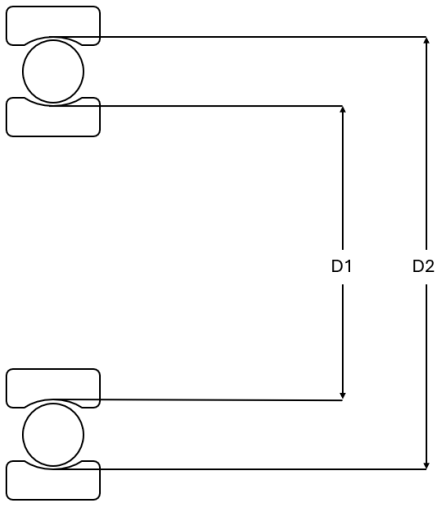

Figure 2.2: Visualization of diametrical clearance with the diameter to the inner and outer raceway marked as D1 and D2.

As noted by both Harris and Brändlein, this gap is necessary to reduce slip and friction. It also allows for misalignment of the rings under no load (Harris, 2001, p.58). Conversely, an excessively large diametrical clearance may result in shocks under vibrations, which can cause damage to balls and raceways. To mitigate this risk, a small radial preload is often applied by e.g. removing the clearance during bearing assembly. Applying radial preload results in more balls under radial load, reducing the maximum rolling element load and prevents skidding (Harris, 2001, p.375).

2.1.1 Effective Clearance

It is important to note that the diametrical clearance provided by the bearing manufacturer changes once the bearing is installed in its intended location. This is due to the fit between the house, shaft, and their respective raceway, as well as temperature differences

between the two rings. The clearance when the bearing is in use is known as effective clearance. All models in this thesis work are modeled using the effective clearance as stated by the commercial gearbox modeling software SABR. Effective diametrical clearance for all bearings used in this report can be found in appendix E.

2.2 Contact Stresses and Deformations

One of the first researching contact theory was Heinrich Hertz. At 23 years of age, he presented his theory describing the contact condition between two half spheres which can be applied to bearings as they are designed to transmit loads from one raceway to another through rolling elements. The magnitude of the load carried by a rolling element is determined by the internal geometry of the bearing and its position at any given moment. Hertz contact theory has been used as foundation for research and development of bearings (NE Nationalencyklopedin AB, n.d.). This section details the method for calculating the load-deflection relationship for the rolling-element-race contact initially established by Hertz and later refined by Harris and Hamrock, among others.

2.2.1 Harris Load Deflection Relationships

Harris (2001) describes the mechanical behavior of point contact between two contacting surfaces as seen in figure 2.3.

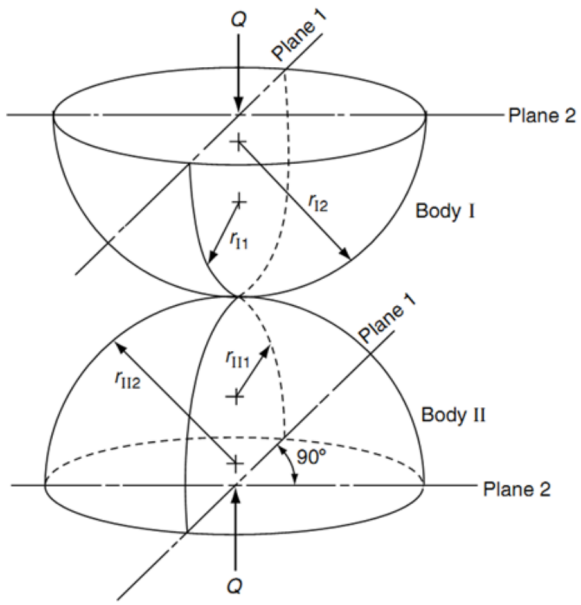

Figure 2.3: Point Contact of two Contacting Bodies. Whilst the radius is always positive, curvatures may be positive or negative depending on if it is a concave or convex surface (Harris, 2001).

The curvature sum describes the overall curvature of the bearing raceway profile and is crucial for calculating the contact dimensions and stiffness. Furthermore, the curvature difference describes how well the two contacting surfaces conform to each other. A large

difference implies point contact and conversely, a small curvature difference implies a larger contact area essentially leading to better conformity. Harris (2001) defines the curvature sum and curvature difference in equation 2.7 and 2.8 below, respectively.
Curvature sum:

$$\sum \rho = \frac{1}{r_{11}} + \frac{1}{r_{12}} + \frac{1}{r_{21}} + \frac{1}{r_{22}} \tag{2.7}$$

Curvature difference:

$$F(\rho) = \frac{(\rho_{11} - \rho_{12}) + (\rho_{21} - \rho_{22})}{\sum \rho} \tag{2.8}$$

Whilst the ball geometry is symmetric, the curvatures of the inner and outer raceway are asymmetric as they differ from each other. The inner and outer contact areas are therefore calculated separately. Harris (2001) explains that the inner and outer raceway contact can be described as follows. Inner raceway contact:

$$\rho_{11} = \rho_{12} = \frac{2}{D}$$
$$\rho_{21} = \frac{2}{D}\Big(\frac{\gamma}{1-\gamma}\Big)$$
$$\rho_{22} = -\frac{1}{f_i D}$$
$$\Downarrow$$

$$\sum \rho_i = \frac{1}{D}\Big(4 - \frac{1}{f_i} + \frac{2\gamma}{1-\gamma}\Big) \tag{2.9}$$

$$F(\rho)_i = \frac{\frac{1}{f_i} + \frac{2\gamma}{1-\gamma}}{4 - \frac{1}{f_i} + \frac{2\gamma}{1-\gamma}} \tag{2.10}$$

γ is the ratio between ball diameter D and the pitch diameter d_m times the cosine of the angle of contact $cos(\beta)$, $\gamma = \frac{Dcos(\beta)}{d_m}$. In this project only bearings with a contact angle of zero will be investigated i.e, $\beta = 0^o$. ρ_{11} and ρ_{12} represent the ball curvature and they are equal in both axial and rolling direction. ρ_{21} represent the raceway curvature in rolling direction and ρ_{22} describes the raceway curvature in axial direction. As the raceway groove is concave, ρ_{22} has a negative sign. Note that $F(\rho)_i$ is a dimensionless parameter describing the curvature difference between the ball and raceway, which is used for bearing stiffness calculations at a later stage.

The outer raceway contact is described similarly to the inner contact but with an opposite sign at ρ_{21} as the geometry is flipped:

$$\rho_{11} = \rho_{12} = \frac{2}{D}$$
$$\rho_{21} = -\frac{2}{D}\Big(\frac{\gamma}{1+\gamma}\Big)$$
$$\rho_{22} = -\frac{1}{f_0 D}$$
$$\Downarrow$$

$$\sum \rho_o = \frac{1}{D}\Big(4 - \frac{1}{f_o} - \frac{2\gamma}{1+\gamma}\Big) \tag{2.11}$$

$$F(\rho)_o = \frac{\frac{1}{f_o} - \frac{2\gamma}{1+\gamma}}{4 - \frac{1}{f_o} - \frac{2\gamma}{1+\gamma}} \tag{2.12}$$

Harris (2001, p.235) describes the stiffness of a steel ball bearing as:

$$K_p = 2.15 \cdot 10^5 \sum \rho^{-1/2} (\delta^*)^{-3/2} \tag{2.13}$$

Where K_p is the bearing stiffness and δ^* is a dimensionless contact parameter (see appendix A). The load deflection relationship is determined as:

$$Q = K_p \cdot \delta^{3/2} \tag{2.14}$$

The load-deflection relationship stated in equation 2.14 is used in various attempts described in section 3.8.1. Other

2.2.2 Hamrock's Load Deflection Relationships

The deformation within the contact is a function of, among other things, the ellipticity parameters and the elliptic integral of the first and second kind. The following simplified expressions facilitate straightforward calculations of stresses and deformations by leveraging the applied load, material properties, and the geometry of the contacting elements.

According to Hamrock (1983, p.17), the contact area expands when two elastic bodies come into contact due to an applied load. In the case of the two solids depicted in figure 2.3, the resulting shape of the contact area will be elliptic and the equations for the curvature radii R_x and R_y are stated in table 2.2.

Table 2.2: Definition of Curvature Radii

	Inner raceway	**Outer raceway**
R_x	$R_{xi} = \frac{(1-\gamma)D}{2}$	$R_{xo} = \frac{(1+\gamma)D}{2}$
R_y	$R_{yi} = \frac{f_i D}{(2f_i - 1)}$	$R_{yo} = \frac{f_o D}{(2f_o - 1)}$

According to Hamrock (1983, p.11) the equivalent radius, R as seen in equation 2.15, is an important factor in contact stress and deformation analysis, as will be shown later in this chapter.

$$R = \frac{1}{\frac{1}{R_x} + \frac{1}{R_y}} \tag{2.15}$$

A key parameter in the process of solving for the Hertzian contact stresses is the shape of the elliptic contact area κ :

$$\kappa = \frac{a}{b} \tag{2.16}$$

With "a" and "b" being the semi-major and semi-minor axes of the elliptic area.

The contact pressure at the center of an elliptical area is:

$$\sigma_0 = -\frac{3Q}{2\pi ab} \tag{2.17}$$

According to equation 2.17, the stress at the center decreases if the contact area increases, i.e., if "a" and "b" increases, and vice versa. This is due to the fact that the force is distributed across a larger surface. The increase in contact area is an effect of deformation of the two contacting bodies, see figure 2.4.

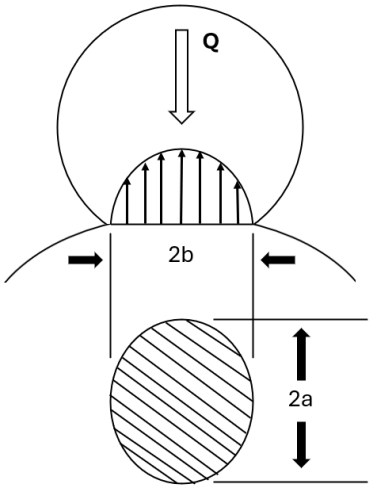

Figure 2.4: Visualization of Hertzian pressure distribution, deformation, and the contacting bodies elliptic contact area. Please not that the contact surface between the two bodies is not flat.

The standard Hertzian solution necessitates the calculation of the ellipticity parameter kappa and the two elliptic integral functions $\mathcal{F}$ and $\mathcal{E}$.

$$\mathcal{F} = \int_0^{\pi/2} \left[1 - \left(1 - \frac{1}{\kappa^2}\right) sin^2\psi\right]^{-1/2} d\psi \tag{2.18}$$

$$\mathcal{E} = \int_0^{\pi/2} \left[1 - \left(1 - \frac{1}{\kappa^2}\right) sin^2\psi\right]^{1/2} d\psi \tag{2.19}$$

The issue with these equations is that they require a solution to a transcendental equation involving κ, $\mathcal{F}$, $\mathcal{E}$, and the geometry of the contacting solids. This means that they must be solved using numerical techniques or approximations. There are a number of approaches to solving this issue. One way, as described by Brewe and Hamrock (1982), is to use simplified expressions of kappa and the two integral functions by expressing them as functions of geometry. This was only possible after obtaining some reference results by using iterative methods as described in the work of Hamrock and Anderson (1973) or using charts as described by Jones (1946). Table 2.3 compares various curvature ratios ρ and their respective κ, $\mathcal{F}$, and $\mathcal{E}$ values, which are the result of the numerical approach used in Hamrock and Anderson (1973). Using a linear regression method, Brewe and Hamrock (1982) came up with the simplified equation for κ seen in equation 2.20.

$$\bar{\kappa} = \alpha^{2/\pi} \tag{2.20}$$

where α represents the radius ratio:

$$\alpha = \frac{R_y}{R_x} \tag{2.21}$$

Due to the asymptotic behavior of the two integrals, an inverse logarithmic approach was applied, resulting in the following two equations:

$$\bar{\mathcal{F}} = \frac{\pi}{2} + q \cdot ln(\alpha) \tag{2.22}$$

$$\bar{\mathcal{E}} = 1 + \frac{q}{\alpha} \tag{2.23}$$

With:

$$q = \frac{\pi}{2} - 1 \tag{2.24}$$

The resulting curve fit values are also presented in table 2.3 along with an error comparison of the simplified approach vs. the numerical approach.

Table 2.3: Comparison of Numerically Determined Values with Curve-Fit Values, from (Hamrock, 1983, p.52)

Radius-of-curvature ratio, α	Ellipticity parameter, κ			Complete elliptic integral of first kind			Complete elliptic integral of second kind		
	κ	$\bar{\kappa}$	Percent error, e	$\mathcal{F}$	$\bar{\mathcal{F}}$	Percent error, e	$\mathcal{E}$	$\bar{\mathcal{E}}$	Percent error, e
1.00	1.00	1.00	0.00	1.57	1.57	0.00	1.57	1.57	0.00
1.25	1.16	1.15	0.66	1.69	1.69	-0.50	1.46	1.46	0.52
1.50	1.31	1.29	1.19	1.79	1.80	-0.70	1.39	1.38	0.76
1.75	1.45	1.43	1.61	1.88	1.89	-0.75	1.34	1.33	0.87
2.00	1.59	1.55	1.96	1.95	1.97	-0.73	1.30	1.29	0.91
3.00	2.07	2.01	2.87	2.19	2.20	-0.44	1.20	1.19	0.83
4.00	2.50	2.42	3.35	2.36	2.36	-0.11	1.15	1.14	0.69
5.00	2.89	2.79	3.61	2.49	2.49	0.17	1.12	1.11	0.57
6.00	3.25	3.13	3.74	2.60	2.59	0.40	1.10	1.10	0.48
7.00	3.59	3.45	3.80	2.70	2.68	0.59	1.09	1.08	0.40
8.00	3.91	3.76	3.81	2.78	2.76	0.75	1.08	1.07	0.35
9.00	4.21	4.05	3.78	2.85	2.83	0.88	1.07	1.06	0.30
10.00	4.50	4.33	3.72	2.91	2.89	1.00	1.06	1.06	0.26
15.00	5.80	5.61	3.32	3.16	3.12	1.38	1.04	1.04	0.15
20.00	6.93	6.73	2.81	3.33	3.28	1.60	1.03	1.03	0.10
25.00	7.94	7.76	2.29	3.47	3.41	1.74	1.02	1.02	0.09
30.00	8.88	8.72	1.79	3.58	3.51	1.84	1.02	1.02	0.05
35.00	9.74	9.62	1.32	3.67	3.60	1.90	1.02	1.02	0.02
40.00	10.56	10.47	0.87	3.75	3.68	1.95	1.01	1.01	0.02
45.00	11.33	11.28	0.44	3.82	3.74	1.99	1.01	1.01	0.02
50.00	12.07	12.07	0.03	3.88	3.80	2.02	1.01	1.01	0.02
60.00	13.55	12.55	-0.72	3.91	3.80	2.06	1.01	1.01	0.01

From the elliptical parameter κ, the elliptic integrals $\mathcal{F}$ & $\mathcal{E}$, the applied load Q, Poisson's ratio ν, and the equivalent modulus of elasticity E' the expressions for the major and minor axes of contact as well as the maximum deformation at the center of contact can be written, from the analysis of Hertz (1881):

$$a = \left(\frac{6\kappa^2 \mathcal{E} Q R}{\pi E'} \right)^{1/3} \tag{2.25}$$

$$b = \left(\frac{6\mathcal{E}QR}{\pi\kappa E'}\right)^{1/3} \tag{2.26}$$

$$\delta = \mathcal{F}\left[\left(\frac{9}{2\mathcal{E}R}\right)\left(\frac{Q}{\pi\kappa E'}\right)^2\right]^{1/3} \tag{2.27}$$

Were E' denotes the equivalent modulus of elasticity of the two contacting bodies, E':

$$E' = \frac{2}{\frac{1-\nu_a^2}{E_a} + \frac{1-\nu_b^2}{E_b}} \tag{2.28}$$

For an elliptic contact area and from equation 2.27 one can complete the load-deflection relationship as:

$$Q = K_p\delta^{3/2} \tag{2.29}$$

where K_p represents the ball stiffness:

$$(K_p)_{i,o} = \pi\kappa_{i,o}E'_{i,o}\sqrt{\frac{2\mathcal{E}_{i,o}R_{i,o}}{9\mathcal{F}_{i,o}^3}} \tag{2.30}$$

The total stiffness of the case with two raceways separated by a ball is then the sum of the two deformations under load:

$$\delta = \delta_i + \delta_o \tag{2.31}$$

with:

$$\delta_{i,o} = \left[\frac{Q}{(K_p)_{i,o}}\right]^{2/3} \tag{2.32}$$

Putting these equations into equation 2.29 the final expression for ball stiffness looks like the following:

$$K_p = \frac{1}{\left\{\left[\frac{1}{(K_p)_o}\right]^{2/3} + \left[\frac{1}{(K_p)_i}\right]^{2/3}\right\}^{3/2}} \tag{2.33}$$

Note that the expression for $(K_p)_{i,o}$ come from equation 2.30 with the only difference between the two being the geometry of contact and any difference in material properties.

2.3 Lincoln

Lincoln is an in-house developed software made to create computationally light but accurate rolling bearing models to be used in larger FE analysis work. The key to reducing bearing geometry and thereby also its required computational resources is to replace the rolling elements with springs. A set of springs represents the ball seen in figure 2.5.

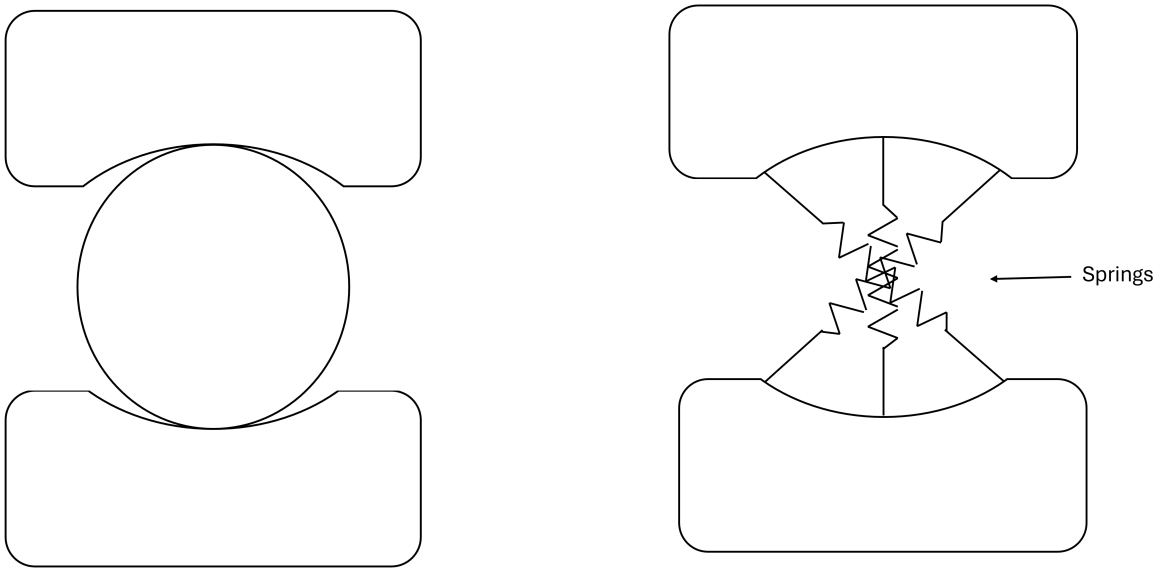

(a) Deep Groove Ball Bearing Section Cut

(b) Deep Groove Ball Bearing Section Cut with Springs

Figure 2.5: Section cuts of a deep groove ball bearing. The ball in figure 2.5(a) is replaced by springs in figure 2.5(b).

Lincoln offers a GUI for ease of use, allowing users to change the geometry of the bearing and the number of springs for each ball. See appendix C for an overview of the Lincoln GUI. Lincoln creates a node network, which serves as the foundation for determining the positions of solid and spring elements. Lincoln then prints this information to an Abaqus input file to replicate a ball bearing as an FE-model. In addition to defining nodal positions and specifying solid elements and springs, Lincoln allows users to specify surfaces for defining boundary conditions and loads. Lincoln also aims to calculate an accurate spring stiffness based on the bearing geometry. The user can use a roller or a ball bearing in a simulation with almost no coding, enabling the simulation team at Volvo GTT to improve efficiency.

2.4 Non-Linear Spring Modeling and Radial Play in Abaqus

The stiffness of the bearing is defined in Abaqus using non-linear spring elements. The springs' non-linear behavior is defined by F_i, δ_i force-displacement pairs as seen in figure 2.6 that are printed by Lincoln to the Abaqus input file. It is vital that the force-displacement range entered into Abaqus covers the entire range in which the springs will operate. The reason is because Abaqus assumes a constant force outside that range (Dassault Systemes, 2024a). See figure 2.6 for an example illustration. Exceeding the entered range of force-displacement pairs would lead to excessive displacements and an unstable model. To counteract this, the stiffness curve was defined until 200 micrometers - far exceeding typical displacements of a bearing. At the other end of the curve, springs in tension were set to develop a force detailed in equation 2.34 at a displacement of 1 mm. By doing so, the spring stiffness in tension is set very low as the ball elements can not

carry any forces in tension. Ideally, the springs in tension should be set to 0 N but that later appeared to cause modeling instability.

$$F_{tension} = \frac{100}{sp_b} \tag{2.34}$$

To model linear springs, a linear set of force-displacement pairs would have to be entered together with the force-displacement pair describing the stiffness in tension. That way, the spring behavior is linear within the range given but Abaqus interprets the nodes entered as a non-linear spring.

The play between the raceway and the ball is modeled using the non-linear definition of springs in Abaqus. As illustrated in figure 2.1, the radial play between the ball and the raceway increases with distance from the center spring. As the springs are connected directly between the raceways, it is necessary to incorporate the play into the spring modeling. To achieve this, the spring force is set to zero when the displacement equals its specific play. By doing so, the spring will not exert any force until there is initial contact between a fictional ball and the inner and outer raceways, respectively.

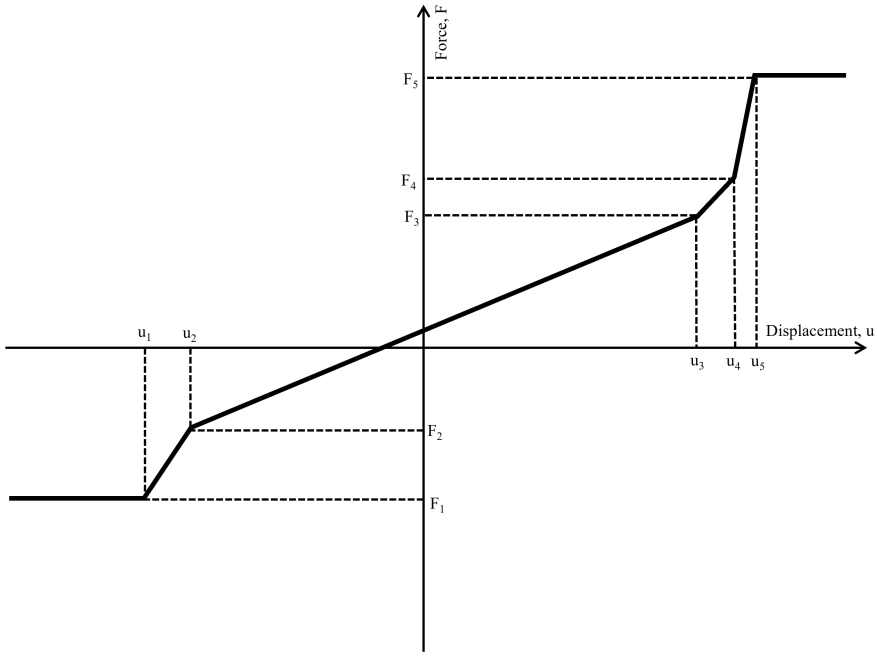

Figure 2.6: Example illustration showing how Abaqus models spring elements. Continuation of constant force is assumed if the displacement exceeds the defined force-displacement range, hence the constant forces being illustrated beyond the outermost force-displacement pairs. Please note that this curve is an example and does not necessarily align with the relationship utilized in this project.

Methodology

The methodology describes the different stages of this project from the planning phase and defining the state of Volvo's current solution, followed by a description of improvements made to this solution. The chapter continues with a detailed description of how different software were used in the different stages of the project, as well as how the results were obtained and processed. The chapter concludes with a study of the settings used in both the creation of the models and the settings used in the simulations performed, and how these settings affect the results.

3.1 Project Overview

The main deliverables and workflow was structured in a Gantt and flow chart, respectively. See figure 3.1 below for the flow chart and appendix B for the Gantt chart. An iterative approach was implemented throughout the project as the main objective was to implement a new solution using data from established and trusted software as reference.

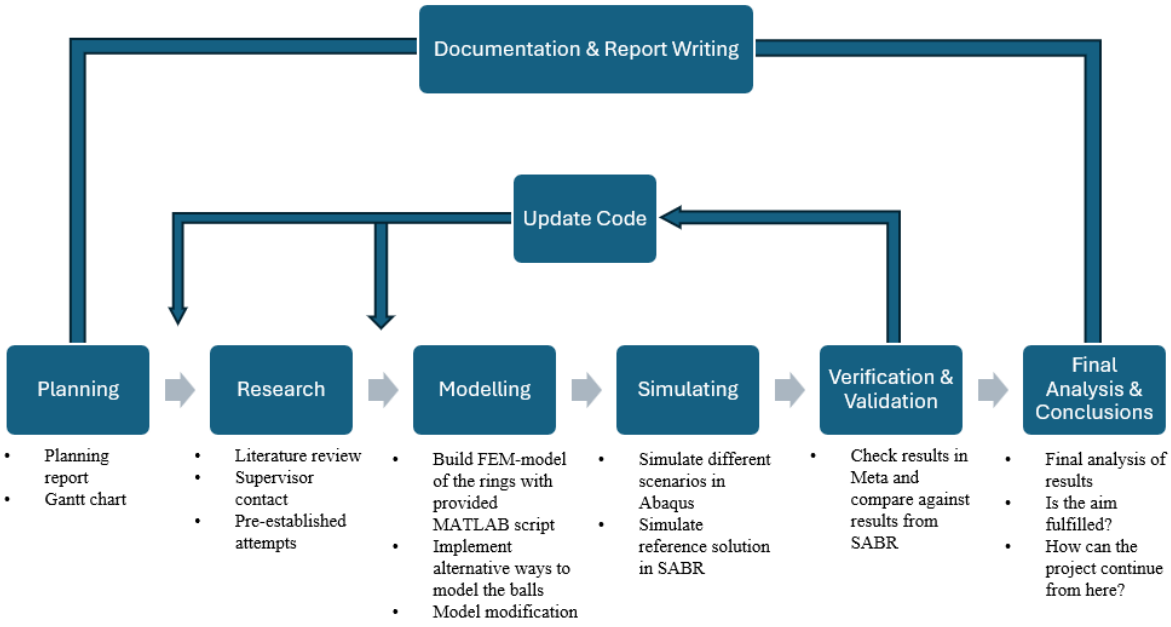

Figure 3.1: A project overview. Continuous updates of the bearings stiffness modeling and its geometry combined with a solid structure for documentation.

Lincoln is a Volvo in-house MATLAB software capable of generating finite element models (FE-models) of cylindrical and tapered roller bearings, and deep groove ball bearings. It was determined that the work should continue from this script. The strategy involved modeling the balls in the bearing with non-linear springs, aiming to reduce simulation time and mitigate the risk of simulation errors. This approach was deemed feasible because the balls themselves was not of primary concern but the transfer of forces between the outer and inner ring of the bearing. Consequently, the stiffness of the springs became a key parameter. Using springs to model force transfer was a method already in place

for cylindrical and tapered roller bearings. Those already existing solutions did therefore serve as inspiration at later stages of the project. However, as there was no general analytical expression that described ball bearing stiffness accurately available, the primary objective was to iterate and compare the solution with results from SABR. Displacements at different loads combined with various misalignments were of particular interest.

3.2 Lincoln Development

This section provides a detailed overview of Lincoln's utilization at Volvo, its application in this particular project, and script updates made to improve the program.

3.2.1 Previous Attempts to Model Ball Bearings in Abaqus

A previous attempt using a combination of linear springs and gap elements had previously been implemented in Lincoln on roller bearings by Rahani (2021). The same principles were later implemented for ball bearings. Gap elements are defined by specifying the two nodes forming the gap allowing for the nodes to be in contact (gap closed) or separated (gap open) with respect to particular directions and separation conditions. The reason why this is used is the conformity and the small radial play that exist between the ball and raceways. Connecting the linear spring directly between the two rings would cause it to exert force on the rings at the slightest change in length, effectively eliminating radial play. However, by coupling the spring to a gap element via a common node, the spring can simulate a contact constraint once the gap element closes, as illustrated in figure 3.2.

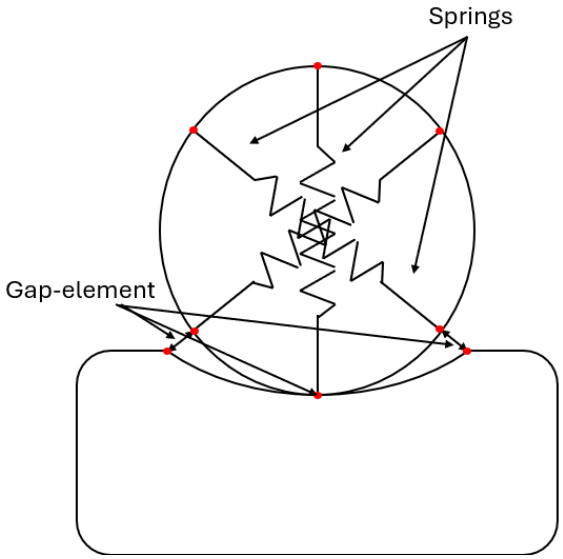

Figure 3.2: Example of a gap element solution. The void between ball and raceway is represented using gap elements coupling the springs to raceway nodes visualized as red dots.

The concept was discarded in favor of non-linear springs because the force-displacement curve can be adjusted non-linearly, allowing each spring within the ball to have its own radial play before exerting force, see section 2.4.

3.2.2 Spring setup

The implementation of the spring setup presented a challenge. Initially, the springs were directly connected to their respective raceway surfaces of the outer and inner rings, i.e. the springs and the solid elements of the rings have common nodes. This meant that a change in the position of the inner ring caused a change in the angle of the springs, see figure 3.3.

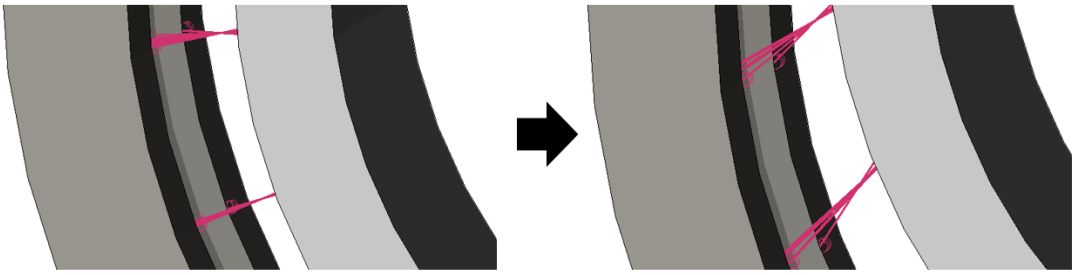

Figure 3.3: Visualization of a spring angle change. The angle changes as the inner ring is being displaced further from its nominal position in which the springs are normal to the raceway surfaces.

To address this issue, it was determined that modeling the springs' nodes intersection with the outer surface by a contact constraint between the nodes and the surface would be a more effective solution. This approach effectively addressed the issue of angular change whilst introducing the possibility of the springs/balls sliding over the surface, leading to a more desirable motion, see figure 3.4.

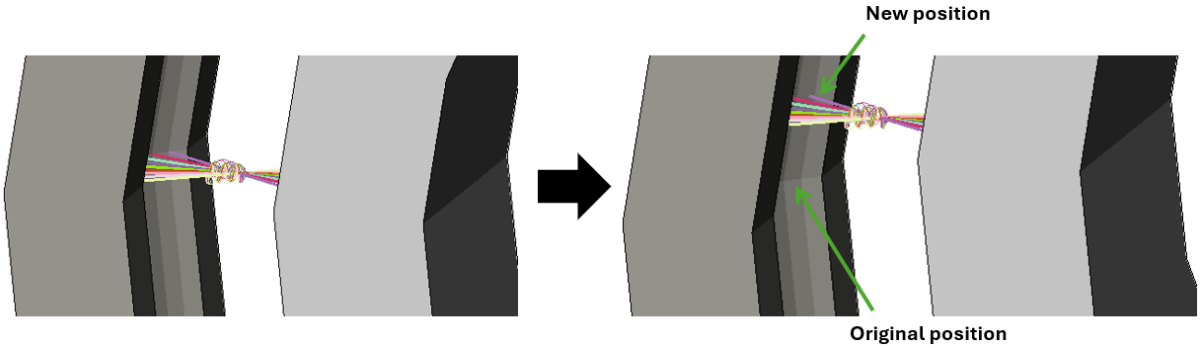

Figure 3.4: Visualization of springs sliding over the outer ring raceway.

To ensure numerical stability, the contact definition of "no separation" was employed, meaning that the springs could not leave the surfaces, see Abaqus manual (Dassault Systemes, 2024b). Although this resulted in the springs being stretched when the rings were separated, see figure 3.5, this was considered acceptable since the non-linear spring definition set the stiffness to a value close to zero in elongated springs.

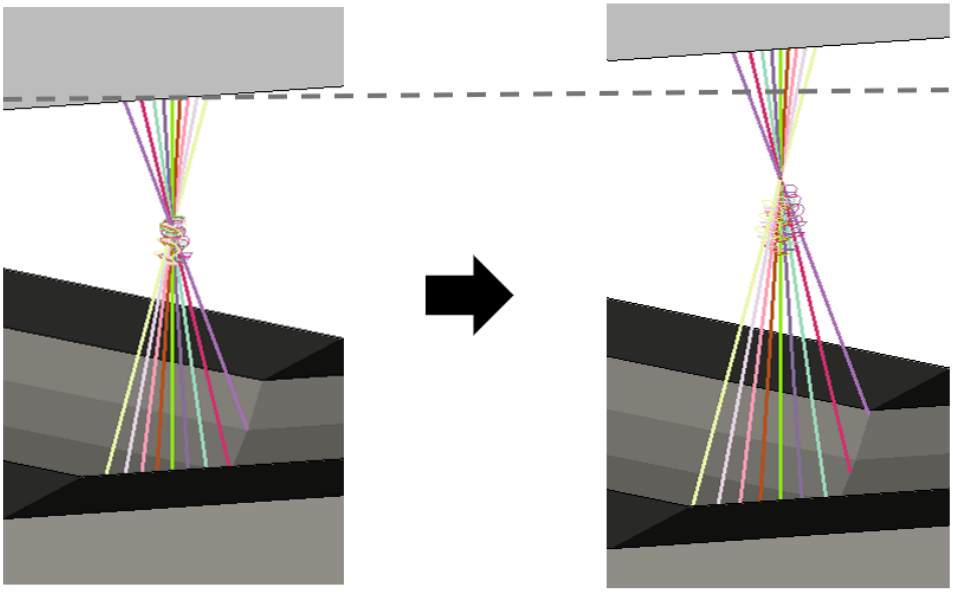

Figure 3.5: Elongation of Springs Positioned at the Opposite Direction of Motion. Impact on bearing stiffness is negligible.

Before concluding that the contact approach had been completed, it was necessary to address an issue where the springs could glide against the raceways freely. Due to the design of the springs as being highly stiff in compression and ideally not stiff at all in tension, the motion of the spring pair under loading was sometimes such that they would glide around over the raceways, maintaining their original length. This led to highly unstable and unreasonable results. To solve this issue, a number of MPCs (Multi-Point Constraints) called sliders and links were set in place, see figures 3.6 & 3.7 (Dassault Systemes, 2024c). A slider (yellow) MPC forces three nodes to align along a straight line. A link MPC forces two nodes to maintain their distance to each other. The first slider connects the two nodes of the spring (blue) to a node on the inner diameter of the inner ring. That node is kept in position by a slider and a link (white). The slider keeps it at the inner diameter by connecting it to the corner nodes of the ring. The link keeps it in the correct axial position by connecting it to one of the corner nodes.

The sliders, aligned with the springs (blue), constrain the springs to align with the slider's orientation. To ensure the slider's orientation is maintained, the node at the base is secured by a combination of a slider and a beam/link (white).

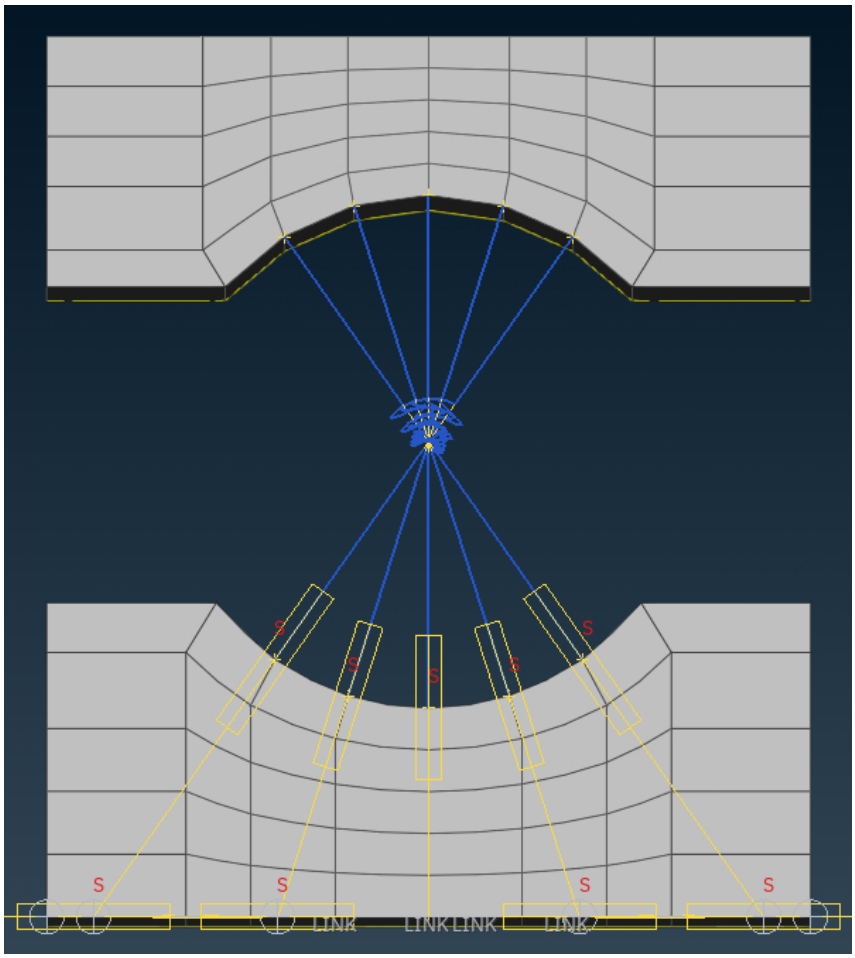

Figure 3.6: Setup to keep springs aligned. Sliders in yellow and springs in blue. The springs are constrained tangent to the sliders orienting them perpendicular to the inner raceway surface.

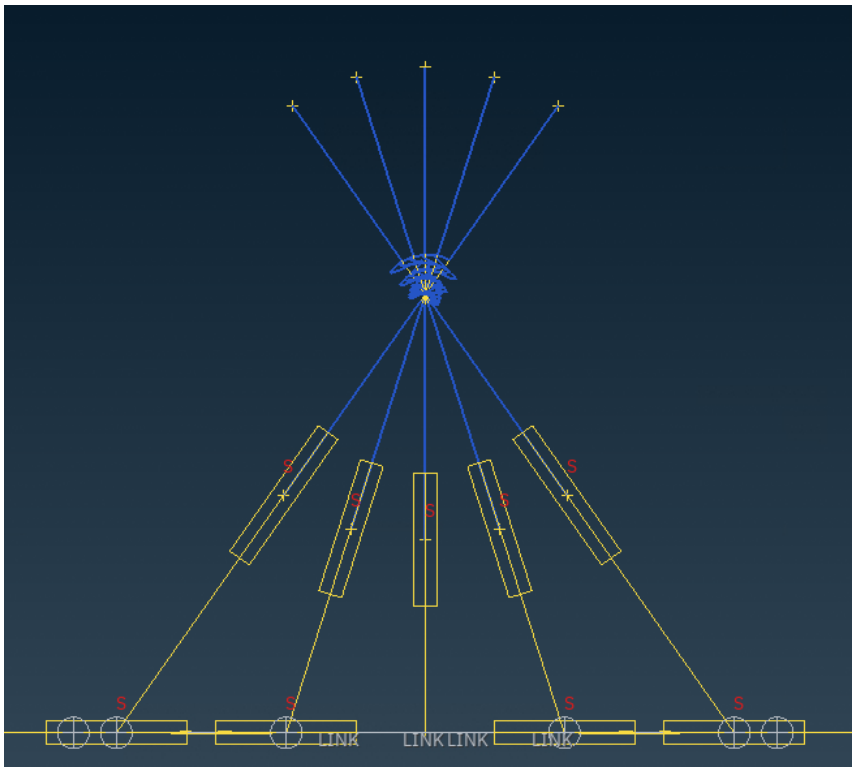

Figure 3.7: Setup to keep springs aligned without solids

3.3 Bearing Geometry Verification

This chapter describes how the springs' and sliders' bearing geometry generated using Lincoln was verified against SABR with CAD (CATIA V5). This was done by exporting the coordinates of the raceway nodes from Lincoln and importing them as a point cloud into CAD. The points were then used to derive two splines, one each for the outer and inner raceway. See figure 3.8.

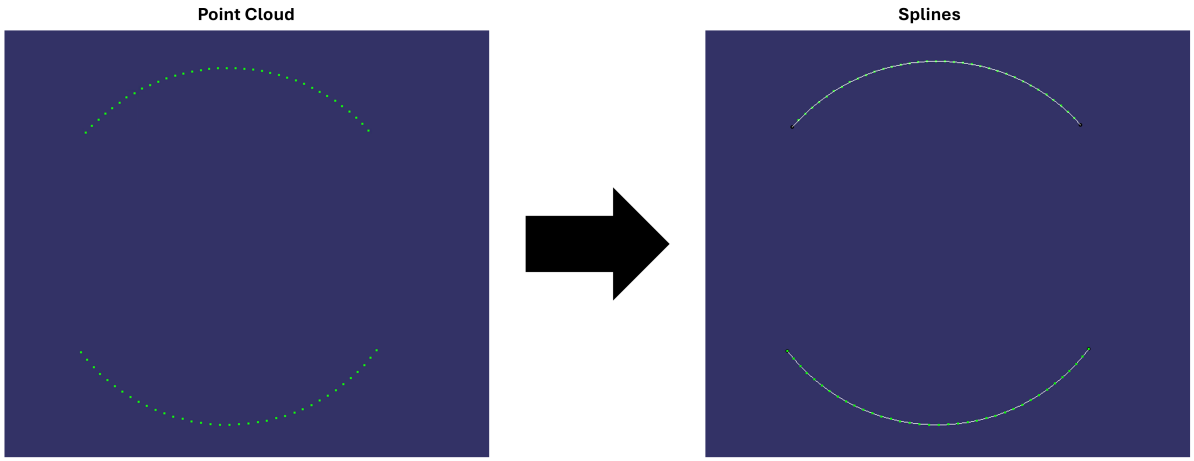

Figure 3.8: Splines fitted to a point cloud of coordinates exported from Lincoln.

By measuring the radii of the splines, it was confirmed that the raceway radius can

be calculated by multiplying the ball radius with the curvature gain. Furthermore, an inserted ball verified the radial clearance between the two splines at the center spring, see figure 3.9.

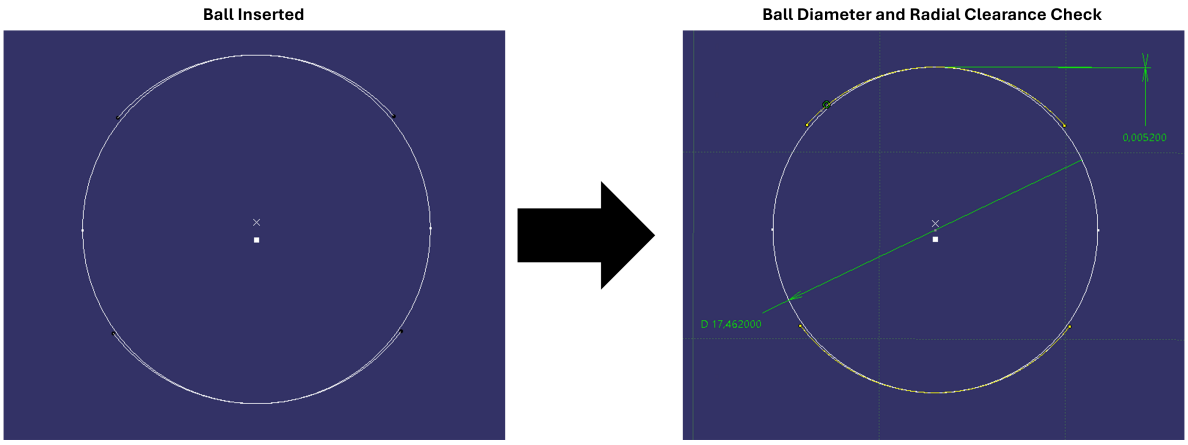

Figure 3.9: Ball inserted between the splines with contact condition to the inner raceway to verify radial clearance. SKF bearing 6216 shown in this figure, with a ball diameter of 17.462 *mm* and a radial clearance of 0.00052 **mm**.

Radial play was verified by placing lines representing springs between the two splines at identical angles to which the springs are oriented in, as seen in figure 3.10.

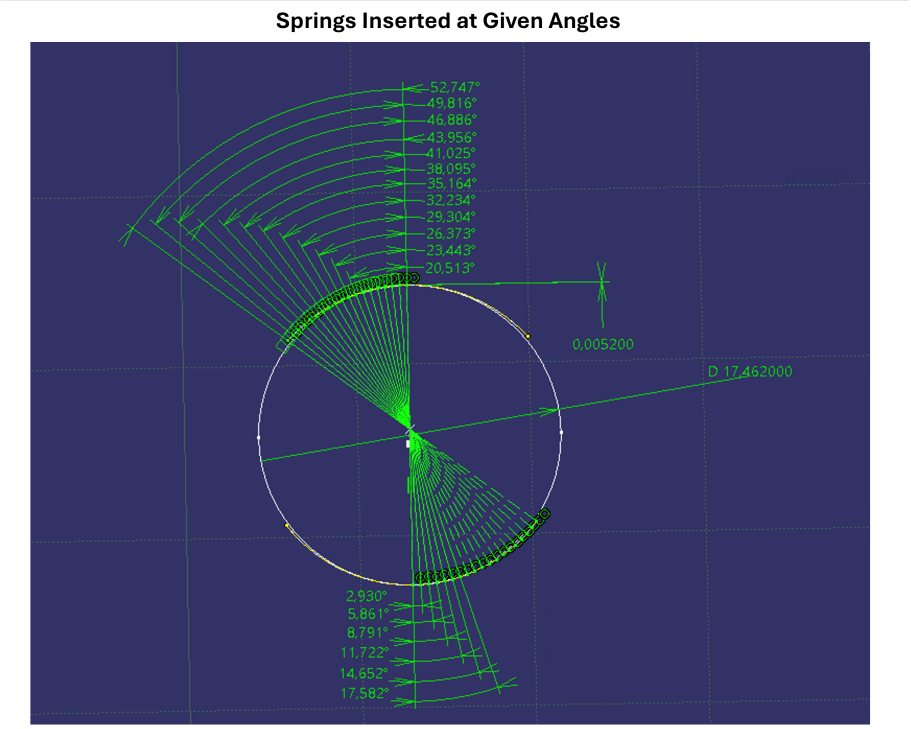

Figure 3.10: Lines, representing springs, placed at angles identical to the Lincoln orientation.

The lines were constrained perpendicular to the inner raceway, consistent with the con-

figuration in the Lincoln model. The radial play was derived by measuring the length of each line using the measurement tool in CAD, as seen in figure 3.11, and subtracting the ball diameter. The radial play values were then compared with the radial play calculated in Lincoln. The measured results verified that the Lincoln geometry aligned with the expected given radial play.

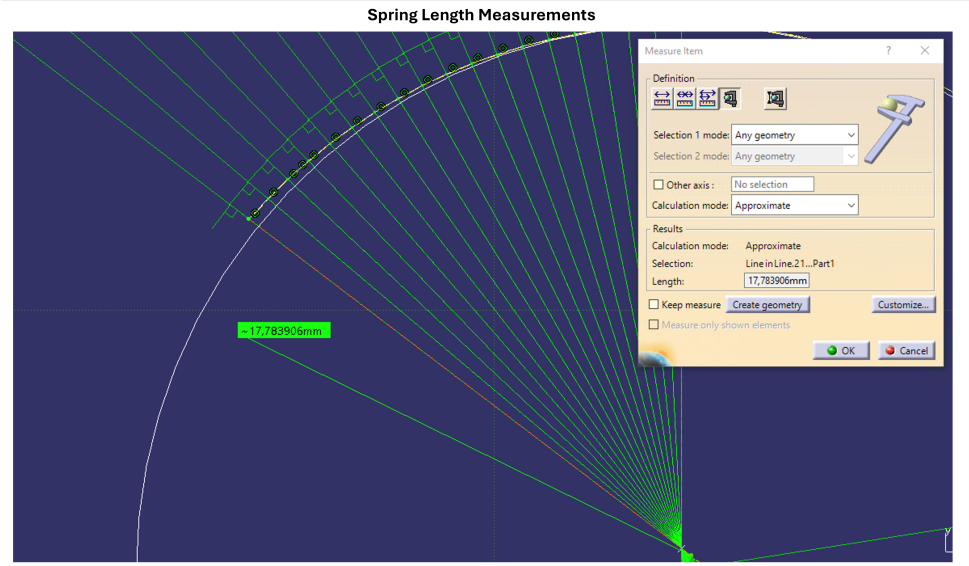

Figure 3.11: A spring being measured using CATIA measurement tool. The given value subtracted by the ball diameter equals the radial clearance.

Another performed test investigated the raceway geometries specifically by comparing CAD measurements with reference results from SABR. The following paragraph details how these measurements were taken using both CAD and SABR, respectively.

The CAD measurements were made using the same point cloud previously mentioned. Contrary to the previous radial play verification, a ball was inserted at 0, 5, 10, 15, and 20 degrees from center with a contact condition to the inner raceway. An arc representing the outer raceway was then inserted tangent to the other side of the inserted ball. By measuring the distance between the center point of the arc and the original center point of the outer ring, its total displacement could be derived. See figure 3.12 for an overview of the method implemented. The results are listed and illustrated in section 4.1, in table 4.1 and figure 4.1, respectively.

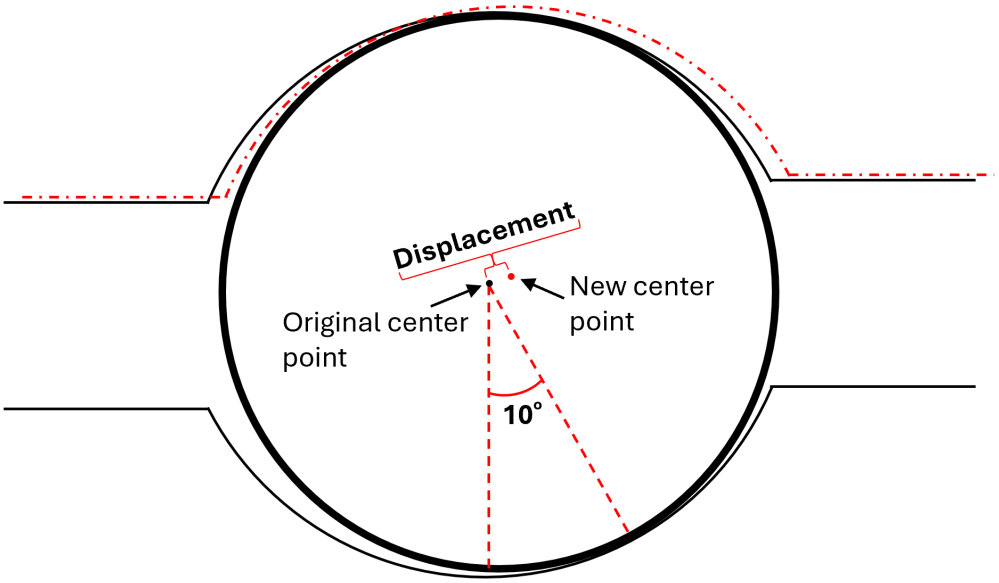

Figure 3.12: Method implemented to measure the raceway geometries using CAD. In this instance, a ball was inserted at an angle of 10° constrained perpendicular to the inner raceway. An arc (dashed red) was then inserted opposite of the balls contact with the inner rim tangent to the ball representing a displaced outer raceway. A measurement was then taken between the center points of the original outer raceway (solid black) and the displaced outer raceway (dashed red).

A different methodology was used to obtain raceway geometry measurements in SABR. First, a small radial load of 50 N was applied. Then, the following axial loads were added: 0, 2, 4, 6, 8, and 10 N. For axial load, the resulting radial and axial displacements were noted alongside the ball compression. In order to derive the curvature of the raceway, the ball compression was subtracted from the radial displacements. The results are listed and illustrated under section 4.1 in table 4.2 and figure 4.2.

The final test compared the geometrical behavior of the Lincoln geometry using an Abaqus simulation. The process of obtaining the Abaqus geometry measurements was very similar to the method used with SABR, in the sense that a 50 N radial load was applied at the bearing inner ring. However, rather than applying an axial load as in SABR, axial displacements were prescribed into the simulation. MetaPost was then used to measure the displacements. This was done by measuring the inner ring radial displacement subtracted by the largest spring compression. The spring compression was measured by obtaining the node positions and subtracting the nominal spring length. The results indicated that the displacement did not reach the amplitude that had been previously measured using SABR and CAD, please refer to section 4.1.

As a result, another type of bearing geometry was tested. Replacing the original spring configuration with springs with a length equal to the ball diameter. All springs were assigned the same length and inserted perpendicular to the inner ring, see figure 3.13. The play between ball and raceway now was represented by a physical gap between the two elements. The springs were given a very high stiffness practically making them static elements. Again the same test with a small radial load and a prescribed axial displacement was run. Unfortunately, using this geometry yielded the same results as the

previous attempt, please refer to section 4.1.

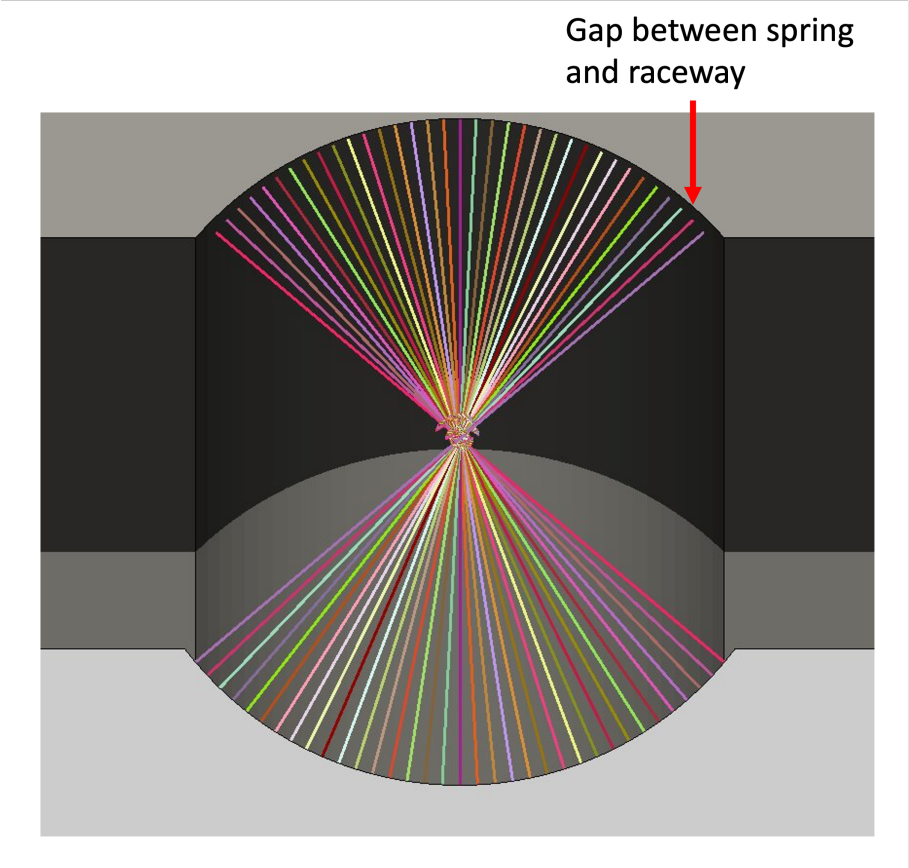

Figure 3.13: Alternative bearing geometry for bearing geometry verification in Abaqus.

3.4 Pre-Processing in ANSA

Once the geometry and spring definitions have been completed through Lincoln, as illustrated in figure 3.14(a), the subsequent step involves preparing the model for simulation by applying boundary conditions (BCs), loads, requesting the desired output, defining a step end time, time-step size, and whether the simulation is static or if large deformations are permitted, see example .inp file in appendix G. This can be done in the commercial pre-processing software ANSA. However, most simulations in this project utilized the same settings, with the only difference being the load magnitude or misalignment of the inner ring position. This meant that the same input file could be used with minor alterations. The BCs and loads were applied on the surfaces defined in Lincoln, see figure 3.14(b). The surface on the outer ring was completely constrained, whilst the surface on the inner ring was the one on which the load is applied. The inner ring was constrained in all rotations, see figure 3.14(b).

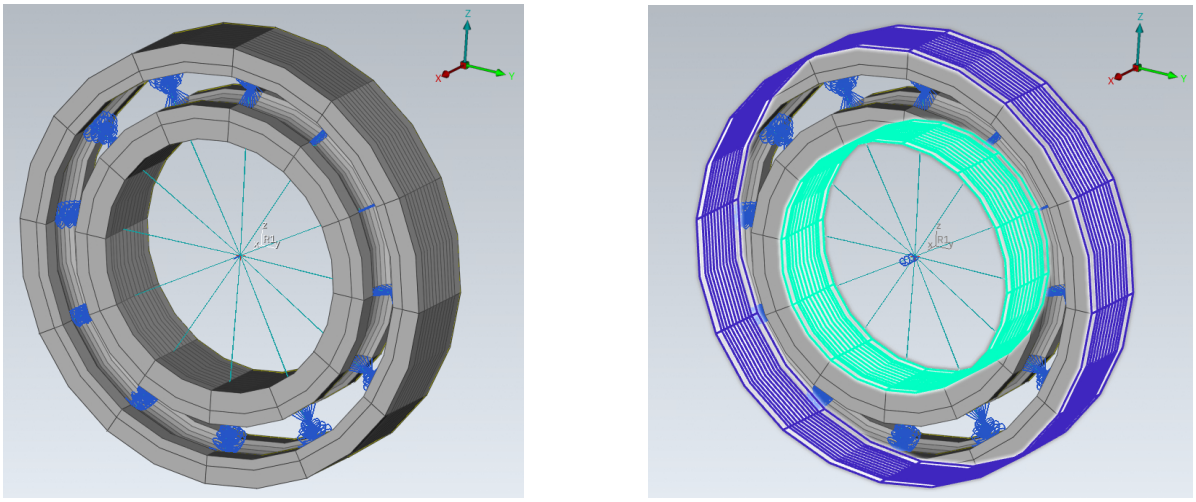

(a) Ball Bearing Model in ANSA

(b) Bearing Model with Surfaces Highlighted

Figure 3.14: Generic Deep Groove Ball Bearing Model Illustrated using ANSA

To simulate the scenario in which the inner and outer rings are slightly misaligned during loading, a prescribed rotation of the inner ring around either the y or z axis will result in the desired orthogonal and parallel misalignment's outlined in table 3.1. The rotation of the inner ring makes the ball creep up on the raceway and initiates contact with the springs, see figure 3.15. By allowing the inner ring to move axially, an applied small radial load will displace the inner ring until equilibrium is restored prior to applying any additional loads, see figure 3.16.

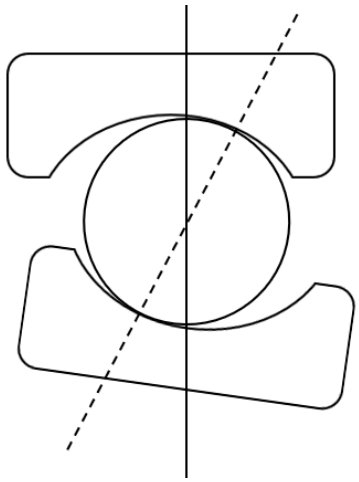

Figure 3.15: Raceway creep due to misalignment. The original line of contact is represented by a straight line and the new line of contact is represented by a dashed line.

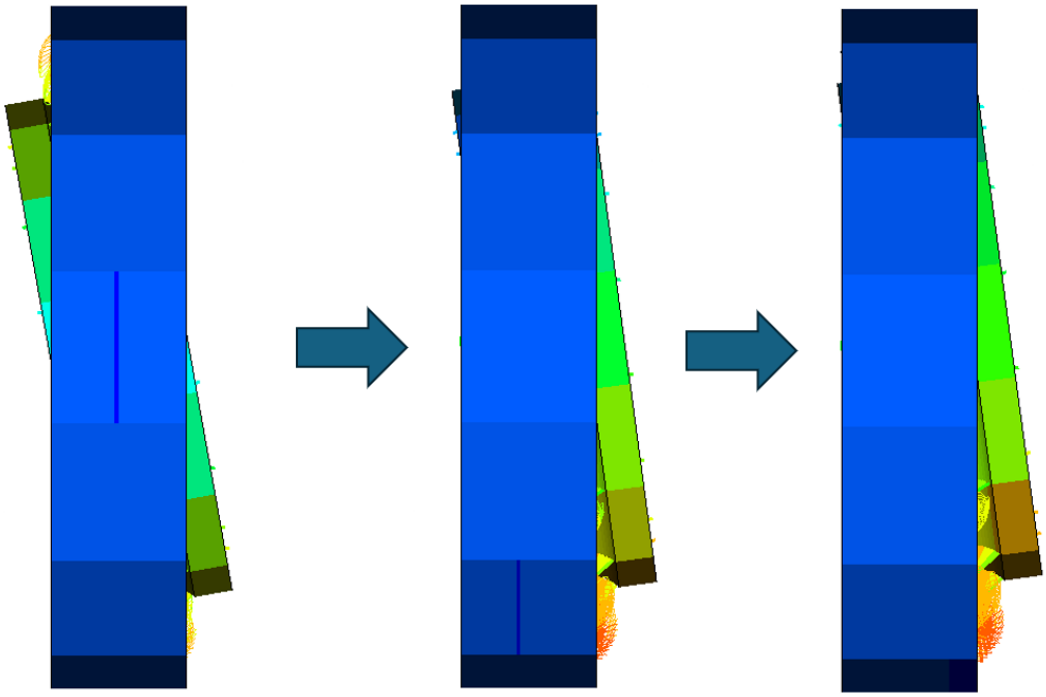

Figure 3.16: Misalignment equilibrium. Scaled deformation for illustrative purposes. Left: Initial rotation. Middle: Axial displacement of the ring until equilibrium is obtained. Right: Radial load is applied.

3.5 SABR Bearing Simulations

SABR is a commercial software used to simulate gearboxes and their respective parts. Realis, the company behind SABR, claims to use the same bearing calculations as the bearing design and manufacturing companies use, including the ISO 16281 and ISO 281 standards (Realis Simulation, 2025). The bearing displacements at different loads and misalignments were modeled and the results were used as reference. See figure 3.17 for the SABR model used in this study.

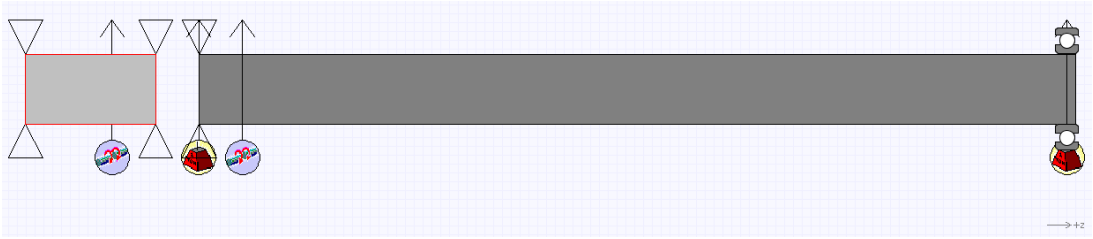

Figure 3.17: Example of a SABR model showing two connected axles supported by one deep groove ball bearing (to the right) alongside three ideal bearings.

Figure 3.17 shows how two axles are connected using a direct coupling, this is required because SABR needs to think it is simulating a gearbox. The bearing of interest was placed furthest to the right where either a radial, axial or combined load is applied. At the other end of the shaft, a radial load was applied to cause a radial displacement that

induced shaft misalignments per table 3.1. The stiffness and length of the axle was set so that an applied load of 1000 N would result in roughly 1 mrad of misalignment. Two to four iterations were required to set the radial load needed to induce a misalignment in accordance to the table.

Table 3.1: Types of misalignment combined with different load cases. First implemented by Rahani (2021).

Misalignment Case	**1**	**2**	**3**	**4**	**5**	**6**	**7**	**8**	**9**	
Parallel	0	0	0	1	1	1	3	3	3	[mrad]
Orthogonal	0	1	3	0	1	3	0	1	3	[mrad]

3.6 Post-Processing in MetaPost

Abaqus is the software used to conduct the finite element method (FEM) simulations in this project. However, it should be noted that it is not utilized for post-processing. To view the results, the program used was MetaPost, also known as META. META is an excellent tool for visualization purposes, as it streamlines and expedites the iterative process of comparing different configurations whilst requiring minimal previous experience. In this project, the primary use of META was to visualize the geometry's general motion, i.e. the deformed shape under load, in various simulations and to observe how the springs respond to different conditions. For instance, if the outermost spring ends up outside the raceway in the event of misalignment or an axial load being applied, see figure 3.18.

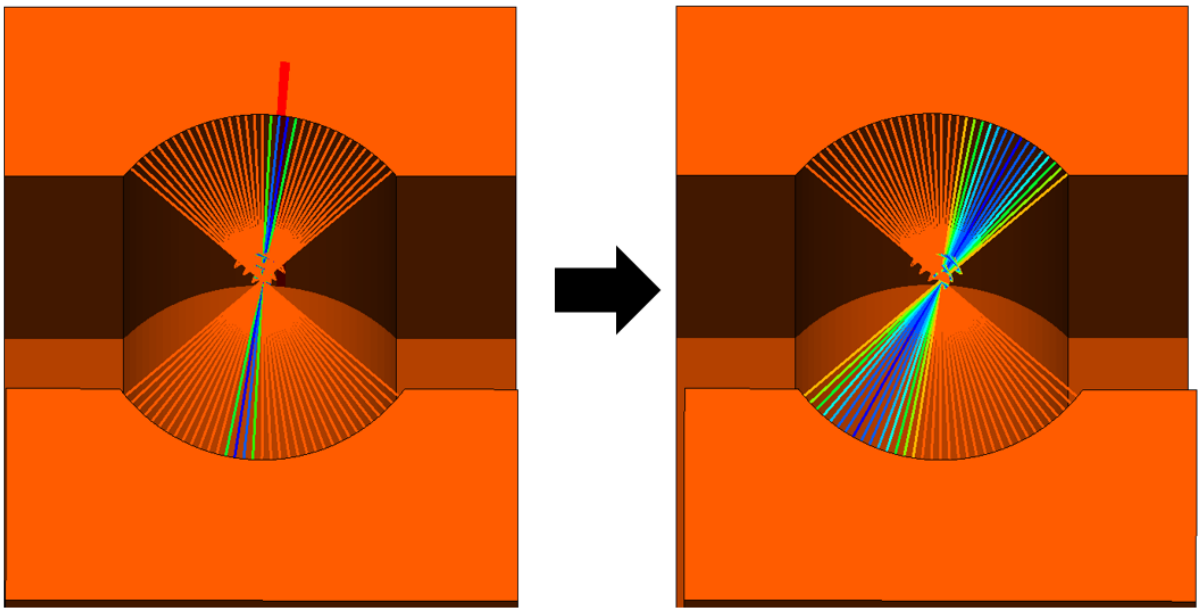

Figure 3.18: Visualization of a spring set almost leaving the raceway in a simulation with misalignment and an applied axial load.

Another feature is the option to measure the stress of each spring at different times during

the simulation. This allows for precise determination of the load level at which a spring becomes active, see figure 3.19.

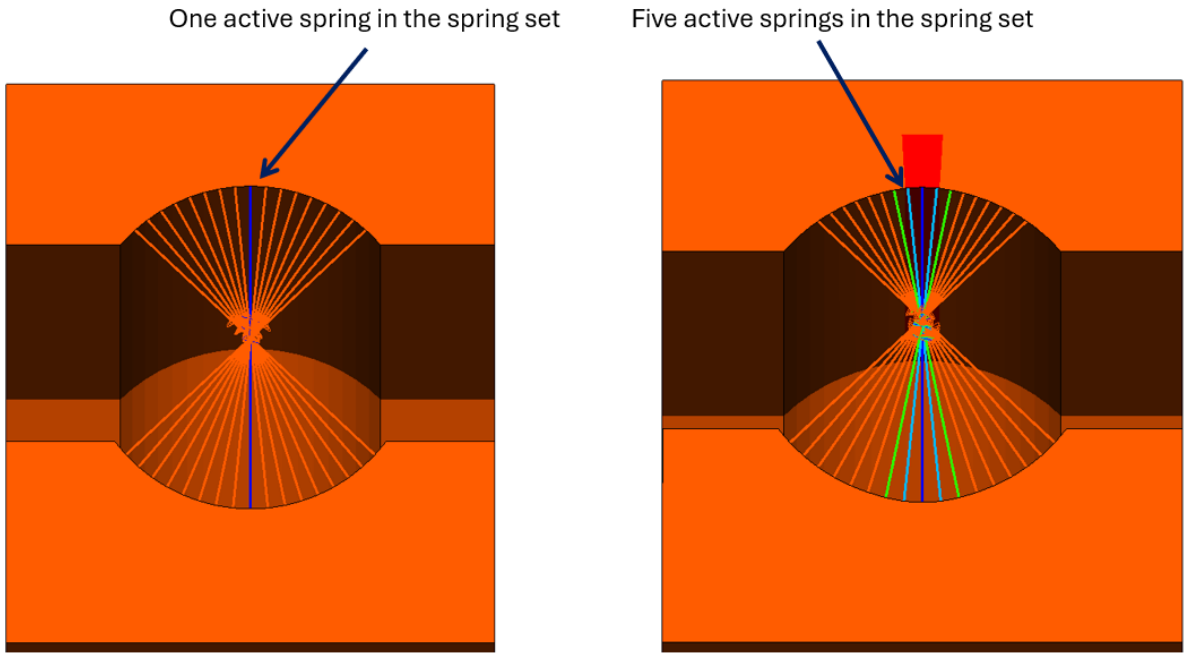

Figure 3.19: Visualization of the springs under stress i.e., engaged springs, at two different load levels in META

This is useful for verifying the proper implementation of the spring's play and for measuring the largest length change in the spring under maximum stress. It also allows for determining the number of springs that are in contact and thereby considered active. This can be used to calculate the angle of contact in the raceways by measuring the angle between the two outermost active springs, this angle is called the contact angle throughout this project, see figure 3.20.

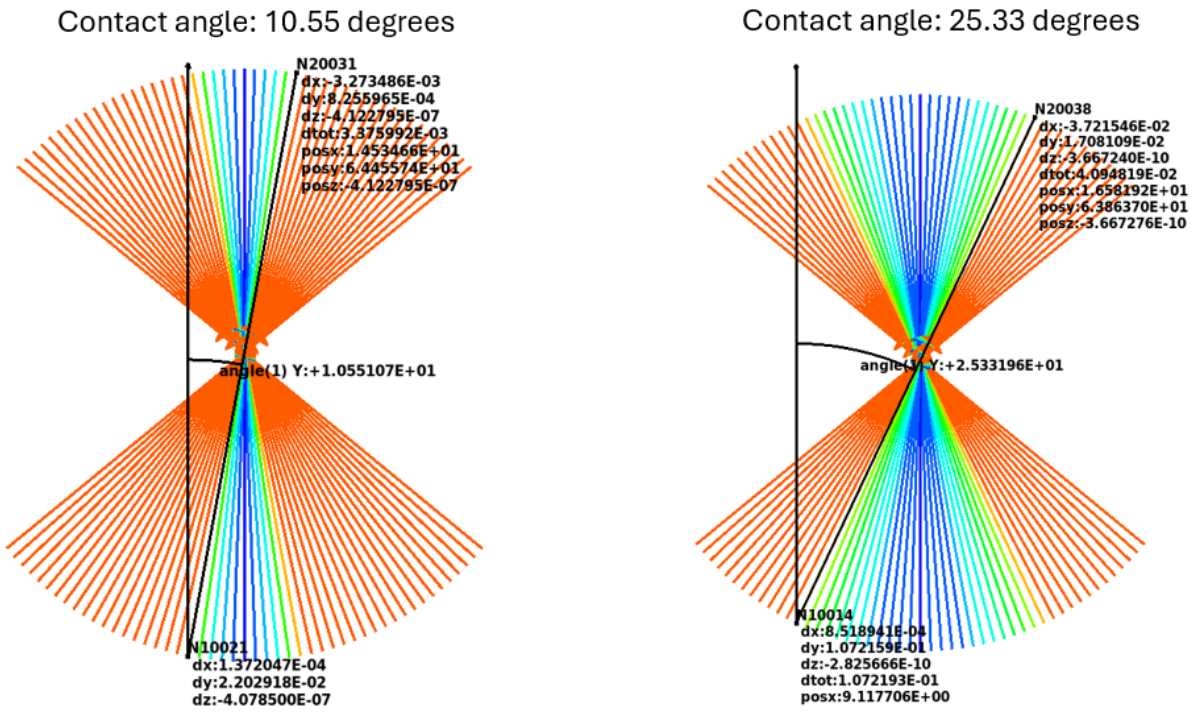

Figure 3.20: Visualization of how the contact angle can be measured in META for two different load levels.

3.7 Post-Processing in Excel

Excel was used to compare results against reference data from SABR. The displacement of the center point of the inner ring was extracted in the x, y, and z directions. The results were imported into Excel and plotted alongside values from SABR to ascertain if the general motion matched, see figure 3.21.

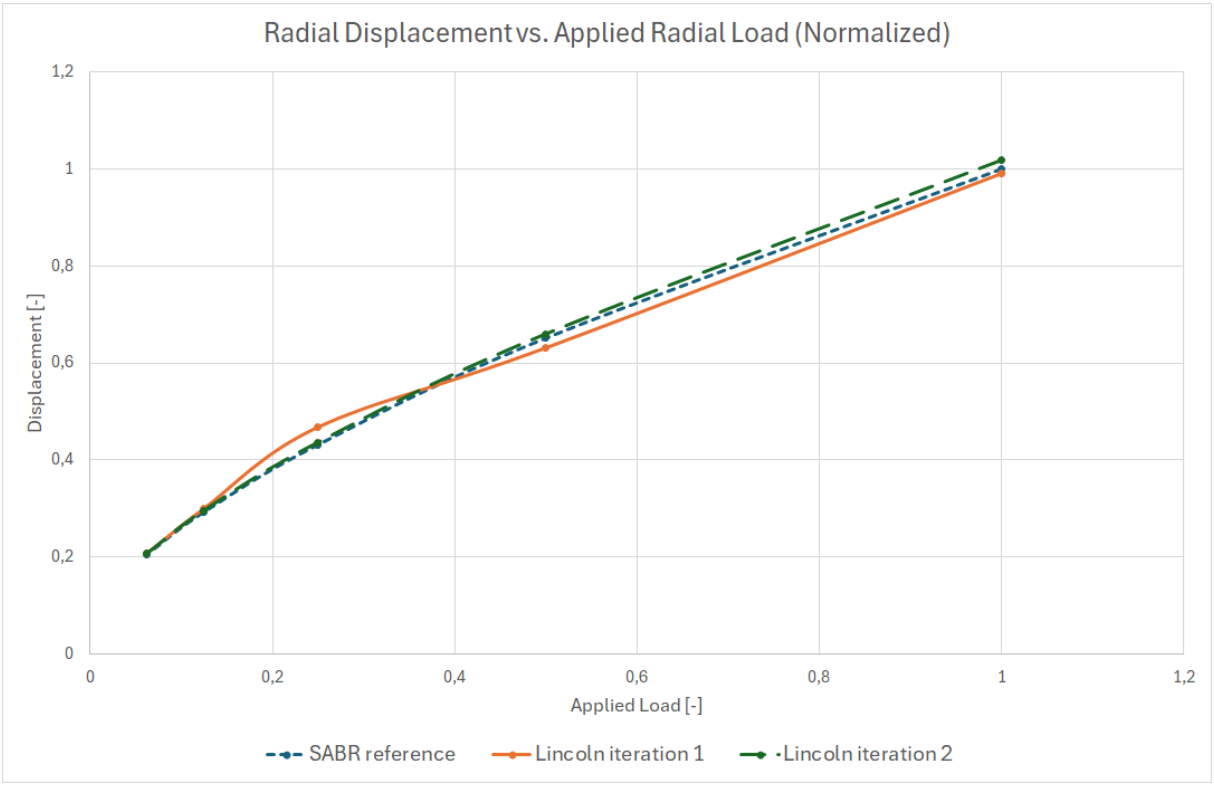

Figure 3.21: Normalized plot of the inner rings displacement in y-direction vs. the applied load for two different Lincoln models

The percentage difference between the results and the reference was calculated as well. Any result with a percentage difference within ±10% was considered satisfactory and marked green. Values between $10 - 20\%$ were deemed acceptable but not optimal and, as a result, were marked yellow. Finally, any discrepancy larger than ±20% was marked red, indicating the need for the model to be reworked, see figure 3.22.

6216 lincoln config:

Load case 1		alignment l											jonathan curvefit min_max		jonathan curvefit nonlin	
	72800	Fx	Fy	results	dx sabr	dx abaqus 4 Point stiffness	difference [%]	dx abaqus (x^5/6)	difference [%]	dx abaqus (x^3/2)	difference [%]		dx abaqus min_max	diff [%]	dx abaqus nonlin	diff [%]
1/2	36400	108			108,43	107,46	-0,90%	120,41	11,04%	127,85269	17,91%		109,99874	1,45%	110,27705	1,70%
1/4	18200	71			70,64	68,47	-3,08%	73,24	3,68%	85,366659	20,85%		70,531473	-0,15%	71,488269	1,20%
1/8	9100	47			46,82	50,72	8,33%	45,98	-1,79%	57,846209	23,55%		46,203089	-1,32%	47,283754	0,99%
1/16	4550	32			31,80	32,50	2,20%	29,95	-5,81%	39,930907	25,57%		31,100505	-2,20%	32,093801	0,92%
1/32	2275	22			22,33	22,48	0,66%	20,49	-8,24%	28,154238	26,08%		21,69677	-2,84%	22,492075	0,73%
	100															
Load case 2	1 mrad orthogonal	alignment l										effective clearance results	jonathan curvefit min_max		jonathan curvefit nonlin	
	72800	Fx	Fy	results	dx sabr	dx abaqus (x^2/3)	difference [%]	dx abaqus (x^5/6)	difference [%]	dx abaqus (x^3/2)	difference [%]		dx abaqus min_max	diff [%]	dx abaqus nonlin	diff [%]
1/2	36400	1118			108,37	115,62551	7%	108,12552	-0,23%	108,24316	-0,12%		109,9006	1,41%	110,16834	1,66%
1/4	18200	1076			70,57	78,772309	12%	71,27231	1,00%	69,00344	-2,22%		70,343946	-0,32%	71,310898	1,05%
1/8	9100	1049			46,75	56,234022	20%	48,734023	4,24%	44,745328	-4,29%		45,854921	-1,91%	46,994346	0,52%
1/16	4550	1033			31,74	41,702283	31%	34,202284	7,76%	29,719759	-6,36%		30,722119	-3,21%	31,710788	-0,09%
1/32	2275	1023			22,27	33,258585	49%	25,758586	15,66%	19,664675	-11,70%		21,320726	-4,26%	22,103633	-0,75%
Load case 3	3 mrad orthogonal	alignment l										effective clearance results	jonathan curvefit min_max		jonathan curvefit nonlin	
	72800	Fx	Fy	results	dx sabr	dx abaqus (x^2/3)	difference [%]	dx abaqus (x^5/6)	difference [%]	dx abaqus (x^3/2)	difference [%]		dx abaqus min_max	diff [%]	dx abaqus nonlin	diff [%]
1/2	36400	3142			107,83	129,26113	20%	106,76117	-0,99%	106,94274	-0,82%		109,19782	1,27%	109,46492	1,52%
1/4	18200	3090			69,99	91,940198	31%	69,440232	-0,79%	67,482232	-3,58%		69,395961	-0,85%	70,380765	0,56%
1/8	9100	3063			46,38	70,057358	51%	47,557393	2,54%	44,676944	-3,67%		45,330906	-2,26%	46,313055	-0,14%
1/16	4550	3073			32,8	56,978939	74%	34,478973	5,12%	29,676256	-9,52%		31,680075	-3,41%	32,584761	-0,66%
1/32	2275	3068			23,3	45,540772	95%	23,040806	-1,11%	17,631782	-24,33%		21,699875	-6,87%	22,509672	-3,39%
Load case 4	1 mrad parallel	alignment l										effective clearance results	jonathan curvefit min_max		jonathan curvefit nonlin	
	72800	Fx	Fy	results	dx sabr	dx abaqus (x^2/3)	difference [%]	dx abaqus (x^5/6)	difference [%]	dx abaqus (x^3/2)	difference [%]		dx abaqus min_max	diff [%]	dx abaqus nonlin	diff [%]
1/2	36400	108	1075		107,88	107,01923	-1%	107,18906	-0,64%	107,41412	-0,43%		108,99105	1,03%	109,27678	1,29%
1/4	18200	70	1038		70,07	69,966326	0%	70,088445	0,03%	68,027658	-2,91%		69,300684	-1,10%	70,316813	0,35%
1/8	9100	46	1019		46,24	47,137091	2%	47,178178	2,03%	43,868755	-5,13%		45,093275	-2,48%	46,148403	-0,20%
1/16	4550	31	1010		31,23	32,398828	4%	33,091613	5,96%	28,722917	-8,03%		29,916086	-4,21%	30,929284	-0,96%
1/32	2275	22	1005		21,76	23,832808	10%	24,403674	12,15%	19,032577	-12,53%		20,520942	-5,69%	21,318357	-2,03%

Figure 3.22: Error sheet of bearing 6216 for different methods of calculating the stiffness

For visualization purposes the error results were also plotted, see figure 3.23 for an example of two different iterations of Lincoln and their respective relative difference against values from SABR.

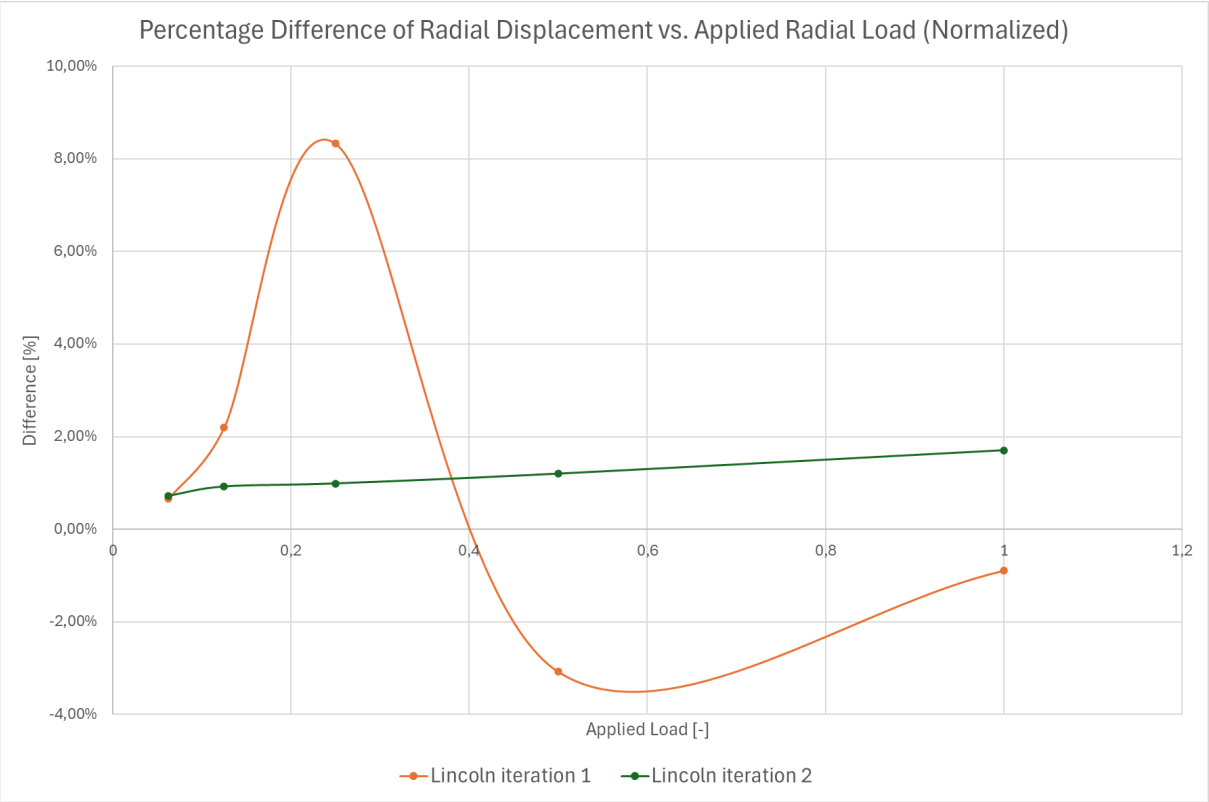

Figure 3.23: Plot of the percentage displacement difference of two different Lincoln models against SABR reference.

The figure suggests several conclusions. First, both lines are within the 10% error margin. Second, the smallest error of the orange line is at the two ends of the graph, whilst the green line increases almost linearly from smallest to largest error. The orange line's fluctuations between positive and negative values indicate that, under certain load conditions, displacements are too large, signifying insufficient stiffness. Conversely, under other loads, the situation is reversed. For the green line, however, the error is constantly positive. This suggests that even better results might be possible by simply scaling the force-displacement curve of the springs corresponding to the green line.

3.8 Analytical Load-Deflection Stiffness

Two attempts were made to use an analytical load deflection relationship in this project, based on the theory presented in sections 2.2.1 and 2.2.2. The subsequent section details the implementation of these relationships in Lincoln, along with preliminary results and conclusions.

3.8.1 Harris Load-Deflection relationship

The theory outlined in section 2.2.1 was implemented utilizing a MATLAB script to enter bearing data and plot the results. The script required the following bearing geometry parameters: ball diameter, inner and outer groove radius, and pitch diameter. For bearing geometry data of SKF 6216, 6008, and 6204, please refer to appendix E. The script can

be found in appendix D. An initial comparison of results between SKF bearing 6216 and 6008 concluded that the relative error is similar, as illustrated in figure 3.24.

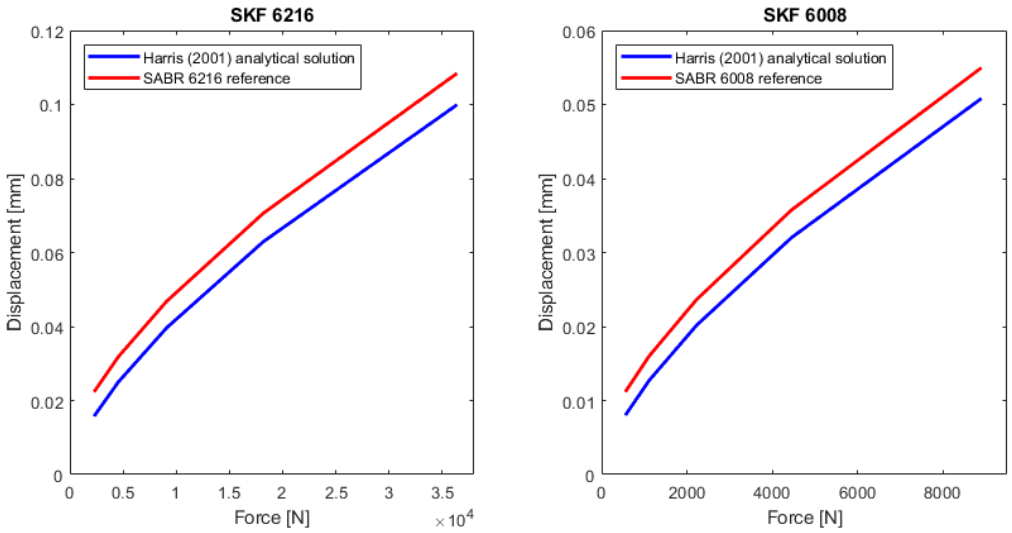

Figure 3.24: Results of Harris theory. SKF bearings 6216 and 6008 (red) compared to their respective SABR reference (blue).

Moving on, the theoretical results of SKF 6204 did not align with the results of 6216 and 6008 as the relative error deviates from what was previously seen in figure 3.24, see figure 3.25.

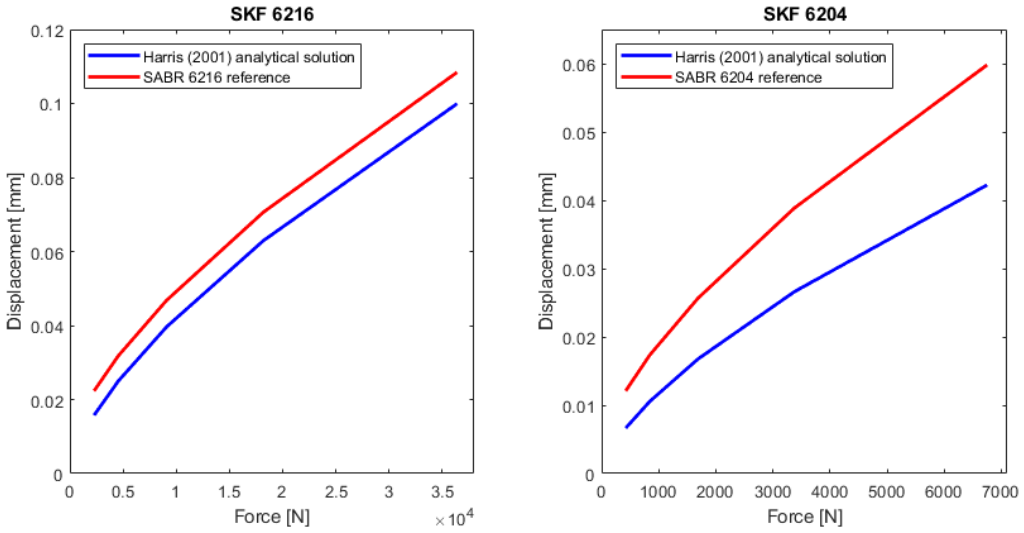

Figure 3.25: Results of Harris theory. SKF Bearing 6216 (left) and 6204 (right) compared in red to their respective SABR reference in blue.

Although the initial theoretical results showed unfavorable results, the derived stiffness was implemented in Lincoln and modeled in Abaqus. As expected, SKF bearing 6216 showed results deviating from reference values with displacements being too low, see figure 3.26. All misalignments listed in table 3.1 were also modeled, their relative error is shown in figure 3.27.

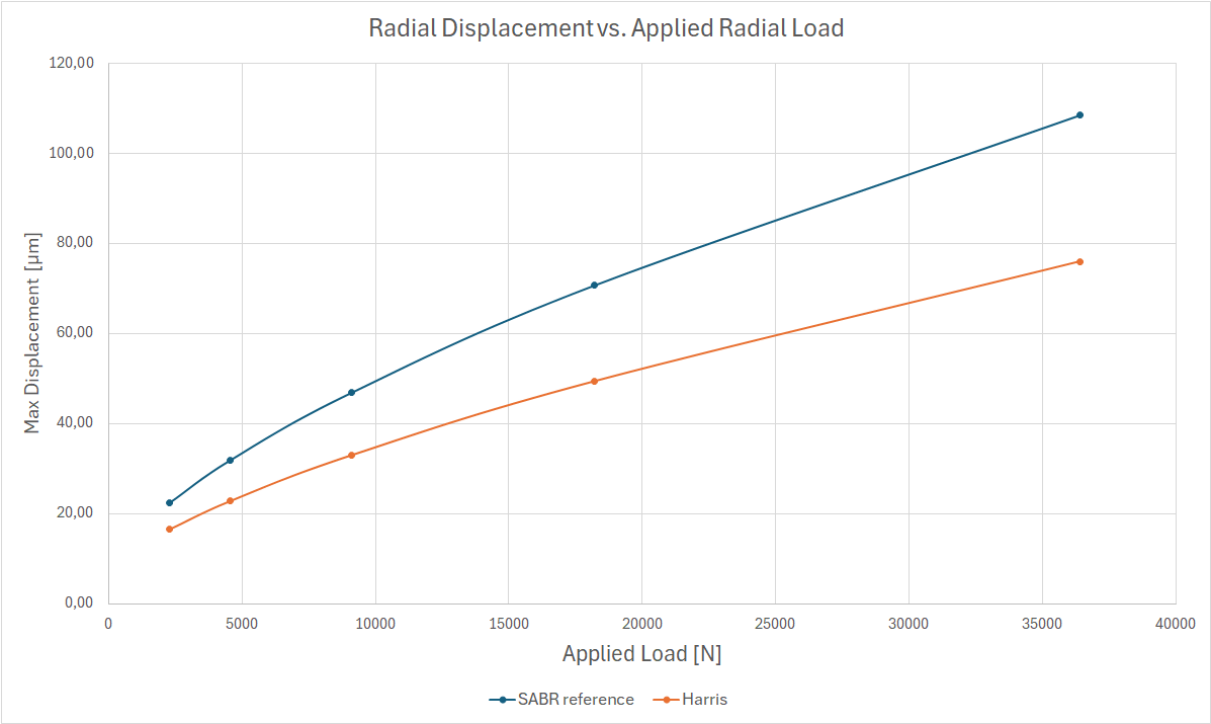

Figure 3.26: Displacement vs. Load of SKF bearing 6216, results from Abaqus.

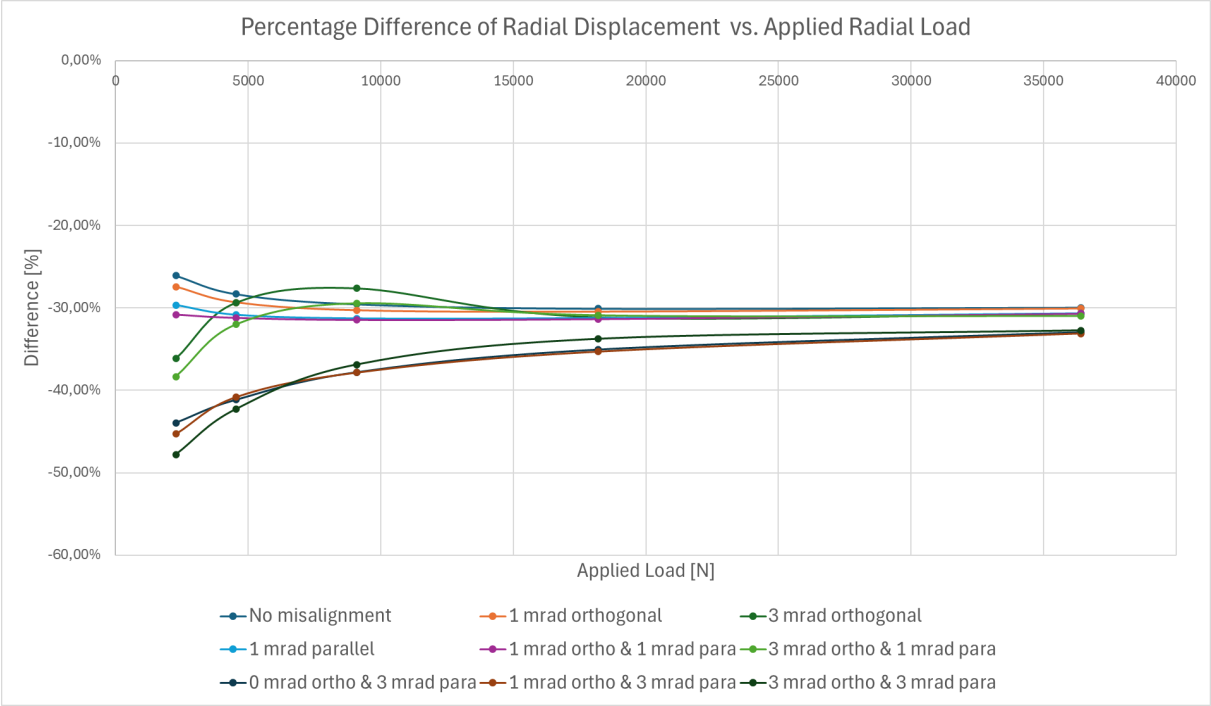

Figure 3.27: Error vs. Load of all different misalignment load cases, results from Abaqus.

It was determined that the implementation of Harris' theory is unable to account for varying bearing geometries. Consequently, other alternative solutions were pursued such as Hamrock (1983)'s theory. More about that in section 3.8.2.

3.8.2 Hamrock Load-Deflection Relationship

To test the theory of Hamrock's simplified load-deflection relationship, the equations were implemented in a manner consistent with the Harris tests. The load-deflection relationship, $Q = K_p \cdot \delta^{3/2}$, was rewritten to calculate δ as $\delta = (Q/K_p)^{2/3}$. The Q values were set to match the forces applied in SABR to calculate the reference values. The results for SKF bearing 6216 were is shown in figure 3.28 below.

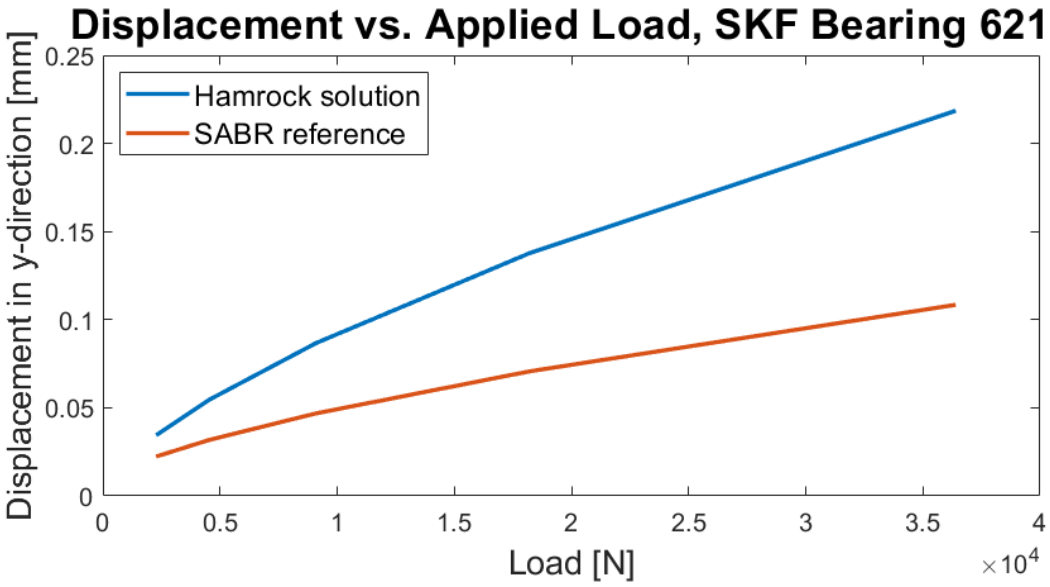

Figure 3.28: Displacement vs. Load of SKF bearing 6216

As illustrated in the figure, the initial results did not align with the reference values. Furthermore, the discrepancy increased with increasing loads. A potential source of error could be connected to how the displacement (δ) is measured. The displacement calculated using the analytical approach represents the length change of a ball under load, whilst the displacement derived using SABR measures the displacement of the inner ring under load. The δ value, ie the displacement, from Hamrock does not account for the possibility of multiple balls being loaded simultaneously. This potential oversight could be a contributing factor to the larger displacements observed in the blue line. However, this does not fully explain the rather large difference for the lower loads as there should only be one active ball at those displacements. The equation was rewritten to determine if the stiffness could be adjusted with a scale factor to increase result accuracy. $\text{Diff} = \delta - \delta_{\text{reference}}$ describes the difference between $\delta = (Q/K_p)^{2/3}$ and $\delta_{\text{reference}}$. In order to match the displacement reference, $\delta_{\text{reference}}$, $\delta - \text{Diff} = (Q/K_{new})^{2/3}$ with $K_{new} = K_p \cdot n$ where n is the scale factor. Initial results indicated that a suitable scale factor was $K_{new} = 2$. The test was rerun with K_{new}, see figure 3.29 and 3.30 for results.

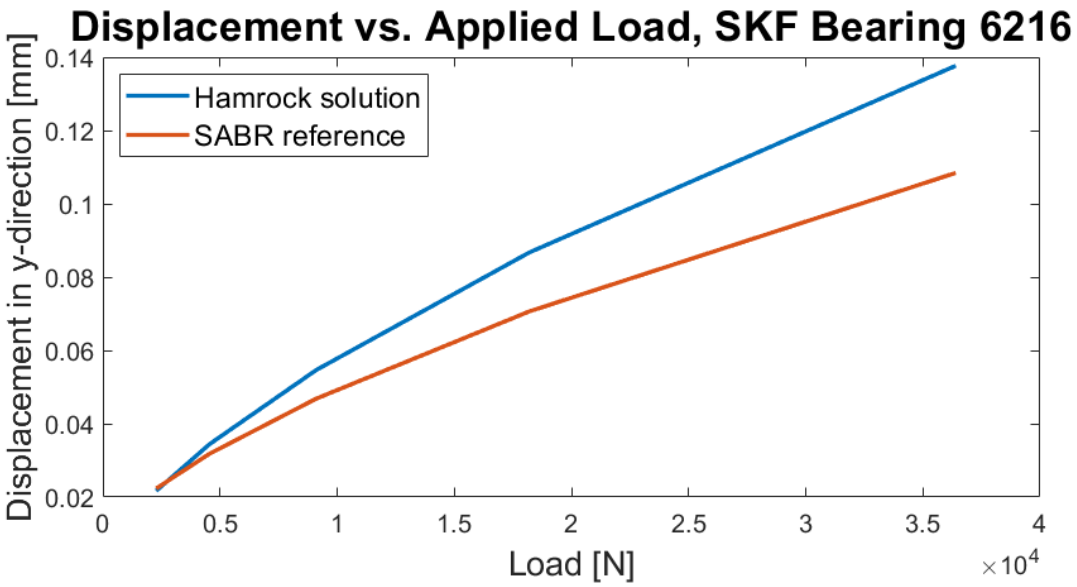

Figure 3.29: Displacement vs. Load of SKF bearing 6216 with scaled Hamrock solution

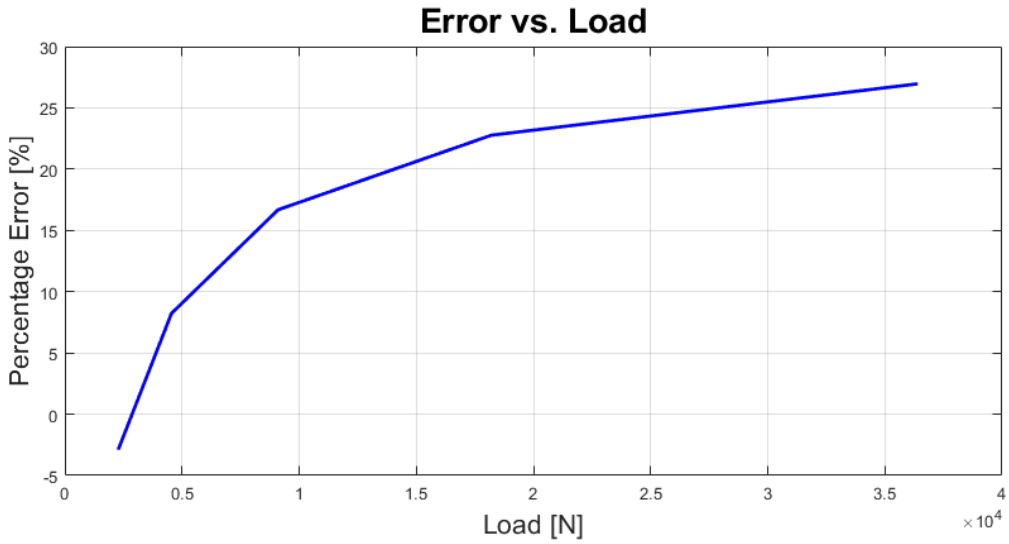

Figure 3.30: Percentage error of the Hamrock analytical solution vs. the reference values from SABR. SKF bearing 6216.

It was concluded that the results align at lower loads, but as the load increases incrementally, the result deviates from the reference. Again, it was suspected that this could be attributed to the fact that the Hamrock theory calculated a ball deflection whilst SABR reference data shows bearing displacement. To test this theory, the Hamrock stiffness relationship was implemented into Lincoln, see appendix F, and was run in Abaqus. The results were compared against reference data from SABR as described in section 3.7, see figure 3.31.

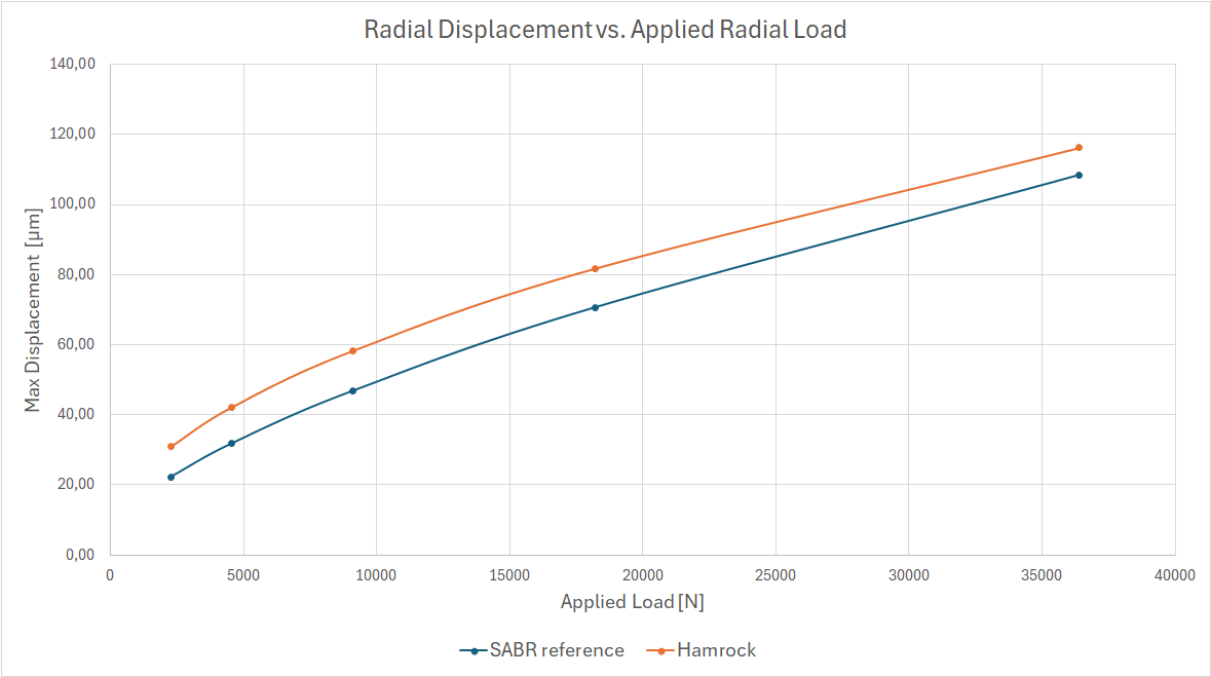

Figure 3.31: Displacement vs. Load plot of SKF bearing 6216, results from Abaqus

The initial results indicated excessive displacement for all loads, but a similar line was observed. The remaining misalignment load cases for that same bearing were simulated as well. The difference between the results and the reference for each load case was plotted, see figure 3.32.

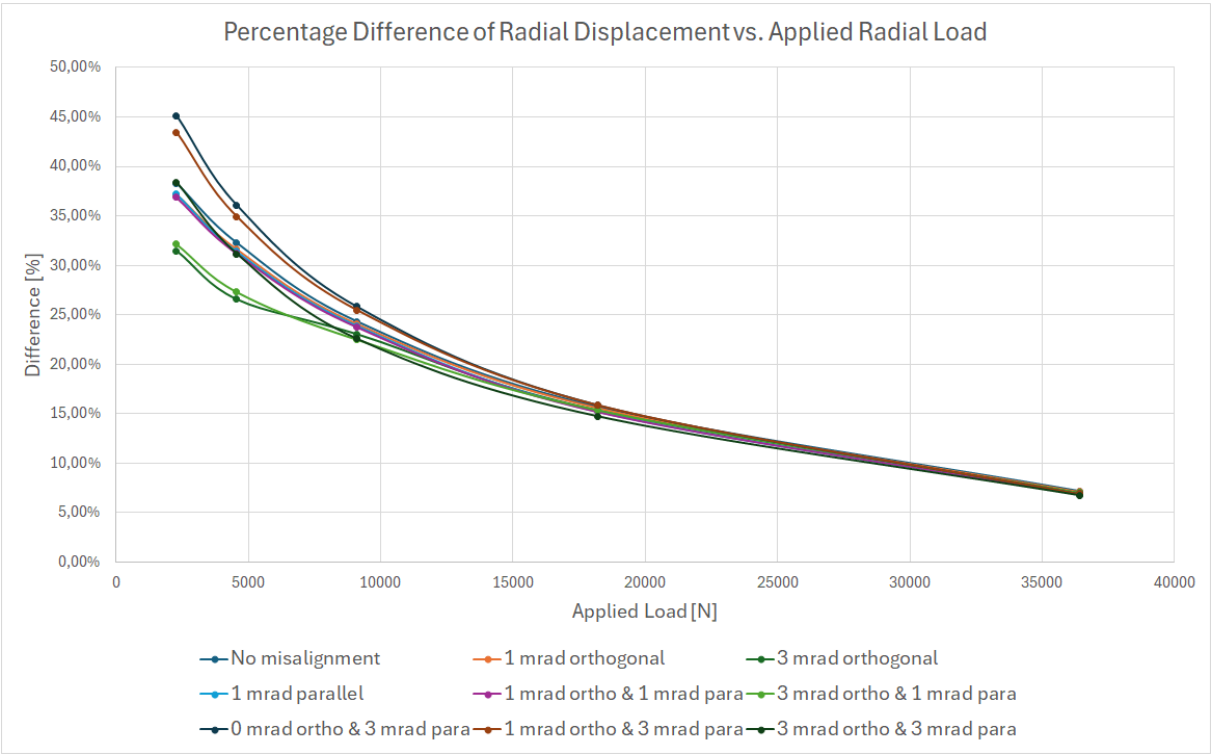

Figure 3.32: Error vs. Load plot of all different misalignment load cases, results from Abaqus

Despite the deviations, a clear similarity was observed in all load cases. This indicated that a different value of the factor n might be able to yield better results. However, the solution had to be tested against other bearings to determine its general applicability or whether it worked only for certain geometries.

To ensure the reliability and usability of the solution, it was essential to test it for more than one bearing geometry. Ideally, tests should include geometries that are not geometrically similar to 6216. The tests were also conducted on the SKF bearing 6020 and 6204. SKF 6020 which has a larger ring diameter than 6216 but smaller and more balls, and SKF bearing 6204 is significantly smaller than 6216. See appendix E for bearing geometries. As shown in figure 3.33, the MATLAB results for bearing 6020 exhibited a comparable pattern to that of bearing 6216, with the scale factor n set to 2. However, the discrepancy was even more obvious at higher loads, 6216: 28% vs. 6020: 42%.

In the case of bearing 6204, the line matched rather well for all loads, especially for the largest load, see figure 3.34(a). As illustrated in figure 3.34(b), the error plot displays a distinct pattern from the previous two plots. The largest error is observed at lower loads, highlighting a key point for consideration. The new behavior was explained by significant changes in geometry. However, there was a concern that the analytical solution might work differently for different bearing geometries.

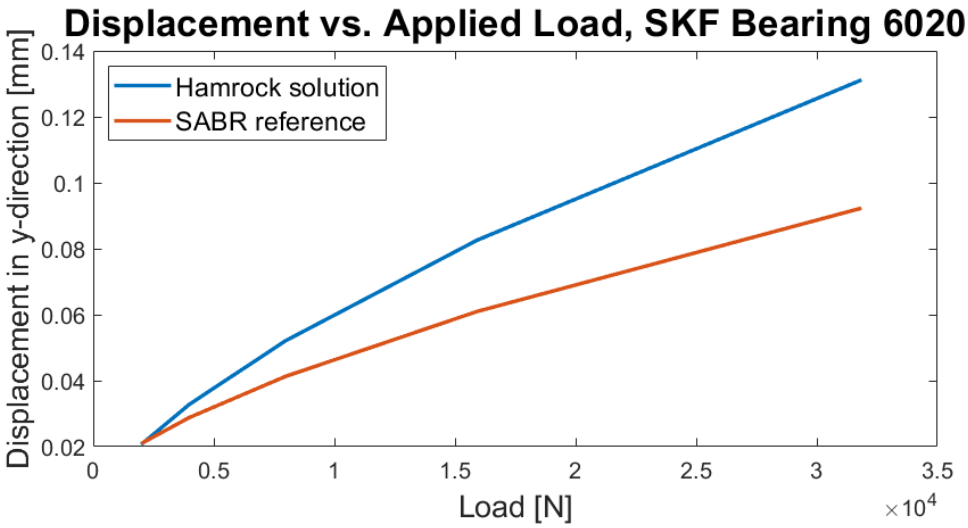

(a) Displacement vs. Load plot of SKF bearing 6020

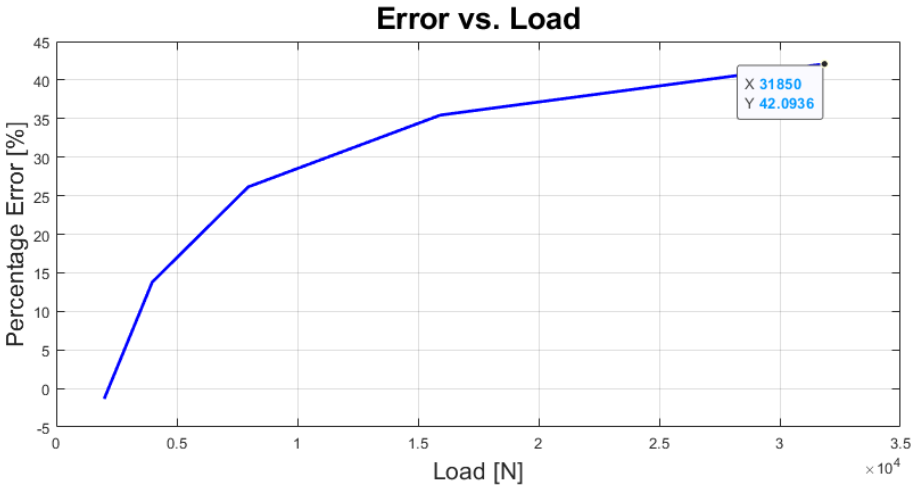

(b) Error vs. Load plot of SKF bearing 6020

Figure 3.33: Matlab results of bearing 6020

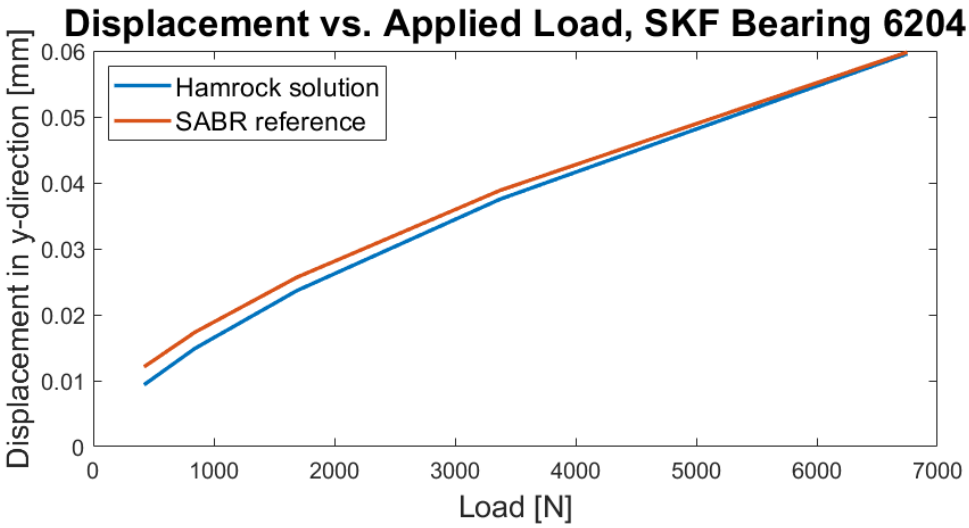

(a) Displacement vs. Load plot of SKF bearing 6204

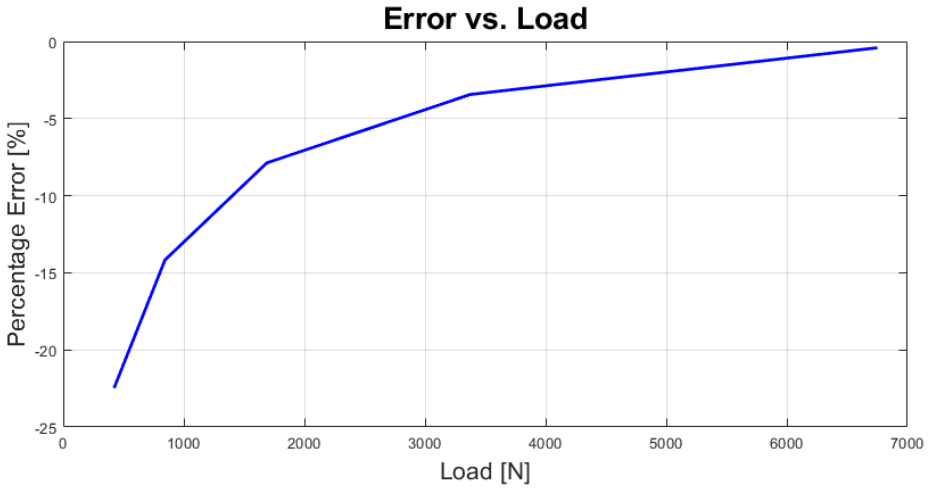

(b) Error vs. Load plot of SKF bearing 6216

Figure 3.34: Matlab results of bearing 6204

Abaqus was used to run the same test as before. This to further compared the two new bearings with bearing 6216, see figures 3.35 & 3.36.

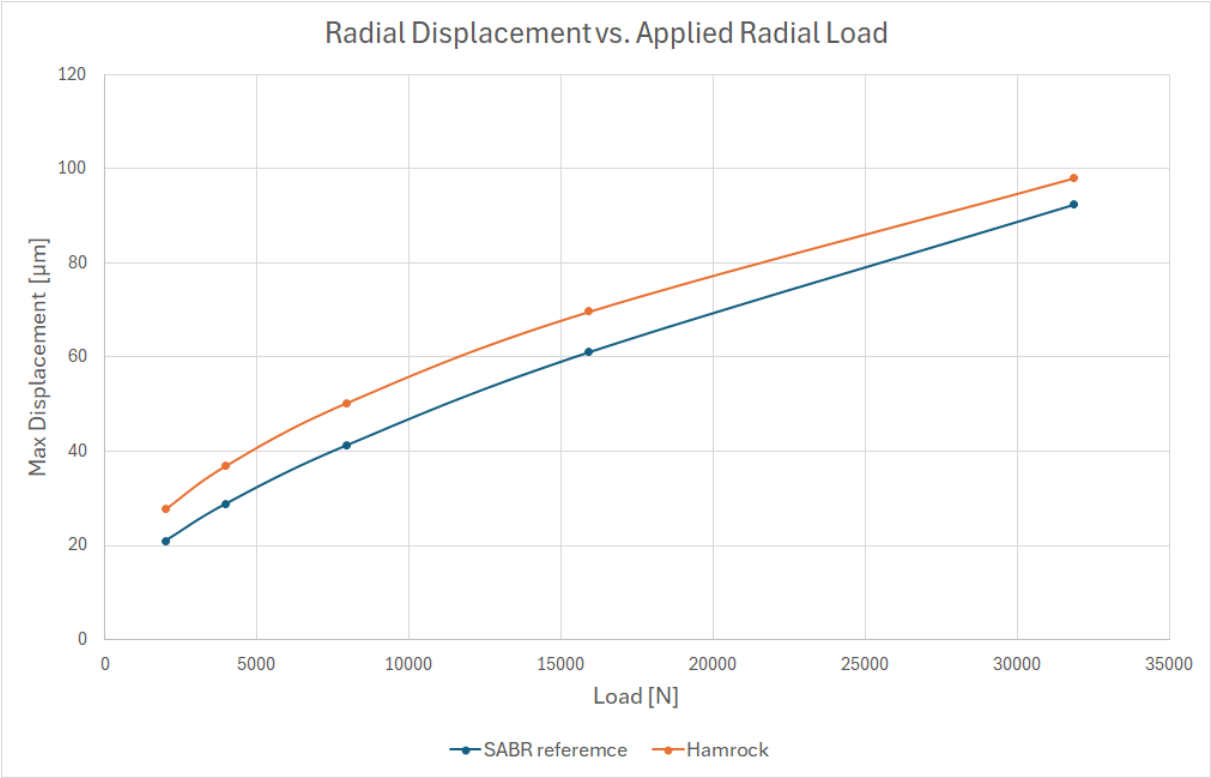

Figure 3.35: Displacement vs. Load plot of SKF bearing 6020, results from Abaqus

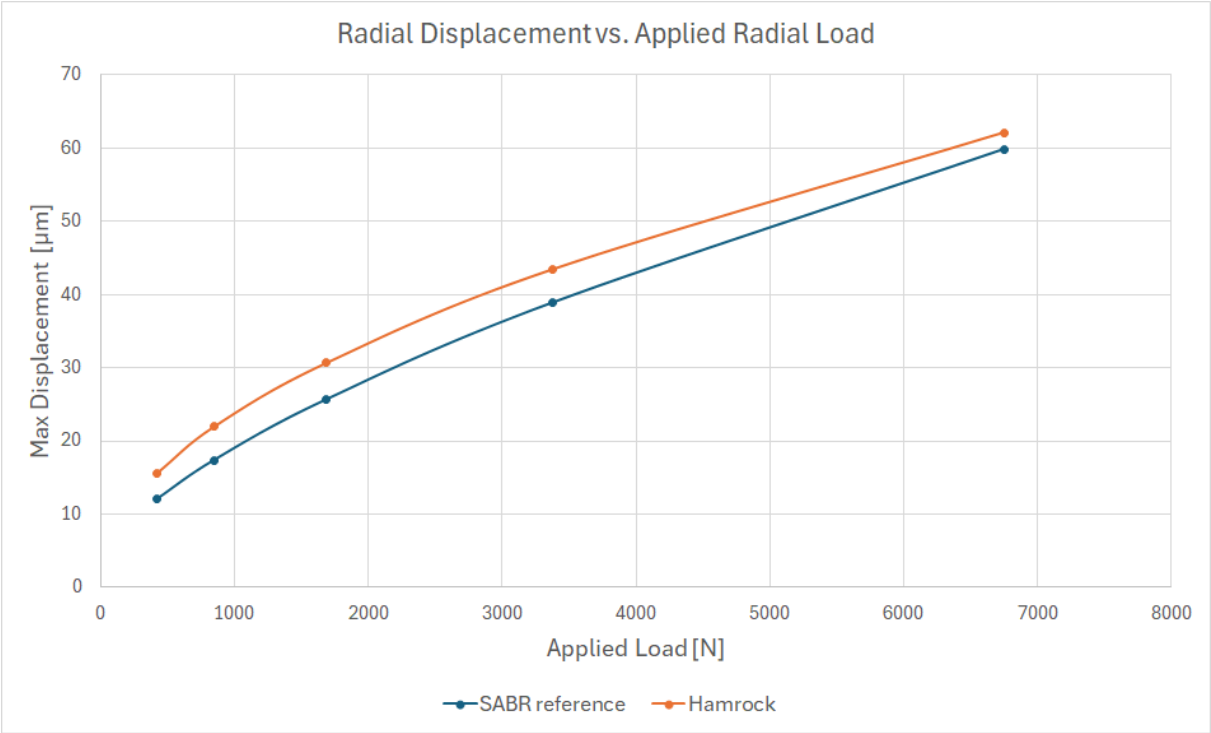

Figure 3.36: Displacement vs. Load plot of SKF bearing 6204, results from Abaqus

Despite the lack of visual similarity, the results from Abaqus for bearing 6216 exhibited a high degree of consistency. The slightly larger displacement magnitude of the three Hamrock lines compared to the reference values indicates insufficient stiffness.

Whilst it appears that the lines could be matched more precisely to their reference values by simply scaling the stiffness, this was not as straightforward as increasing the scale factor, n. This is because x varies nonlinearly, and an increased stiffness will affect the displacements at higher loads more than lower loads, see figure 3.37.

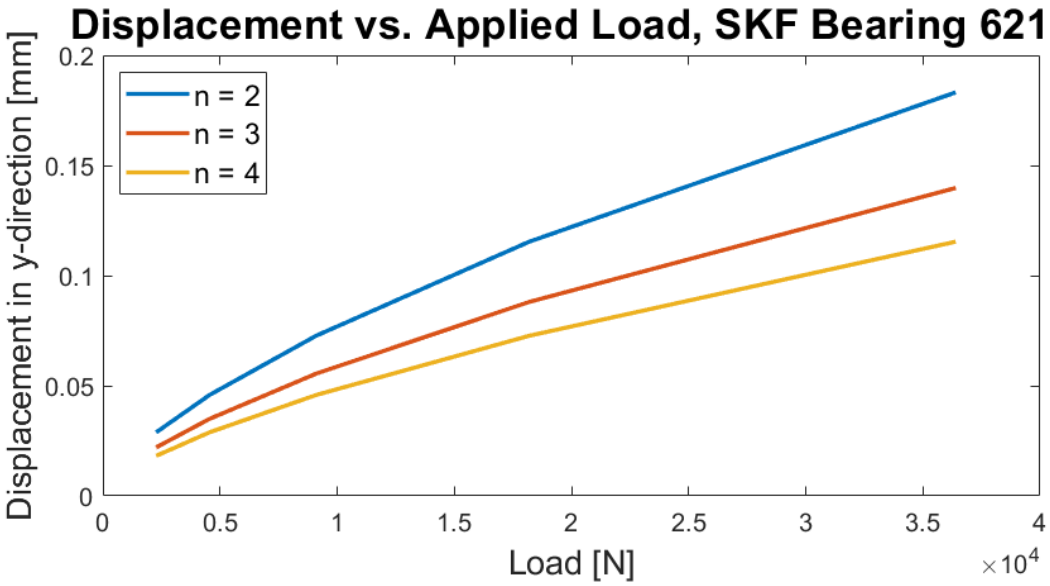

Figure 3.37: Plot showcasing the effect of increasing the multiplication factor n on the displacement

Instead of attempting to match the lines by manipulating the non-linearity of the equation, a new approach was tested. In this approach, the load-deflection relationship was manually changed to identify the force at certain displacements that yielded the best results. By doing so, several key point values on the load-deflection relationship were identified, and a new test was conducted to determine whether the Hamrock analytical formula could fulfill those key point values. By plotting the optimal load-deflection relationship together with the calculated one from Hamrock with $Q = K \cdot \delta^{3/2}$ and $Q = 2 \cdot K \cdot \delta^{3/2}$ it became clear if Hamrock's relationship could match the desired curve, see figures 3.38 & 3.39.

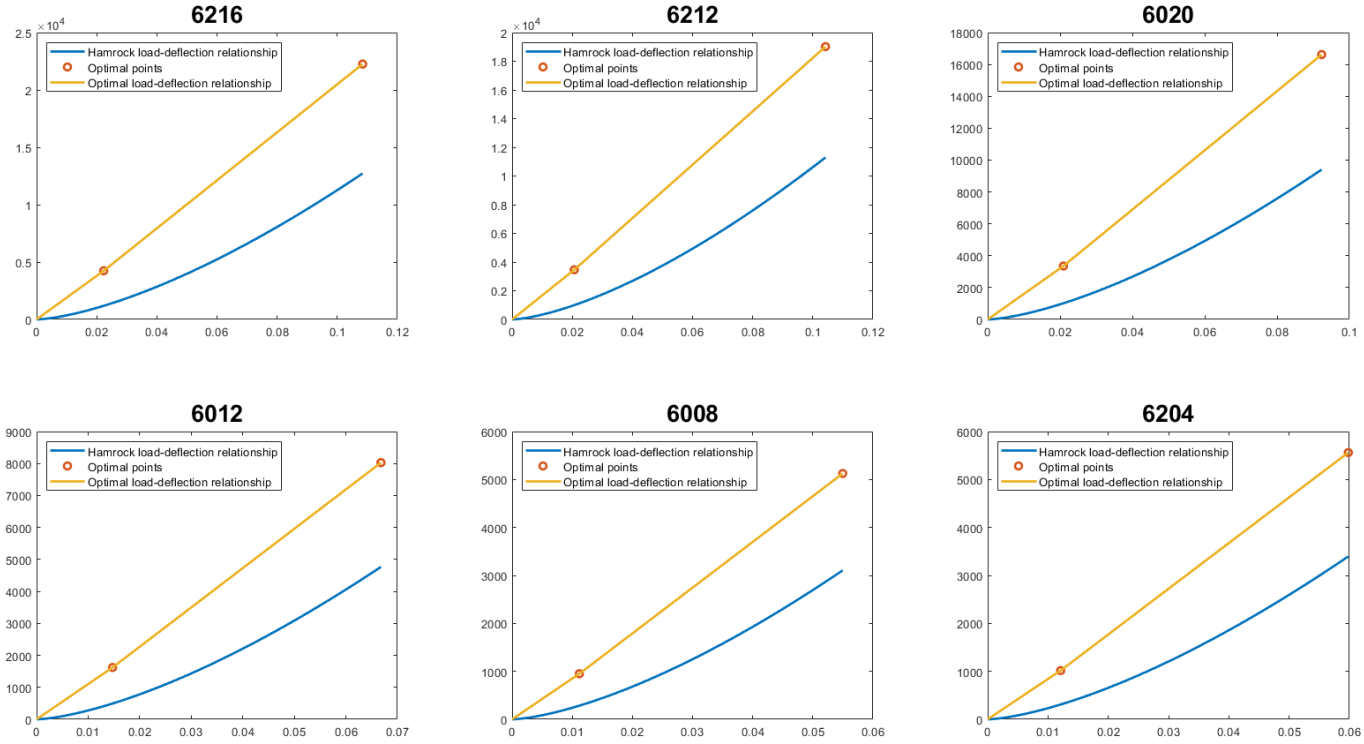

Figure 3.38: Plot showcasing the Hamrock analytical non-linear load-deflection curve vs. the optimal load-deflection curve, no scaling on the stiffness.

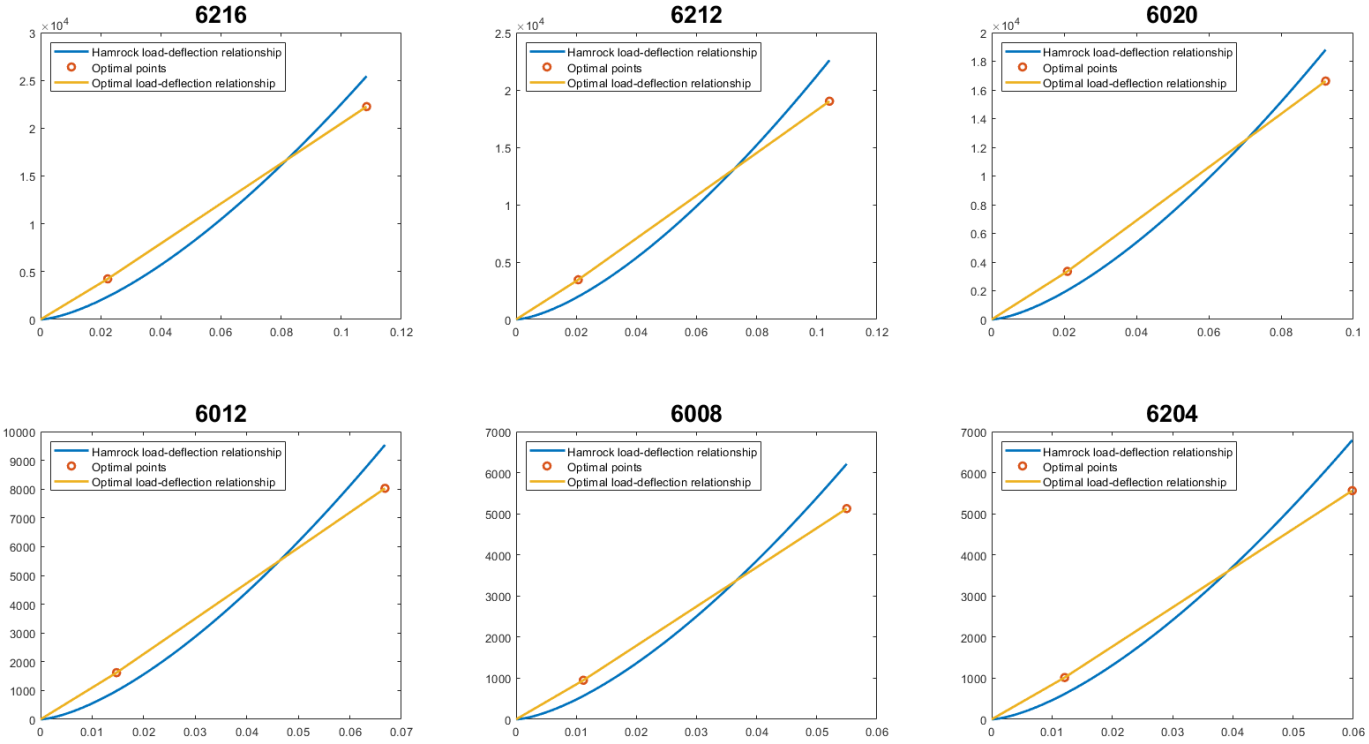

Figure 3.39: Plot showcasing the Hamrock analytical non-linear load-deflection curve vs. the optimal load-deflection curve, stiffness multiplied by 2

From the figures it is evident that Hamrock's relationship needs some scaling to improve on the results but still it does not meet the desired loads. The yellow line, representing the optimal curve, is nearly linear so a linear relationship was also tested. $Q = K \cdot \delta$ resulted in much too high values on Q, see figure 3.40, but $Q = \frac{K}{2} \cdot \delta$ exhibited a better match than $Q = 2 \cdot K \cdot \delta^{3/2}$, see figure 3.41. However, this was still not satisfactory as the line matched better for some bearings than other, as demonstrated in figure 3.41.

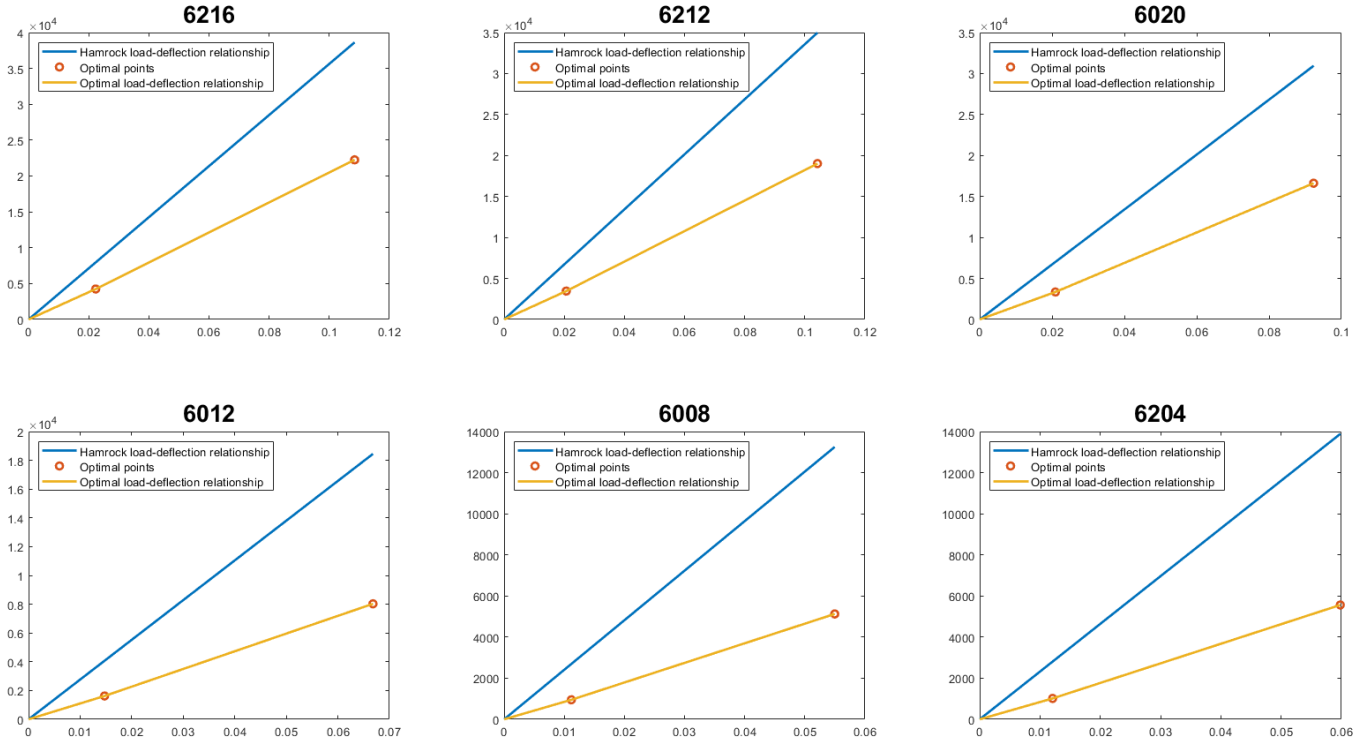

Figure 3.40: Plot showcasing the Hamrock analytical linear load-deflection curve vs. the optimal load-deflection curve, no scaling on the stiffness.

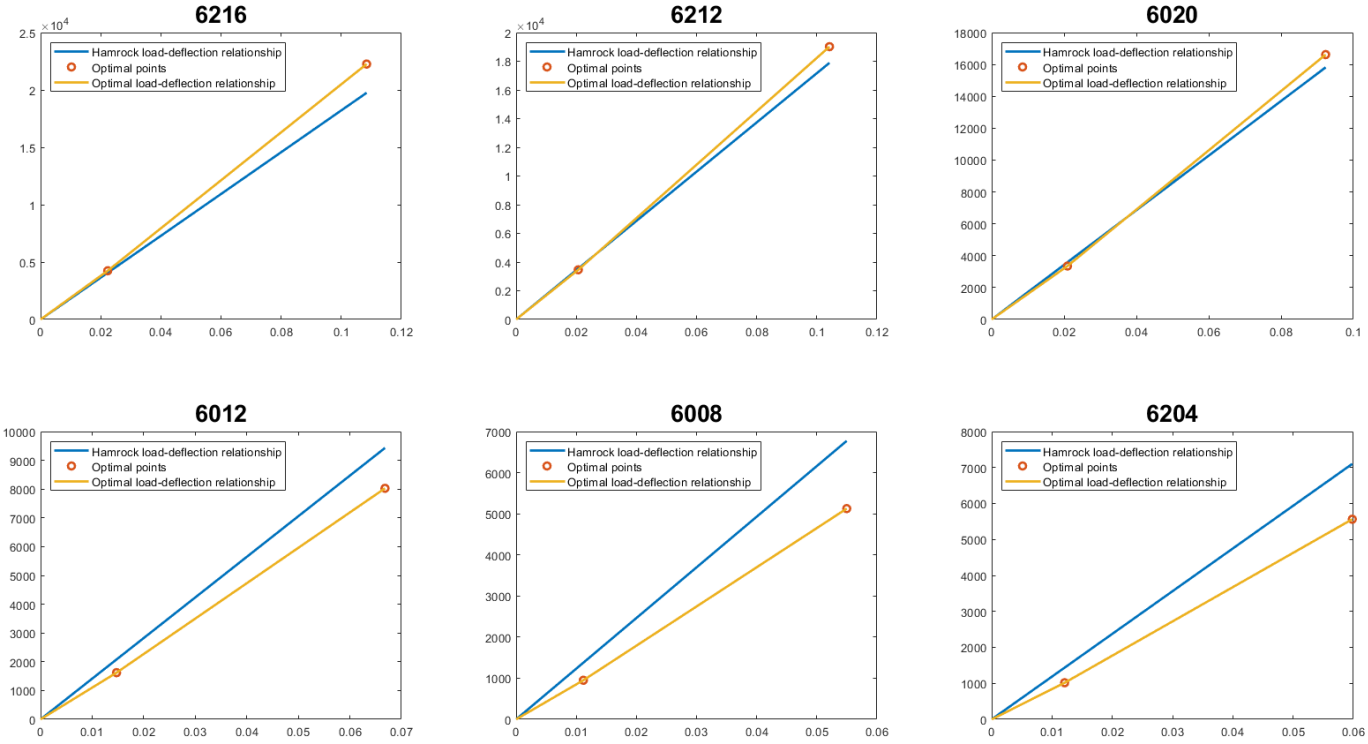

Figure 3.41: Plot showcasing the Hamrock analytical linear load-deflection curve vs. the optimal load-deflection curve, stiffness divided by 2

It was assumed that the theory by Hamrock (1983) does not take enough bearing geometry inputs into account. The decision was made to proceed with a curve fitting approach of a general stiffness equation with more geometrical parameters for modeling spring stiffness.

3.9 Curve Fit Approach

As previous attempts to find an analytical force-displacement relationship failed, a curve-fitting approach was implemented to find the stiffness resulting in the smallest displacement error. A total of three different methods were tested in pursuit of the most accurate results possible:

1. Non-linear least square error fitted to derived stiffnesses for maximum displacement.
2. Non-linear least square error fitted to derived stiffnesses for both maximum and minimum displacement.
3. Non-linear least square error fitted to the displacement - force pairs for both the minimum and maximum displacement.

The curve fitting approach establishes a connection between the bearing geometry and the desired stiffness. A MATLAB script was developed and the function lsqcurvefit (least squares curve fit) was utilized for all versions mentioned. A diverse group of deep groove

ball bearings were chosen for the curve fit optimization to ensure coverage of as many bearing variants as possible. Bearing 6216, 6212, 6012, 6008, and 6204 were used with the following geometry characteristics as parameters (see appendix E for bearing geometry data):

- Ball diameter $[D]$
- Pitch diameter d_m
- Number of balls nr_{balls}
- Radial play rad_{play}

The first stage of implementation used the ideal stiffness for each bearing at maximum displacement. The stiffness's were derived by iterating the Abaqus model until the stiffness resulted in a displacement within 0.5 μm of the SABR reference. The results from the first stage of the curve fit approach showed that the mean error at the lowest load case for SKF 6216 deviated 9.71% from the reference which was deemed unsatisfactory. On the other hand, the results for the higher load cases correlated well, with an approximate error at 0.64% for the highest load case. See table 3.2 for a full list of results.

The second stage of curve fit implementation included the stiffness's derived for the lowest set of displacements. As with the previously derived stiffness's, these were derived using an iterative method. The mean error resulted in 0.94% for the highest load case and 8.36% for the lowest load case, see table 3.2.

Finally, the third version implemented proved to deliver the most accurate results. This specific version used a reference stiffness K $[N/mm]$ and displacement δ $[mm]$ that was provided for the highest and lowest load case for each bearing.

The function listed in equation 3.1 was set up with parameters (a-h) aiming to replace equation 2.29 and provide the optimal fit.

$$Q = K \cdot \delta^h$$
$$\Downarrow$$
$$Q = (a \cdot D^b + c \cdot rad_{play}^d + e \cdot nr_{balls} + f \cdot d_m + g) \cdot \delta^h \tag{3.1}$$

The code successfully identified parameters that match the function very well to the curve, see figure 3.43. However, it was also noted that SKF bearing 6020 does deviate from the characteristic behavior as the stiffness per ball diameter does not align with the other bearings, see figure 3.42(a). To capture the behavior, bearing SKF 6020 was included in the curve fit optimization which lead to a distinctive bend in the curve, see figure 3.42(b). As a result, the model accuracy for the other bearings decreased and it was therefore decided not to include SKF 6020 in the curve fit optimization. See appendix E for bearing geometry properties.

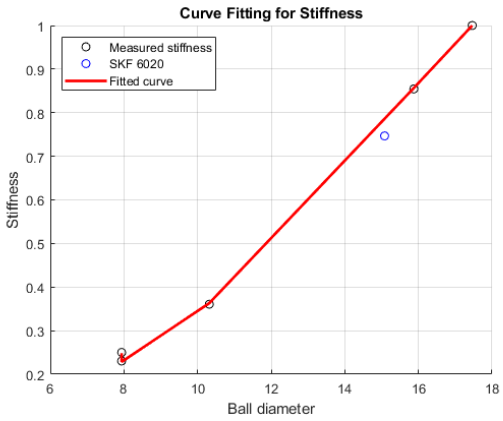

(a) Curve Fit with SKF 6020 Excluded

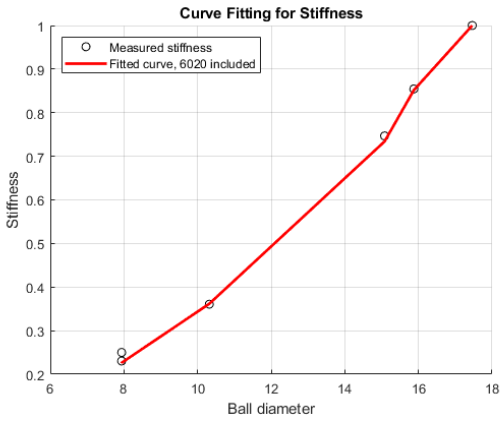

(b) Curve Fit with SKF 6020 Included

Figure 3.42: Left: Curve fit with SKF 6020 excluded. Right: Curve fit with SKF 6020 included. The curve appearance of figure 3.42(b) is not as uniform as the curve shown in figure 3.42(a).

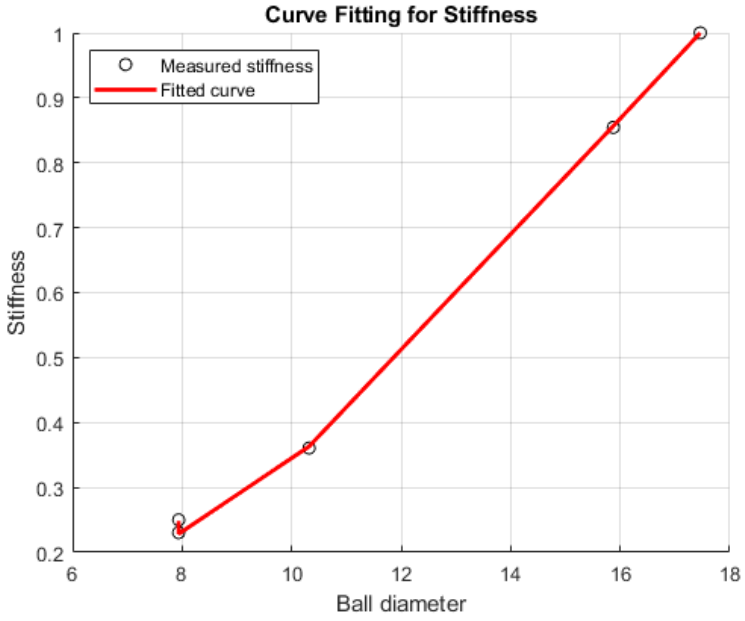

Figure 3.43: Curve fitted stiffness at specific ball diameters. A slighty increasing incline can be noted.

The mean error for the third stage was 1.21% for the highest load case and 4.5% for the lowest. Please refer to figure 3.44 for the displacements of each curve fit stage compared to reference and figure 3.45 for the mean error for each curve fit method respectively. See table 3.2 for a full list of results.

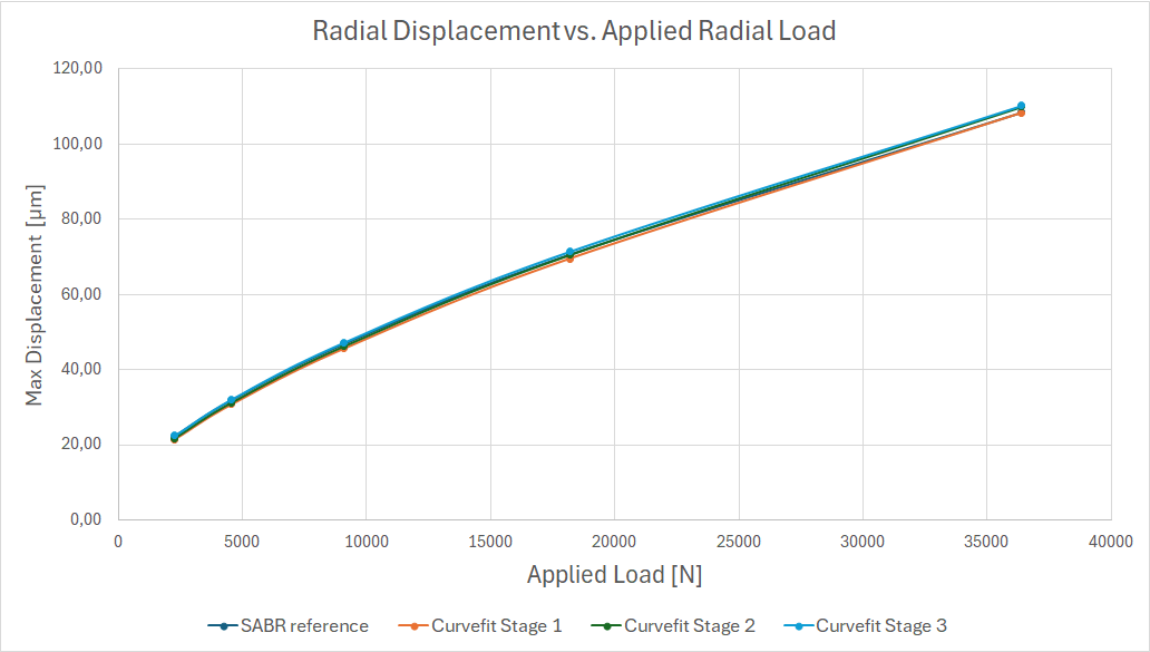

Figure 3.44: Mean displacements of SKF bearing 6216 including misalignments for each curvefit stage, respectively.

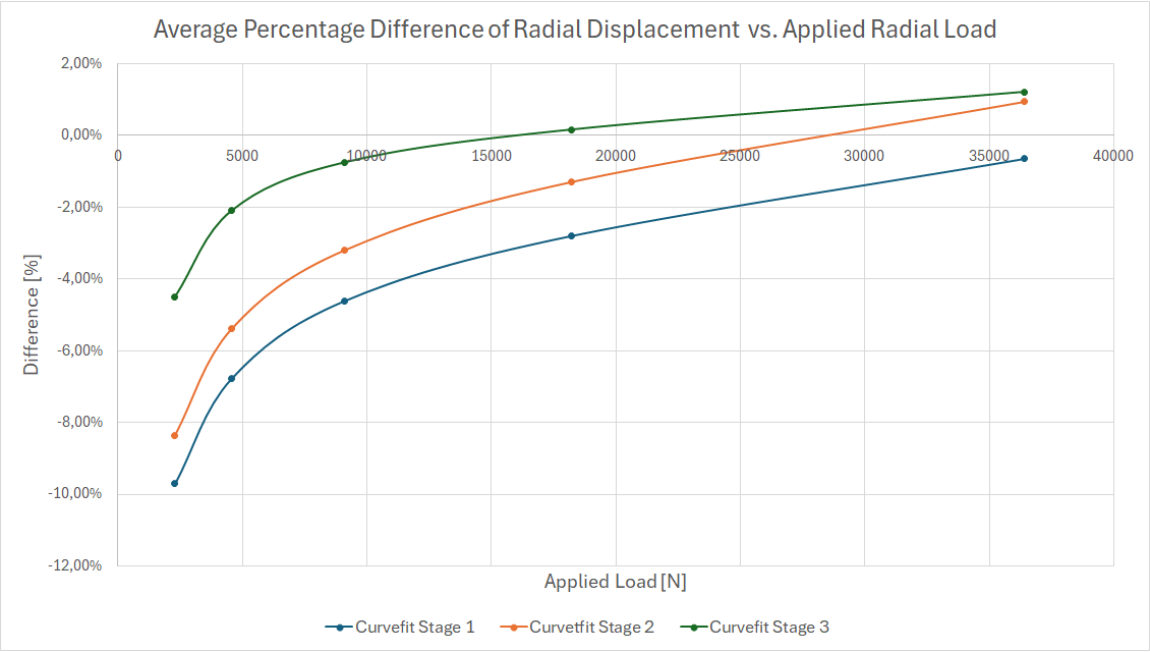

Figure 3.45: Mean error for SKF bearing 6216 against reference values.

Table 3.2: Curvefit results for SKF bearing 6216. Results shown are mean values of all misalignments listed in table 3.1 for the lowest and highest load case, respectively. The error shows the difference between the SABR reference and the Abaqus results.

SKF bearing 6216	**SABR reference** μm		**Abaqus result** μm		**Error** [%]	
Load Case (Low = 2275N, High = 36400N) $[N]$	Low	High	Low	High	Low	High
Harris theory	22.33	108.43	13.17	73.09	-36.16	-31.31
Curvefit stage 1	22.33	108.43	18.47	105.69	-9.71	-0.64
Curvefit stage 2	22.33	108.43	18.75	107.37	-8.36	0.94
Curvefit stage 3	22.33	108.43	19.52	107.66	-4.50	1.21

The results of the third stage of the curve fit approach were satisfactory. Therefore, it was decided to proceed with this fit for further studies.

3.9.1 Distribution of Stiffness in the Ball Model

The calculated stiffness is intended to represent the stiffness of the ball. However, since Lincoln models the ball as a number of springs, it is necessary to distribute the total stiffness in a reasonable manner. Two options were discussed. The first option involves dividing the total stiffness by the number of springs (sp_b). The second option involves measuring the contact area and dividing the stiffness by the number of springs within that area. The latter option ensures that a bearing with a shallow raceway will not be stiffer than expected, and vice versa for a deeper raceway, as illustrated in figure 3.46. Assuming the spring stiffness' are identical, it's evident that the more dispersed spring orientation in the deep raceway would make the Abaqus model less stiff, despite the expectation that a deeper raceway would provide enhanced support to the ball. Unless very large axial loads or misalignments are present.

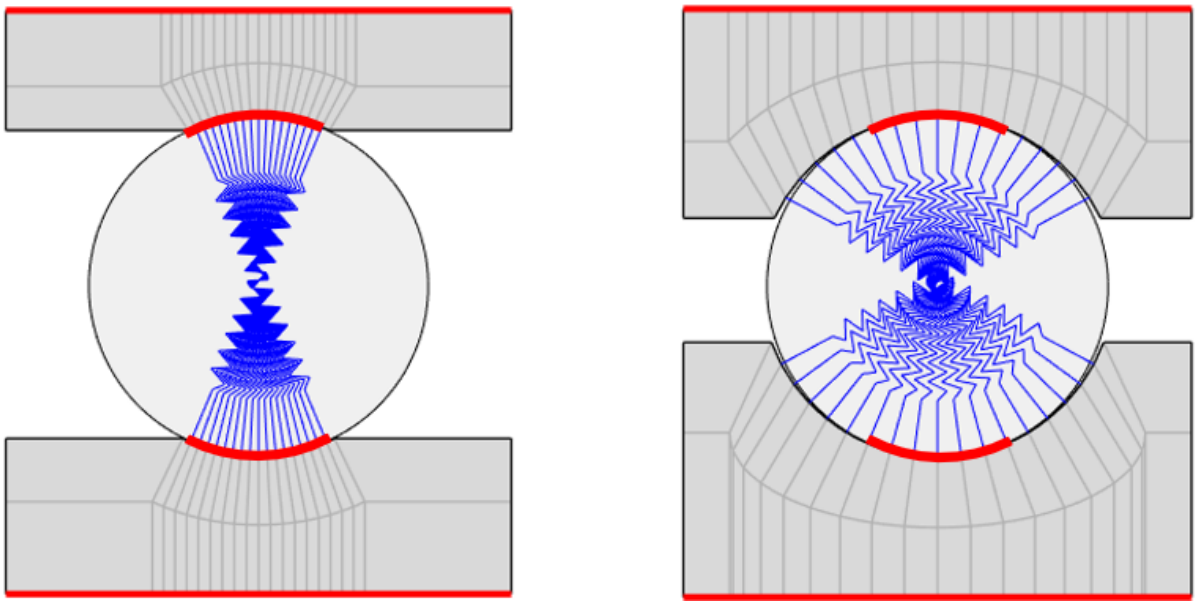

Figure 3.46: A visualization of two bearings, the first with a shallow raceway (left) and the other with a deep raceway (right). The contact area is visible as red lines in the raceways.

An example of how the stiffness per spring is calculated for the bearings seen in figure 3.46 with the two different options is seen in equations 3.2 & 3.3.

Example values:

$$K_p = 1000,\ sp_b = 17,\ \textit{Contact area (ca)} \approx 50^o,$$
$$\textit{Angle between springs } (\alpha)\textit{: Shallow} \approx 2.94^o,\ \textit{Deep} \approx 7.14^o$$

$$K_{per\ spring} = \frac{K_p}{sp_b} = \frac{1000}{17} \approx 58.82 \tag{3.2}$$

$$K_{per\ degree} = \frac{K_p}{ca} \cdot \alpha = \frac{1000}{50} \cdot [2.94,\ 7.14] = [58.80,\ 142.80] \tag{3.3}$$

Equation 3.2 gives the same results for both bearings but since figure 3.46 shows that only 7 of the springs in the figure to the right is in the contact area compared to the 17 springs in the figure to the left, i.e. the total ball stiffness with equation 3.2 will vary:

$$K_{p,\,left} = 58.82 \cdot 17 \approx 1000$$

and

$$K_{p,\,right} = 58.82 \cdot 7 = 411.74$$

The better option is equation 3.3 since it takes the number of springs within the contact area into consideration:

$$K_{p,\,left} = 58.80 \cdot 17 \approx 1000$$

and

$$K_{p,\,right} = 142.80 \cdot 7 \approx 1000$$

A comparison of the two options revealed that the first option, which involved dividing by the total number of springs, resulted in a significantly larger displacement, i.e., a weaker model for the bearing with the deep raceway. In contrast, the second option, which utilized the contact area, yielded more reasonable results, see figures 3.47 & 3.48.

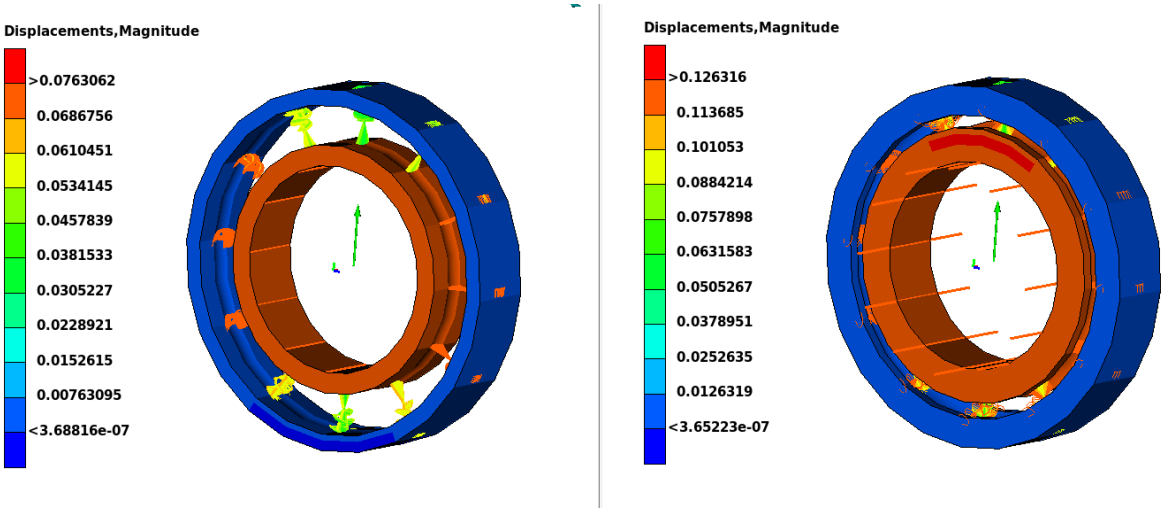

Figure 3.47: Displacement (in $[mm]$) comparison of a bearing with a shallow raceway (left) vs. a deep raceway (right), stiffness divided by number of springs.

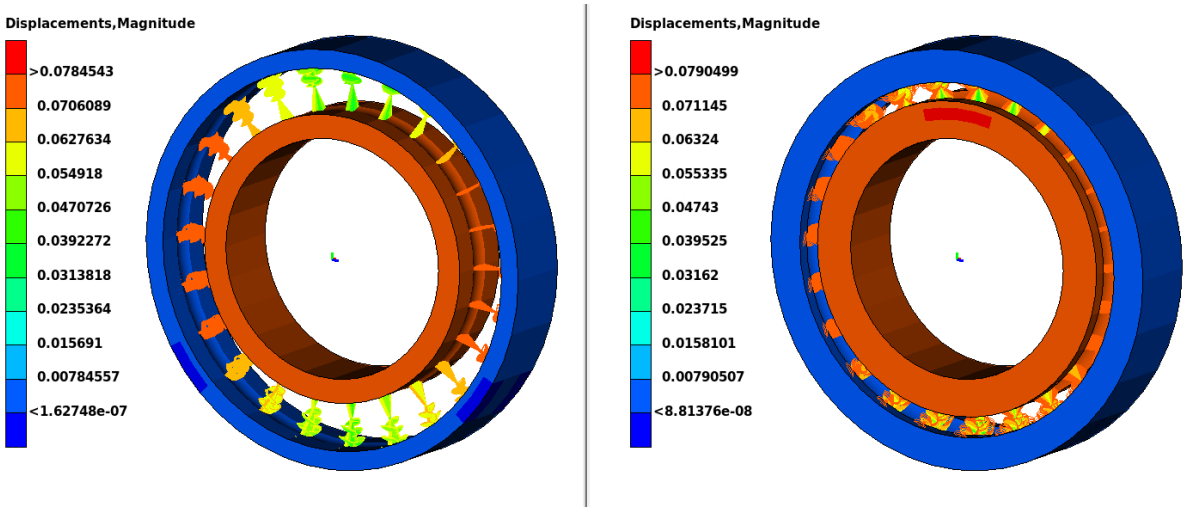

Figure 3.48: Displacement (in $[mm]$) comparison of a bearing with a shallow raceway (left) vs. a deep raceway (right), stiffness divided by number of springs in the contact zone.

The decision to opt for the stiffness/deg solution was verified by running simulations with altered raceway curvatures. Deep groove ball bearing SKF 6216 was modeled for radial load cases in its original configuration and with two altered raceway curvatures across all misalignments listed in table 3.1. See table 3.3 below for bearing alternations and their respective results.

Table 3.3: Deep Groove Ball Bearing 6216 Modified with other Raceway Curvature Gains

SKF bearing	**6216**	**6216**	**6216**
Modification	Default	Smaller curvature gain	Larger curvature gain
Inner curvature gain [%]	4	2	6
Outer curvature gain [%]	6	4	8
Mean Error [%]	1.99	3.19	1.50

Altering the curvature gain showed no significant impact on result accuracy.

3.10 Effects of Changing Meshing Settings and Simulation Resolution

The subsequent section of the method evaluates the impact of modifying specific parameters in the settings of the simulations and the geometry. A variety of factors was assessed, including simulation time and accuracy. Additionally, a mesh convergence study was conducted.

3.10.1 Changing the Number of Springs per set

To approximate the contact behavior of a ball, the number of springs per set was increased to provide more comprehensive coverage of the contact area. In this approach, the stiffness

of each individual spring is calculated based on the number of springs positioned within the contact angle—i.e. those likely to experience loading. By increasing the number of springs, it is expected that the contact surface is more uniformly engaged, which may contribute to a more consistent displacement–force response. This is attributed to the fact that closely spaced springs will engage more gradually during loading, compared to configurations with fewer, more widely spaced springs, see figure 3.49. Whilst this configuration is assumed to better approximate the stiffness distribution of a ball, further analysis would be required to quantitatively validate this assumption. Furthermore, an increase in the number of springs results in a greater number of elements along the raceway, thereby creating a smoother ring-like geometry. However, as illustrated in figure 3.49, this configuration results in elements with a width that is significantly smaller compared to their height and length circumferentially. This relationship between width, height, and length is referred to as the aspect ratio where the optimal aspect ratio is 1. The default max aspect ratio quality limit in Abaqus is an aspect ratio of 10 for hexahedron elements, (Dassault Systemes, 2024d). Ratios greater than 10, particularly elongated or stretched shapes, can result in increased simulation time and numerical inaccuracies, especially in stress and strain calculations, (SDC Verifier, n.d.). The element with the largest aspect ratio of the geometry to the left in figure 3.49 was measured at 23, exceeding the default value of 10. However, it was not as extreme as the aspect ratio of the geometry to the right, which was measured at 188 at most.

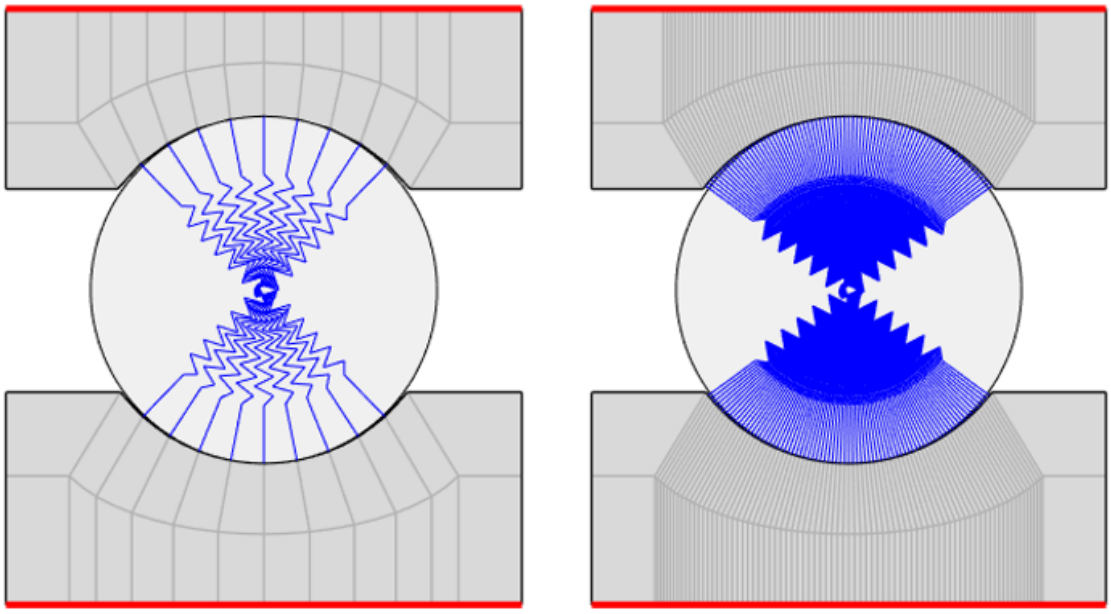

Figure 3.49: Visualization of a bearing with 9 springs (left) vs. 79 springs (right) per set.

One possible method of decreasing the aspect ratio is to increase the number of elements radially, as demonstrated in figure 3.50. However, this approach resulted in an increase of the maximum measured aspect ratio from 188 to 229, please refer to section 5.3.1 for an explanation to this unexpected result.

In theory the model with the finer mesh is the better option in FEA, (SDC Verifier, n.d.). However, it should be noted that high-resolution meshes with numerous elements

can strain hardware resources, increase computational requirements, and lead to longer simulation times.

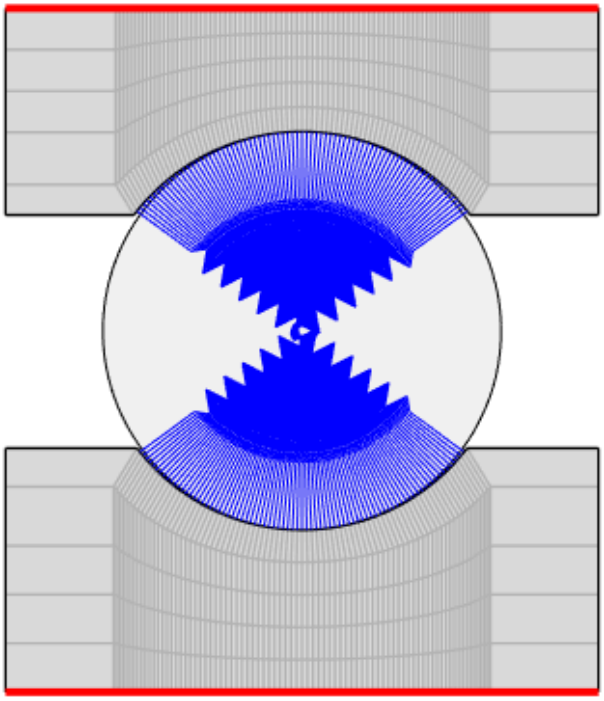

Figure 3.50: Visualization of a bearing with 79 springs per set and added elements radially.

Considering these challenges, this section aimed to identify an optimal balance between the advantages and disadvantages of an increased number of springs.

3.10.2 Changing the Number of Spring Sets per Ball

Lincoln offers the option to distribute the forces further by increasing the number of spring sets per ball, as illustrated in figure 3.51. This adjustment is advantageous for reasons of numerical stability, as it effectively divides the relatively long elements along the circumference of the rings into smaller pieces, To account for the increase in the number of springs in the bearing, the calculated stiffness is divided by two factors: the number of springs in the contact angle and the number of spring sets per ball.

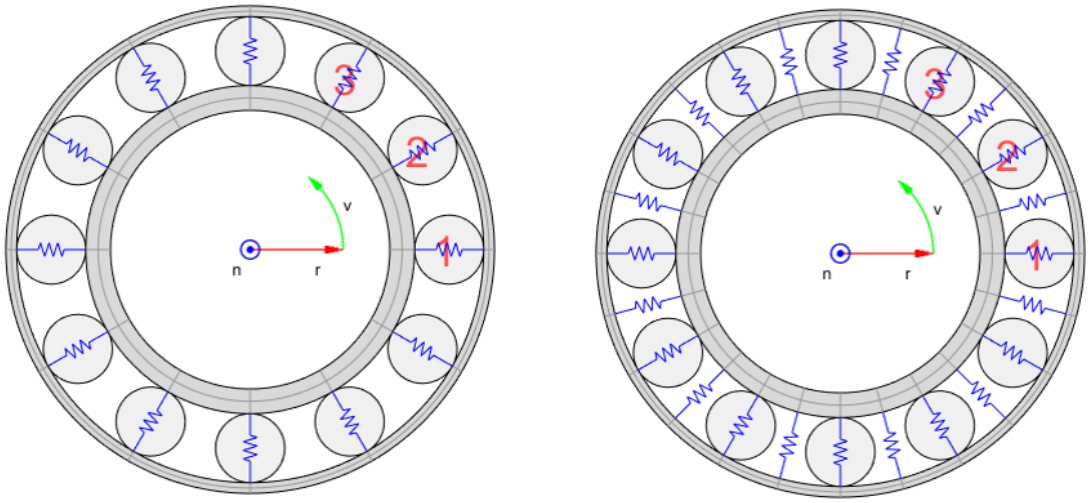

Figure 3.51: Visualization of a bearing with 1 spring set per ball (left) vs. 2 spring sets per ball (right).

The new spring set has the effect of smoothing the circumferential distribution of stiffness. Each spring set is weaker to account for this increase, but there will still be a difference in when a new set of "balls" will initiate contact, which might affect the results in a negative way.

3.10.3 Effects of Refining the Mesh

As is customary in the field of finite element studies, a mesh convergence study was conducted. This was to ensure the reliability of the results and assess the impact of a refined mesh on simulation time. Lincoln offers a number of adjustable parameters, which are listed below:

- Elements axially, flange
- Elements radially
- Elements/spring

Increasing the elements radially in the rings and axially in the flanges can be done separately for the outer and inner ring. In addition to the aforementioned parameters, the following changes mentioned earlier also affect the mesh: increasing the number of springs per set leads to more elements axially in the raceway, and increasing the number of spring sets per ball increases the elements circumferentially in the rings. For options involving axial and radial element increase, the growth factor can be adjusted to accommodate different element sizes as it can be used to increase or decrease the size of each element with a factor relative the innermost element. An example of the roughest mesh possible for a ball bearing in Lincoln is shown in figure 3.52. For this specific bearing the total amount of solid elements was 192.

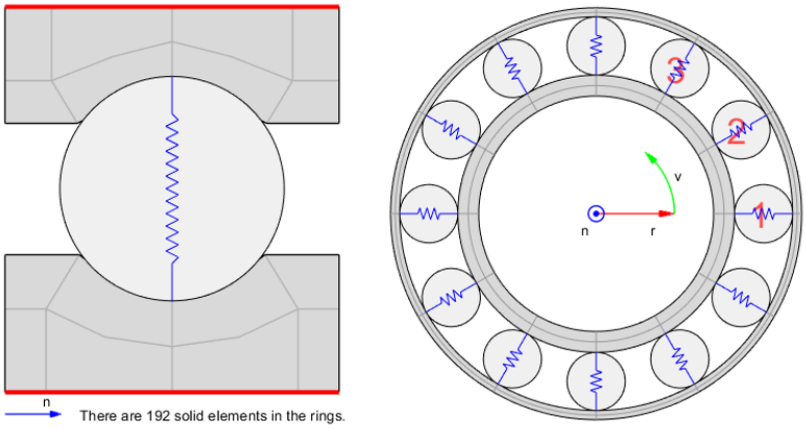

Figure 3.52: Visualization of the roughest mesh possible in Lincoln.

An increase in the amount elements circumferentially is particularly beneficial when there are numerous axial elements i.e., numerous springs per set, and the aspect ratio is high, as discussed in section 3.10.1. Figure 3.53 show the mesh if two more springs are added, the total amount of solid elements in this mesh was 288.

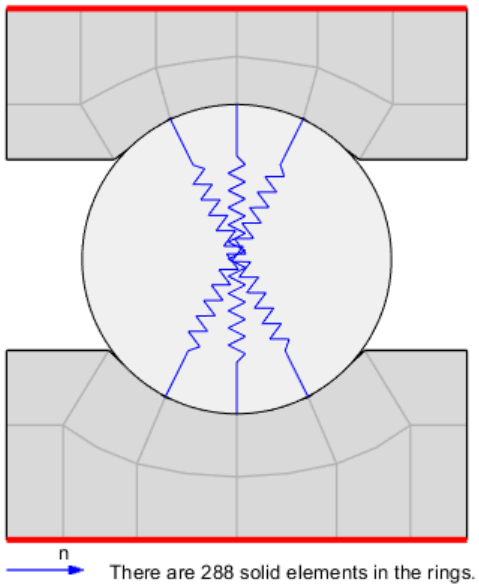

Figure 3.53: Visualization of the mesh with two more springs than the mesh shown in figure 3.52

An increase in the amount of axial elements in the flanges will always lead to the same increase in total amount of elements but an increase in radial element will increase the total amount of elements dependent on the amount of springs per spring set, see figures 3.53(a) & 3.53(b). As the number of elements/springs is increased, the total amount of solid elements is effectively doubled, as illustrated in figure 3.54 bottom row.

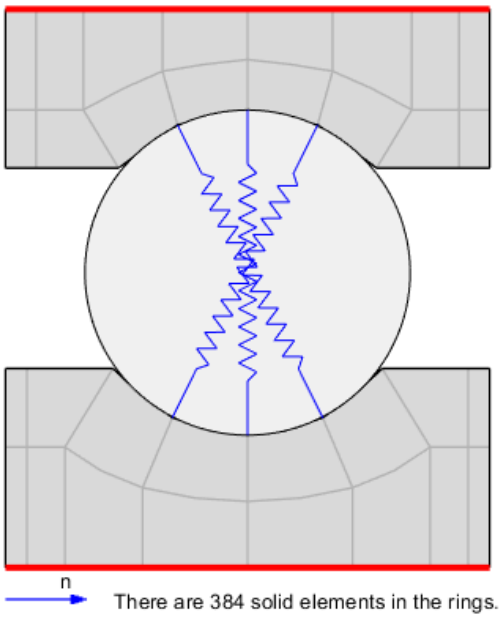

(a): Mesh with two elements axially in the flanges instead of one. Change in number of elements: 96

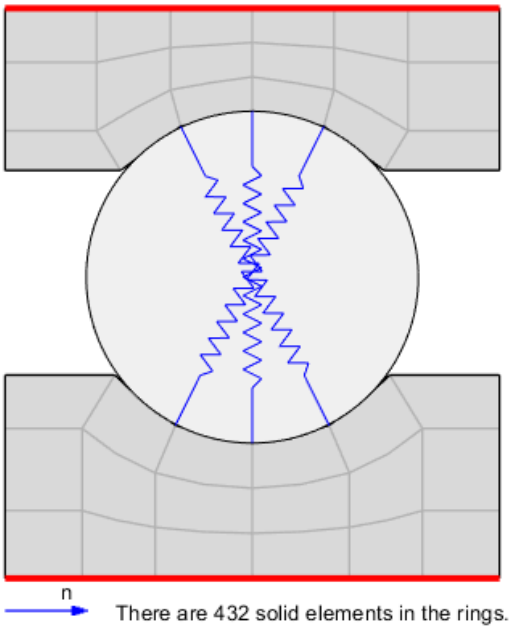

(b): Mesh with three elements radially instead of two. Change in number of elements: 144

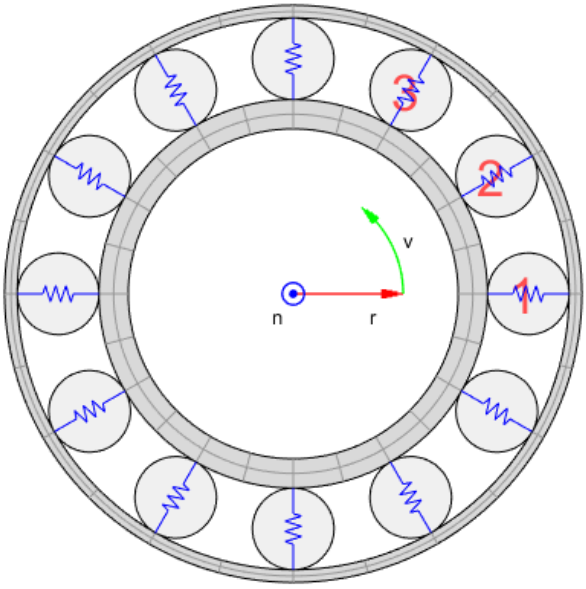

(c): Mesh with two elements/spring instead of one. Change in number of elements: 288

Figure 3.54: Visualization of the Different Mesh Options Available in Lincoln, note that an increase

As discussed in previous sections, it is essential to ensure a sufficient distribution of springs over the raceway to obtain reliable results. Having only one spring is inadequate; at least nine springs per set are necessary for accurate results. Therefore, the mesh convergence study will utilize the mesh in figure 3.55 as the starting point. The objective of the study is to augment the number of elements whilst adhering to specific mesh quality criteria

concerning the aspect ratio.

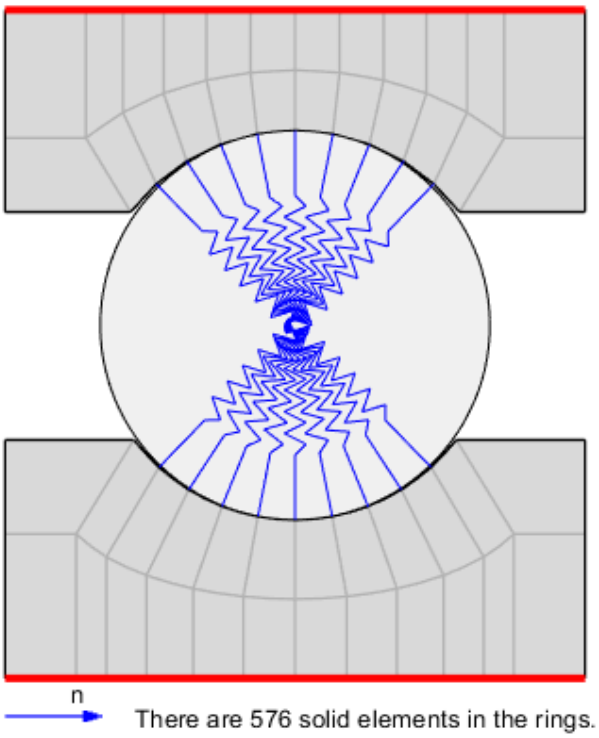

Figure 3.55: Rough mesh in the context of mesh convergence study. Total amount of solid elements: 576, max aspect ratio: 23

3.11 Simulating Combined Load Cases

In general, bearings are rarely subjected to pure radial or axial loads. Therefore, it is essential to test and evaluate the performance of the model for combined load cases, where the bearing is subjected to both radial and axial load. Given five load levels for radial and axial load, as well as nine misalignments, the total number of simulations to run across all bearings would be equal to the number of simulations for each load case, multiplied by the number of load levels. See equation 3.4 below.

$$nr_{sims} = LL_{radial} \cdot LL_{axial} \cdot nr_{misalignments} \cdot nr_{bearings} = 5 \cdot 5 \cdot 9 \cdot 8 = 1800 \tag{3.4}$$

In order to reduce the number of simulations to a more manageable level, it was decided to run a set of samples for each misalignment. This section provides detailed information on the configuration of each sample.

MA1, MA2 and so on refers to misalignment cases depicted by table 3.1. MA1 refers to the case without misalignments, which was assigned five sample simulations at various load cases whilst the other eight misalignments were assigned two samples each. Tables 3.4 to 3.12 below details the chosen samples. C refers to the dynamic load rating. The radial loads ranges from 1/32 to 1/2 of the dynamic load rating, whilst the axial loads ranges from 1/64 to 1/4. The number in the green cells denotes the given load case number and is used to refer back to the results.

Table 3.4: Set of load case samples used for bearings with no applied misalignment, MA1 per table 3.1.

MA1	Radial C/2	Radial C/4	Radial C/8	Radial C/16	Radial C/32
Axial C/4	5				3
Axial C/8					
Axial C/16			2		
Axial C/32					
Axial C/64	4				1

Table 3.5: Set of load case samples used for bearings with MA2.

MA2	Radial C/2	Radial C/4	Radial C/8	Radial C/16	Radial C/32
Axial C/4					6
Axial C/8					
Axial C/16					
Axial C/32	7				
Axial C/64					

Table 3.6: Set of load case samples used for bearings with MA3.

MA3	Radial C/2	Radial C/4	Radial C/8	Radial C/16	Radial C/32
Axial C/4					
Axial C/8				9	
Axial C/16					
Axial C/32					
Axial C/64				8	

Table 3.7: Set of load case samples used for bearings with MA4.

MA4	Radial C/2	Radial C/4	Radial C/8	Radial C/16	Radial C/32
Axial C/4		11			
Axial C/8					
Axial C/16					
Axial C/32					
Axial C/64			10		

Table 3.8: Set of load case samples used for bearings with MA5.

MA5	Radial C/2	Radial C/4	Radial C/8	Radial C/16	Radial C/32
Axial C/4				13	
Axial C/8					
Axial C/16					
Axial C/32					
Axial C/64		12			

Table 3.9: Set of load case samples used for bearings with MA6.

MA6	Radial C/2	Radial C/4	Radial C/8	Radial C/16	Radial C/32
Axial C/4			15		
Axial C/8					
Axial C/16					
Axial C/32					
Axial C/64		14			

Table 3.10: Set of load case samples used for bearings with MA7.

MA7	Radial C/2	Radial C/4	Radial C/8	Radial C/16	Radial C/32
Axial C/4					
Axial C/8					
Axial C/16			17	16	
Axial C/32					
Axial C/64					

Table 3.11: Set of load case samples used for bearings with MA8.

MA8	Radial C/2	Radial C/4	Radial C/8	Radial C/16	Radial C/32
Axial C/4				19	
Axial C/8					
Axial C/16					
Axial C/32					
Axial C/64	18				

Table 3.12: Set of load case samples used for bearings with MA9.

MA9	Radial C/2	Radial C/4	Radial C/8	Radial C/16	Radial C/32
Axial C/4					
Axial C/8					
Axial C/16					
Axial C/32					21
Axial C/64		20			

Results

The results from three main categories are presented below. Studies regarding the accuracy of the bearing geometries, simulation results derived using Lincoln models, and the results from a study on how mesh refinement affects simulation accuracy, time, and stability.

4.1 Geometry Check in Abaqus

During the course of this project, several updates have been implemented to Lincoln and its methods for calculating the ring geometries and spring positions. A study was conducted in which the bearing geometry was partially verified utilizing CAD. Additionally, a test was conducted to measure Abaqus displacement results close to initial contact, as outlined in section 3.3. Please refer to table 4.1 for the measurements measured in CAD. For the displacements derived using SABR, please refer to table 4.2.

Table 4.1: Raceway geometry verification of SKF 6216 measured using CAD.

	Displacement $[\mu m]$	
Ball Angle [°]	**Radial**	**Axial**
0	5.2	0
5	4.668	30.471
10	3.073	60.904
15	0.417	91.264
20	-3.297	121.512

Table 4.2: Raceway geometry verification of SKF 6216 measured using SABR.

Applied Load $[N]$			**Displacement** $[\mu m]$		
Radial	**Axial**	**Ball Compression (BC)** $[\mu m]$	**Radial incl BC**	**Radial excl BC**	**Axial**
50	0	1.8	7.03	5.23	0
50	2	1.8	6.36	4.56	33.24
50	4	1.6	4.43	2.83	64.99
50	6	1.4	1.87	0.47	90.56
50	8	1.2	0.78	-0.42	98.84
50	10	1.2	0.59	-0.61	100.61

The data listed in the tables above is illustrated in the figures below. See figure 4.1 for a graph comparing the results of CAD measurements (table 4.1) and SABR reference data (table 4.2).

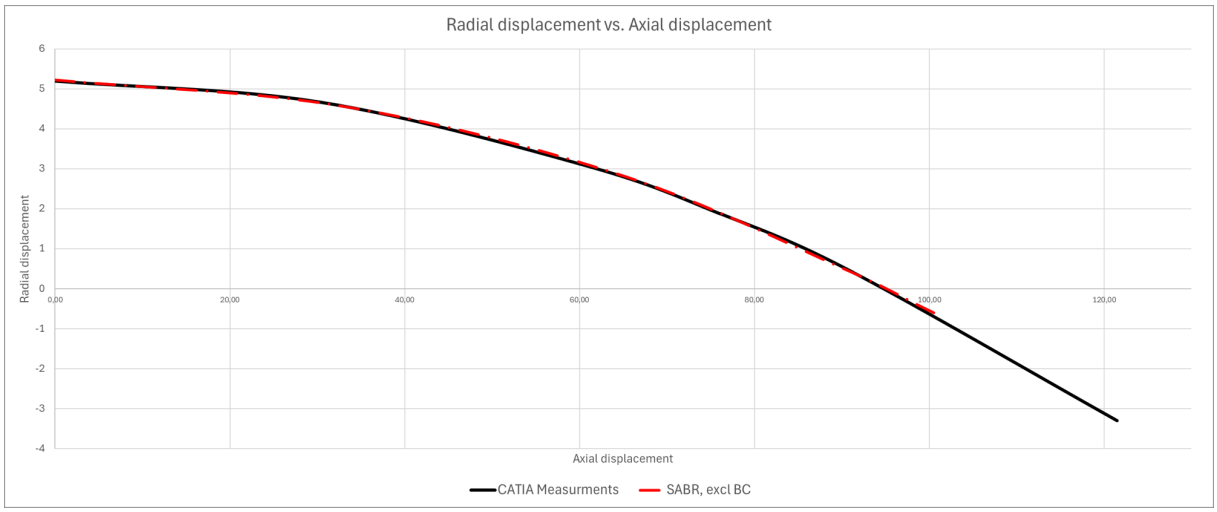

Figure 4.1: Comparison of raceways geometries between CAD measurements and SABR simulation results. The two measurements correspond to each other.

Additionally, the results of simulating the Lincoln bearing geometry in Abaqus using the same approach as used to derive results from SABR is shown in figure 4.2. It was noted that all results correspond at zero axial load, but the Lincoln results deviate from the SABR and CAD reference as the axial load increases.

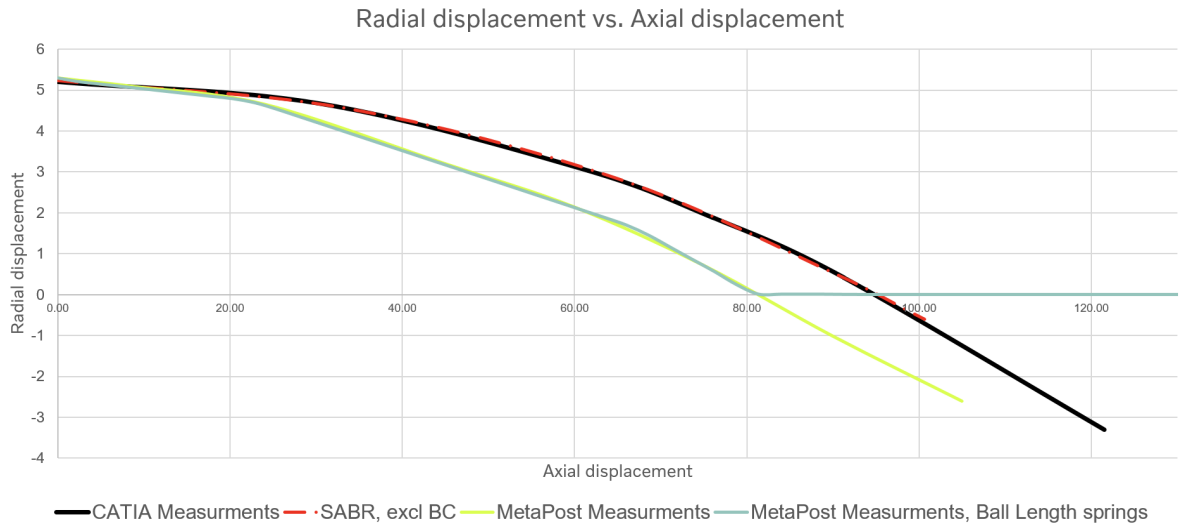

Figure 4.2: Raceway geometry comparison between SABR, CAD and Abaqus.

As a result, it was determined that the geometrical behavior of a Lincoln bearing is partially verified, as the CAD measurements correspond to the reference results from SABR, but the results of the Abaqus simulations does not agree with the SABR reference. For discussion and a root cause analysis, please refer to section 5.1.

4.2 Radial and Axial Loading Results

The primary method for assessing the model's accuracy involved measuring the inner ring displacement under different misalignments and load magnitudes. These displacements

were then compared with reference values provided by SABR.

First, only a radial load was applied and tested. Figure 4.3 below illustrates the model's average performance for different misalignment scenarios of eight bearings with distinct geometries. Please refer to appendix E for a bearing geometry overview.

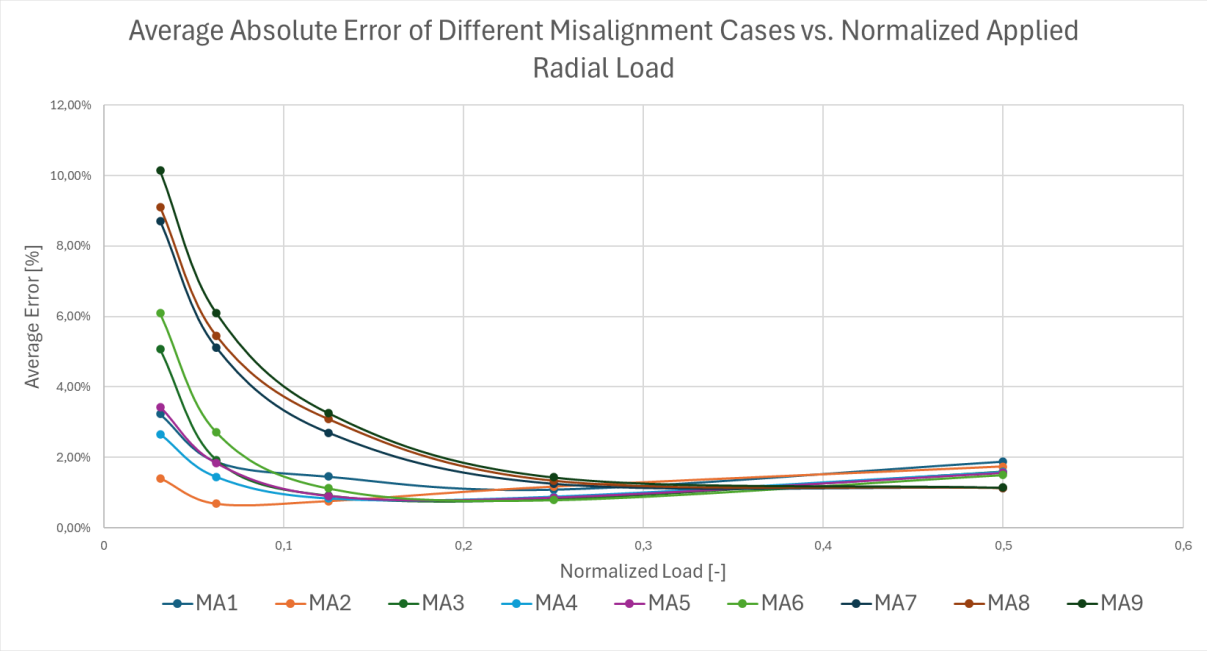

Figure 4.3: Average absolute error of different misalignments vs. applied radial load. Misalignments structured per table 3.1, where MA1 is misalignment case 1.

The figure illustrates the mean error for all misalignments across the eight bearings. The most significant errors are typically observed at lower loads. To calculate the average error, the absolute error value for different loads was summed, and the total was divided by the number of bearings measured. Figure 4.4 below illustrates the mean error for all different bearings across all nine misalignments.

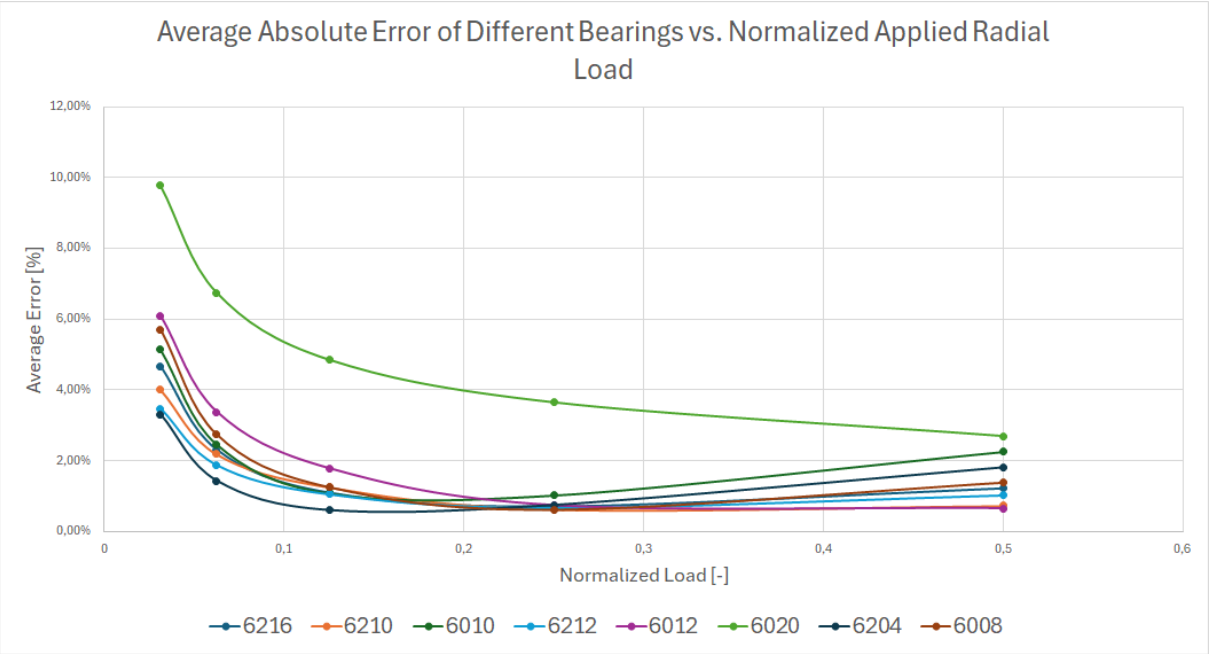

Figure 4.4: Average absolute error of different bearings vs. applied radial load

The fact that the relative error at the lower loads are larger than for the larger loads should be noticed whilst remembering that the numerical difference for the lower loads could be as low as one or two micrometers but the relative error will be much larger for a smaller displacement than a larger one. The result's characteristics from applied axial loads are similar to the radial results. The average error of different misalignment cases versus the normalized applied axial load is presented in figure 4.5.

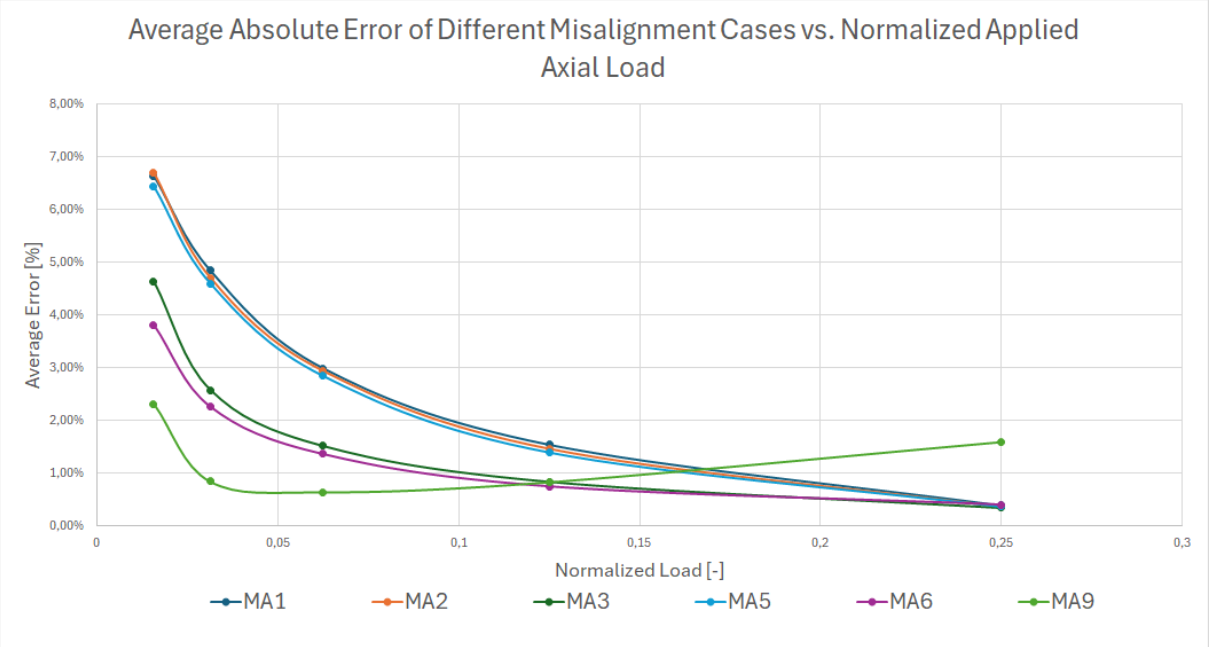

Figure 4.5: Average absolute error of different misalignments (per table 3.1) vs. applied axial load.

The applied axial loads reached 0.25 of the bearings' dynamic load rating, equivalent to half the radial loads. As was the case with radial loads, the relative error generally increases at lower loads. Figure 4.6 below illustrates the mean error for all bearings listed in appendix E across all misalignments per table 3.1. Note that misalignment cases MA4, MA7, and MA8 will result in the same axial displacements as cases MA2, MA3, and MA6 and are therefore not included.

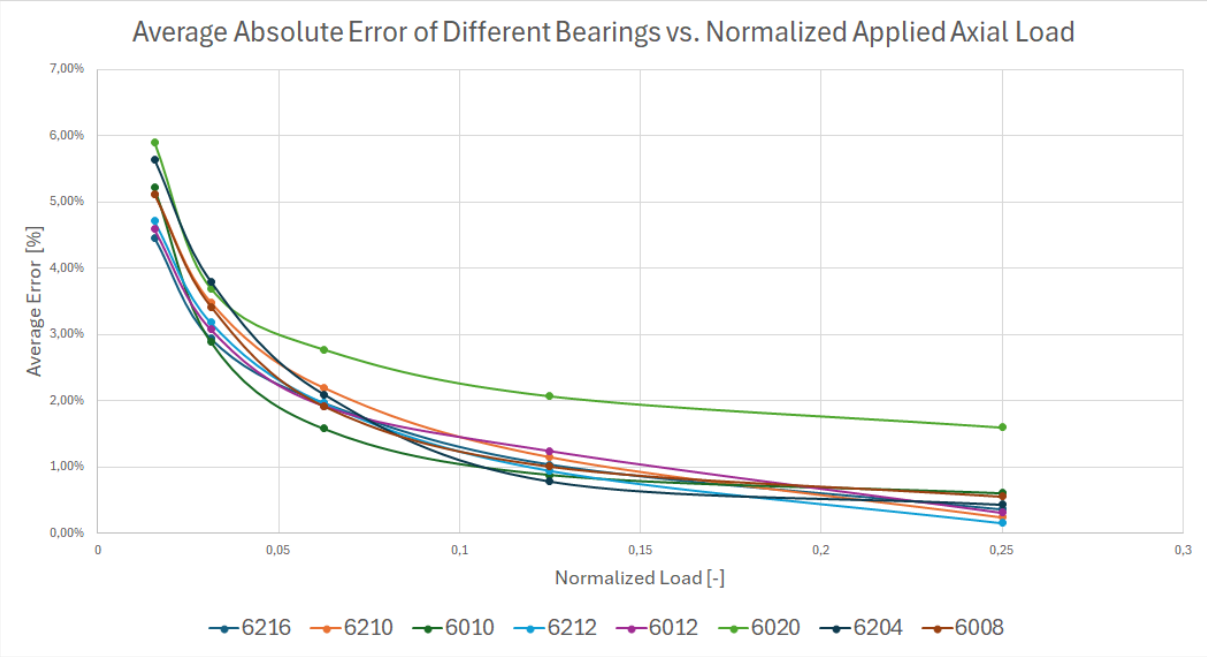

Figure 4.6: Average absolute error of different bearings vs. applied axial load

4.3 Combined Loading Results

This section presents the results from combined load cases. A combined load case refers to the case where both an axial and a radial load are applied simultaneously. For more information on the simulation of combined loading, please refer to section 3.11. In total, there are 21 different sample load cases across all nine misalignments. The two figures below present detailed results and a general overview, respectively.

The detailed data shows the combined displacement results for SKF bearing 6216 in x, y and z direction across all 21 samples. The coordinates are illustrated in figure 4.7 and are listed below:

- **x:** Radial orthogonal direction i.e. the loading direction for radial loads
- **y:** Radial parallel direction
- **z:** Axial direction

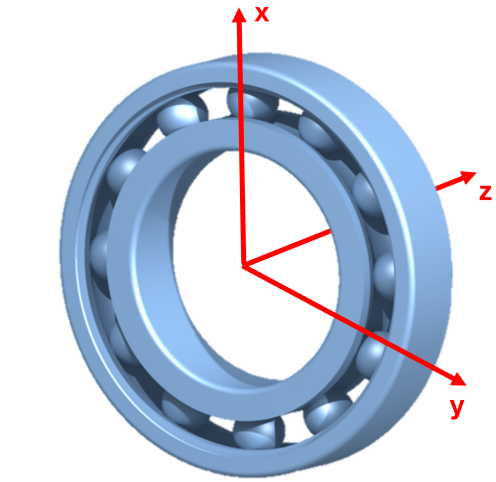

Figure 4.7: Coordinate System

It is clear that load case nr 7 and 12 show excessive errors in z-direction whilst load case nr 8 shows a marginally bigger error in x-direction. See figure 4.8.

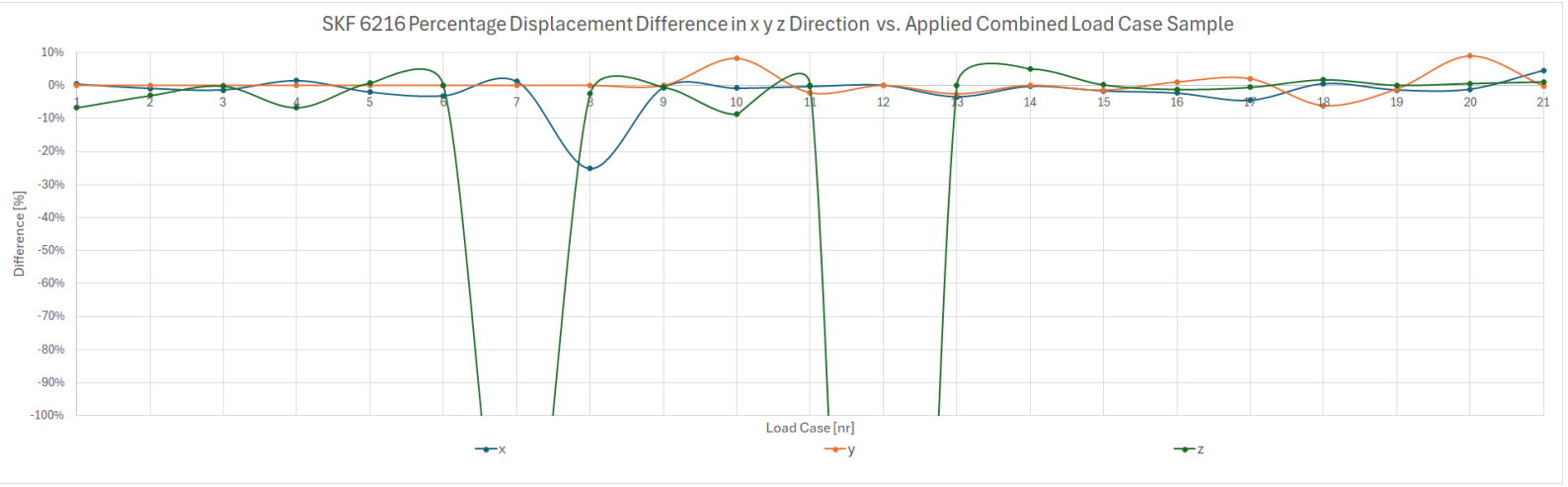

Figure 4.8: SKF 6216 X y z error for each applied load case sample numbered from 1 to 21 per table 3.4 to 3.12.

Additionally, figure 4.9 below provides a more comprehensive overview of all bearings simulated per appendix E. After reviewing the data, it is evident that load cases 7 and 12 demonstrate weaker performance compared to the other load cases across all bearings.

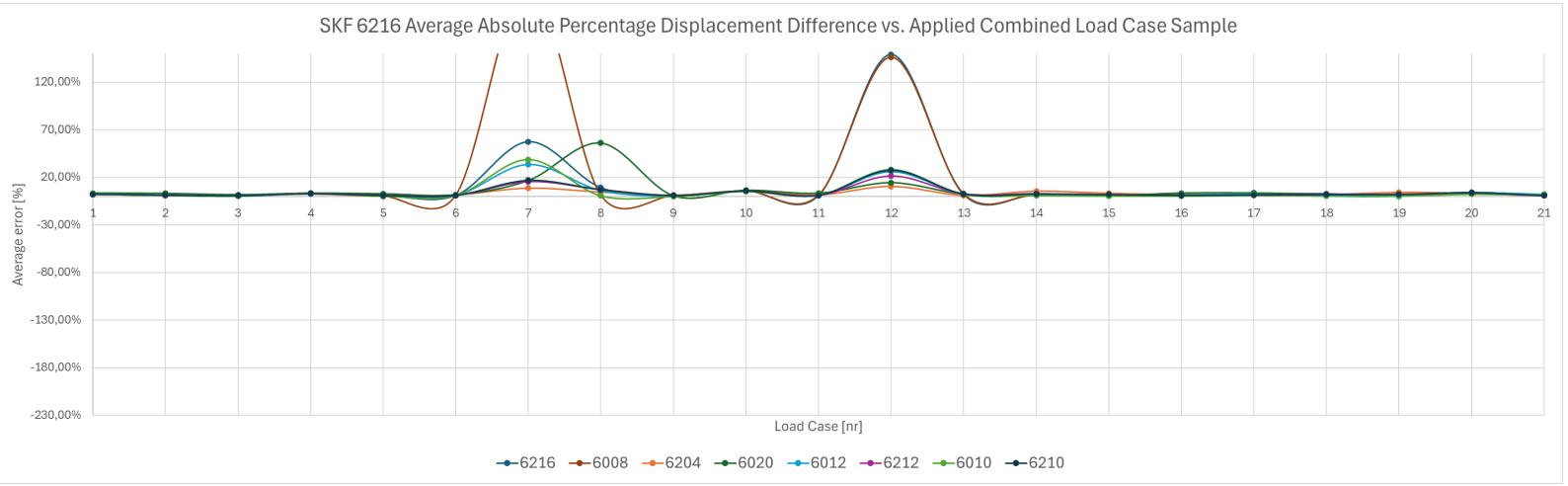

Figure 4.9: SKF 6216 average absolute error for each applied load case sample numbered from 1 to 21 per table 3.4 to 3.12.

Load case 7 and 12 are both cases with high radial load and a lower axial load with the following misalignments:

- Load Case 7: 1 milliradian orthogonal
- Load Case 12: 1 milliradian orthogonal and 1 milliradian parallel

As some displacements are below 1 micrometer, a small displacement error can lead to a large relative error. To address this issue and minimize noise in the visualized results, it was determined to cancel all relative errors with a displacement of less than 1 micrometer. Please refer to table 4.3 for a visual representation of the load cases that have been deleted, highlighted by cell borders.

Table 4.3: Combined load results of SKF 6212

SABR Results [μm]			Abaqus Results [μm]			Difference [%]		
dx	**dy**	**dz**	**dx**	**dy**	**dz**	**dx**	**dy**	**dz**
6.09	0	153.99	6.097436	-0.00000004	143.9678	0.12%	0.00%	-6.51%
17.76	0	204.19	17.56172	-0.00000002	198.5852	-1.12%	0.00%	-2.74%
3.13	0	290.27	3.076737	-0.00000109	290.4563	-1.70%	0.00%	0.06%
103.94	0	22.67	105.2712	-0.00000006	20.8538	1.28%	0.00%	-8.01%
57.53	0	271.14	56.08311	0.00000033	273.8956	-2.52%	0.00%	1.02%
-11.73	0	288.39	-11.3403	-0.00000077	288.5526	-3.32%	0.00%	0.06%
103	0	9.9	104.1864	-0.00000008	5.359059	1.15%	0.00%	-45.87%
9.5	0	59	7.874927	-0.00000003	56.32485	-17.11%	0.00%	-4.53%
-28.17	0	225.1	-27.648	0.00000022	223.2545	-1.85%	0.00%	-0.82%
39.18	-4.3	83.29	39.06033	-4.5652833	74.51222	-0.31%	6.17%	-10.54%
25.53	-14.73	286.02	25.39932	-14.319927	286.3122	-0.51%	-2.78%	0.10%
65.92	-1.57	8.21	66.08927	-1.7421632	2.927735	0.26%	10.97%	-64.34%
-8.48	-14.8	286.37	-8.06344	-14.343746	286.4013	-4.91%	-3.08%	0.01%
65.59	-0.24	-62.73	65.47048	0.22784125	-67.9786	-0.18%	-194.93%	8.37%
-29.09	-14.06	269.38	-28.1559	-13.755761	269.7745	-3.21%	-2.16%	0.15%
8.89	-30.05	190.17	8.785118	-29.884157	186.9227	-1.18%	-0.55%	-1.71%
18.81	-29.21	185.33	18.28481	-29.225818	182.5133	-2.79%	0.05%	-1.52%
100.73	-0.81	-12.65	101.1293	-1.0783956	-13.5273	0.40%	33.14%	6.94%
-7.74	-42.38	274.51	-7.43868	-41.387544	274.7039	-3.89%	-2.34%	0.07%
65.45	0.9	-58.88	61.81049	0.79335598	-60.1267	-5.56%	-11.85%	2.12%
-14.82	-20.97	126.75	-15.085	-20.955781	125.8913	1.79%	-0.07%	-0.68%

The average absolute error across all combined load cases, bearings, and directions listed in table 3.4 to table 3.12 was 7.22%. Important to note that all errors under 1 micrometer is set to zero. With load case 7 and 12 excluded, the average absolute error is 2.48%.

4.4 Ball / Pitch Diameter Ratio vs Stiffness

A point of interest during the course of the project has been to investigate whether or not there is a relation between the ball / pitch diameter ratio and the bearing stiffness. The bearings used in this report have a range of ball / pitch ratios as seen table 4.4. As seen in figure 4.10, no clear relationship was found.

Table 4.4: SKF Bearings with their respective Ball / Pitch Diameter Ratio.

SKF Bearing:	6216	6212	6020	6210	6012	6010	6008	6204
Ball / Pitch Diameter Ratio:	0.156329	0.186765	0.120648	0.181429	0.133148	0.134323	0.147	0.236955

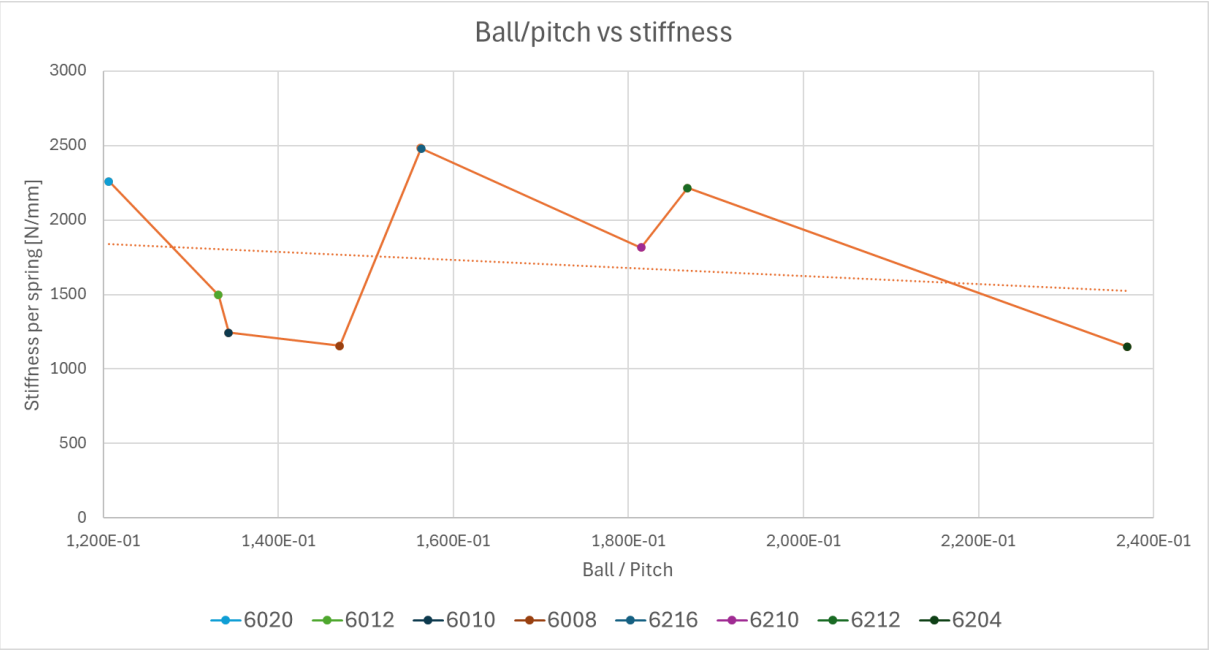

Figure 4.10: Ball/pitch diameter vs individual spring stiffness

4.5 Mesh Convergence Study Results

This section of the results presents the effect of increasing the number of springs per spring set and the number of spring sets per ball on the results. Additionally, the results of the mesh convergence study are presented. This study refined the overall mesh while adhering to the aspect ratio quality criteria.

4.5.1 Results of Increasing the Number of Springs per Spring Set

The primary objective of this study was to ascertain the number of springs per spring set at which the results begin to converge. To accomplish this objective, a simulation was executed in which a radial force was applied in increments for three different bearings that exhibited a wide range of geometric characteristics. This process was repeated for an increasing number of springs. The mean error was calculated and plotted against the number of springs for the bearings 6216, 6204, and 6020, see figure 4.11.

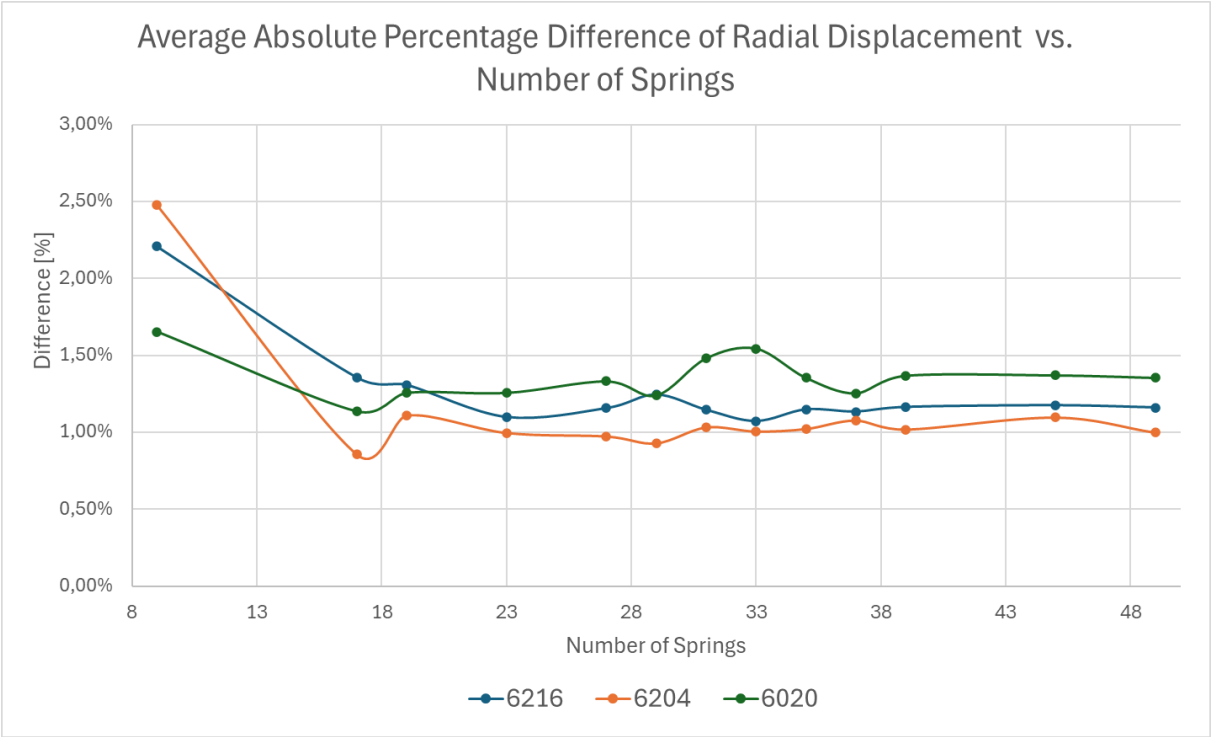

Figure 4.11: Visualization of the effect of increasing the amount of springs per spring set for three different bearings

As illustrated in the figure, the mean error is below 2.5% for all number of springs and the curves are fairly smooth. The only outlier is the first model, which has nine springs per spring set, and the slight bump for bearing 6020 at 31 and 33 springs. However, the relative difference between the results from 17 springs and forward is negligible, and thus, they are considered converged. In addition to validating the accuracy of the results with an increased number of springs per spring set, the effect on simulation time and stability was also noted, see figure 4.12.

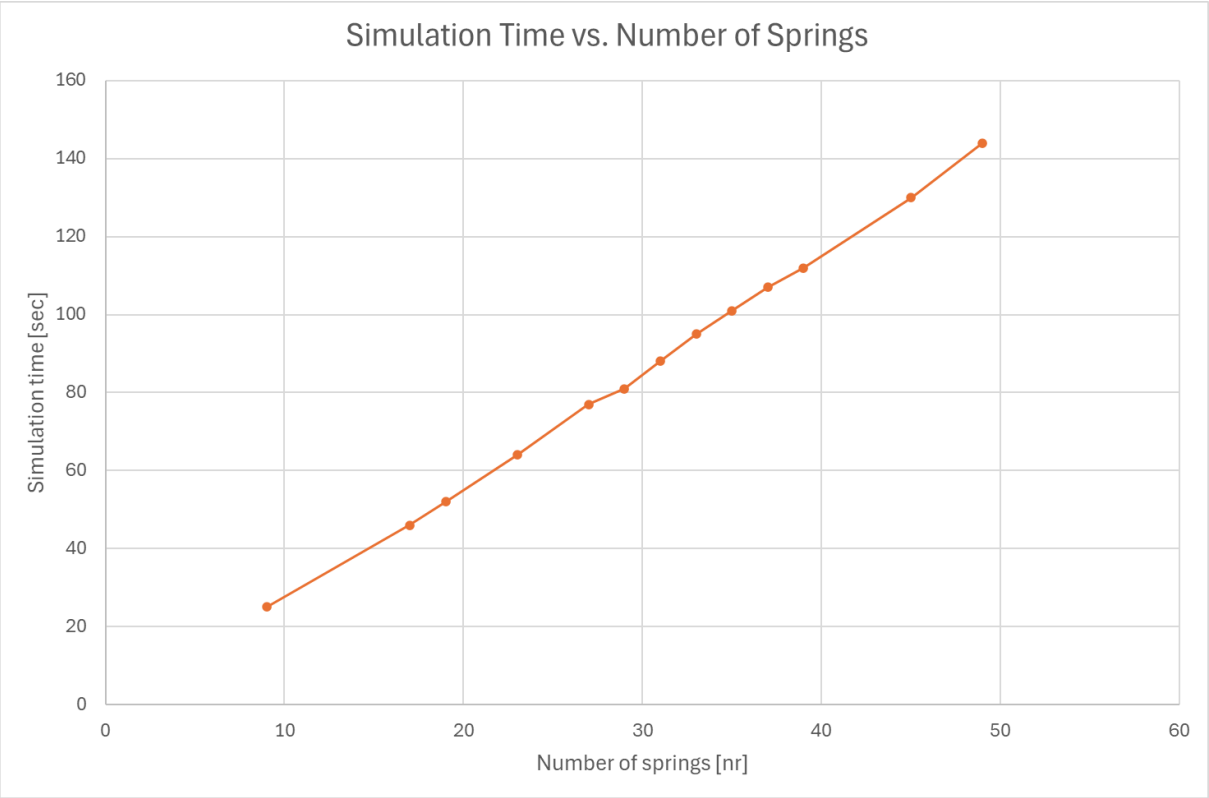

Figure 4.12: Visualization of the effect on simulation time vs. number of springs for simulations run on bearing 6216.

As anticipated, the duration of the simulation increased in proportion to the number of springs i.e. in proportion to increased amount of elements. During the course of these tests, the number of springs per spring set was the only setting that was changed. This resulted in an increase in the aspect ratio as described in section 3.10.1. The increase in aspect ratio was plotted against the number of springs, see figure 4.13.

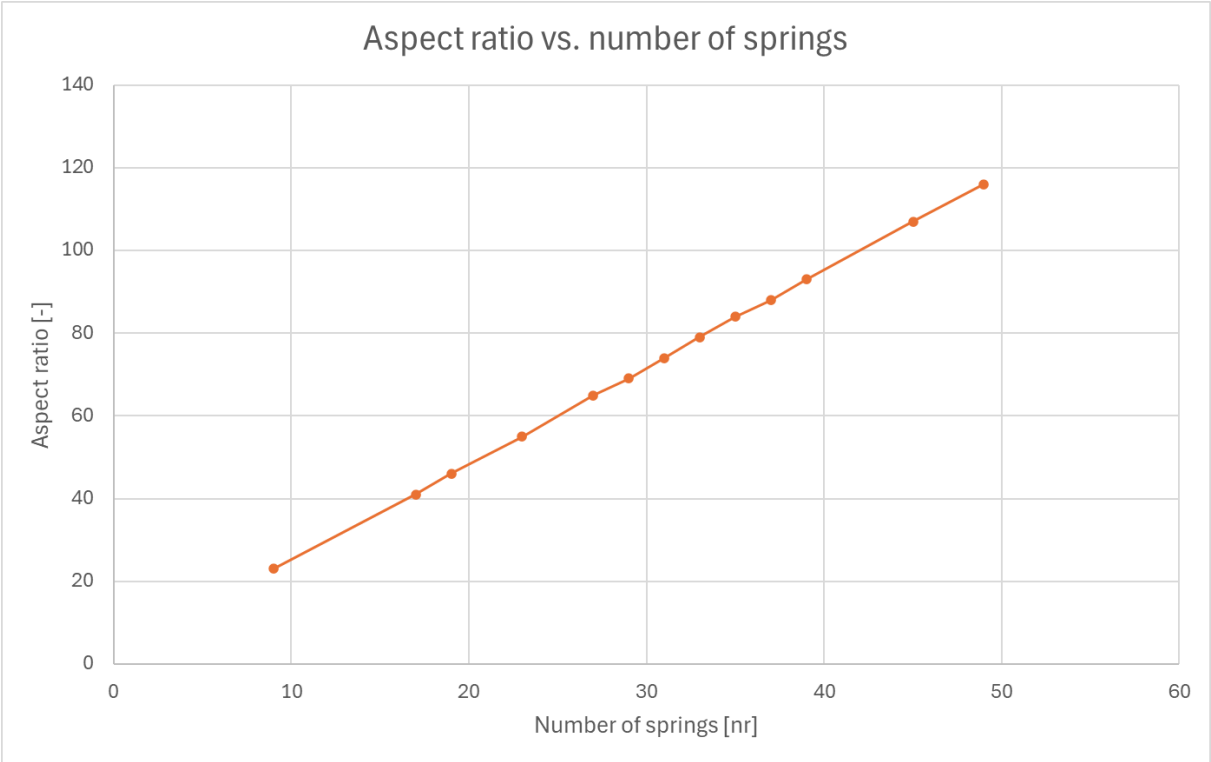

Figure 4.13: Aspect ratio vs. number of springs

Despite achieving aspect ratios exceeding 100, the simulations proceeded without encountering any stability and convergence issues.

4.5.2 Results of increasing the number of spring sets per ball

Section 3.10.2 details the impact of increasing the number of spring sets per ball on the circumferential distribution of stiffness along the rings. It explains that the addition of spring sets per ball leads to a reduction in overall stiffness, with each spring set being weaker to account for the increased number of springs. The same radial load simulation as was run in the previous section was executed again to test the effect of increasing the number of spring sets per ball on the displacements. The model featured 17 springs per spring set, with the number of spring sets per ball increasing incrementally, see figure 4.14.

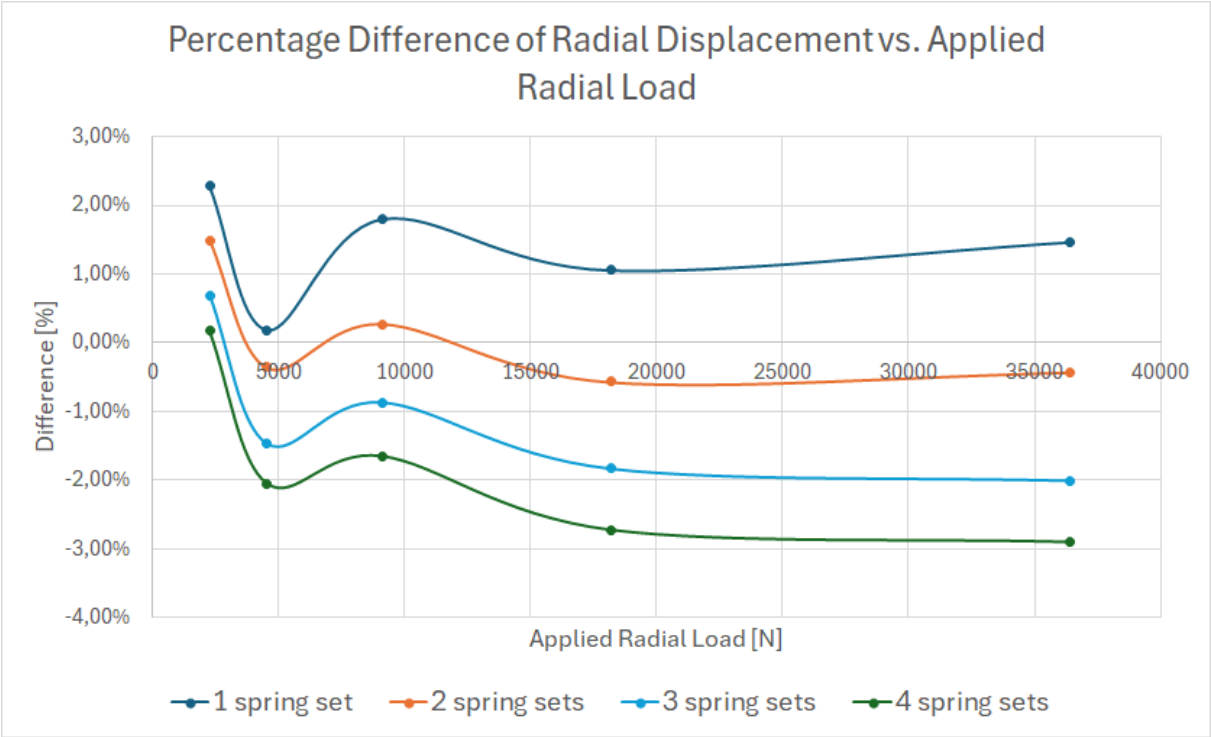

Figure 4.14: Percentage difference of radial displacement vs. applied radial load over five load cases. Run with bearing 6216 with four different number of spring sets per ball, 17 springs per spring set and two elements radially.

As demonstrated by the figure, the displacements decreased with each increment, indicating an increase in the model's stiffness. This even though the total stiffness of each ball is divided by the number of spring sets per ball, as outlined in section 3.10.2. Another point made in section 3.10.2 is the possible advantages to numerical stability and the aspect ratio when increasing the amount of spring sets per ball. Figure 4.15 shows how the aspect ratio decreases with increased amount of spring sets per ball.

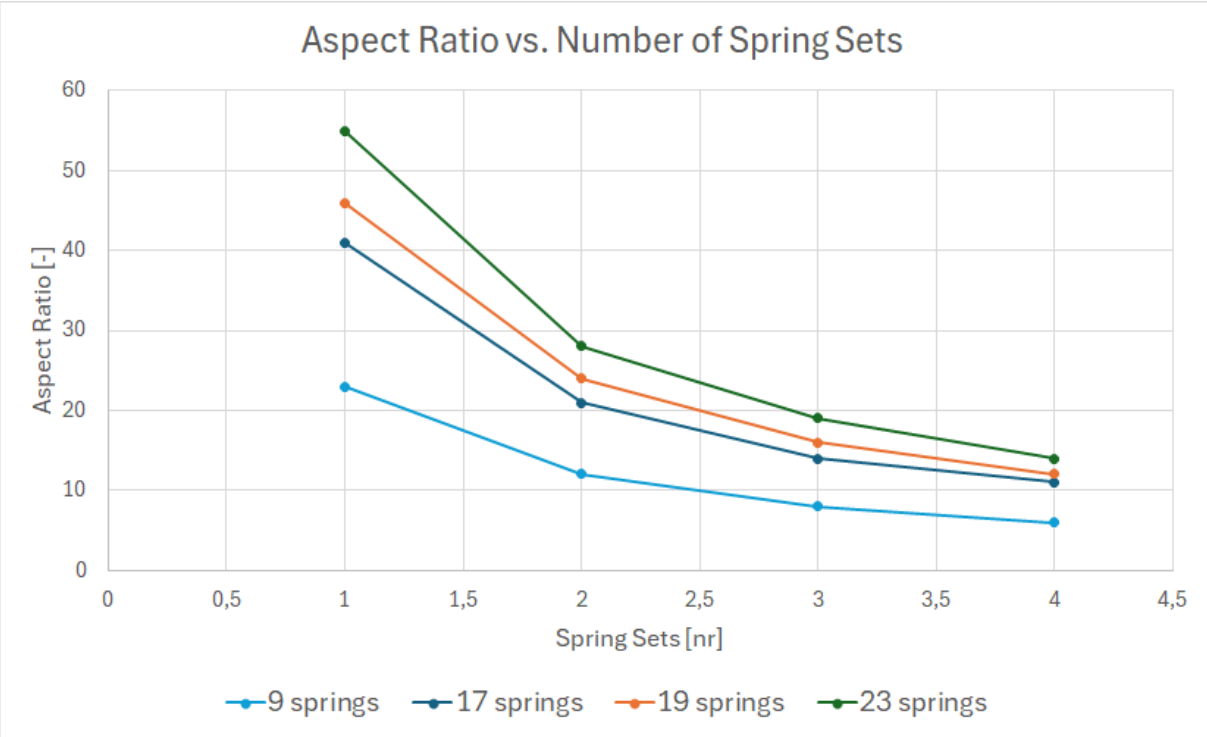

Figure 4.15: Aspect ratio vs. number of spring sets per ball for four different number of springs per spring set. SKF bearing 6216.

As was the case with the increase in the number of springs per spring set and the increase in the aspect ratio, which had no clear negative effect on the stability and convergence of the simulations, the increase in the number of spring sets per ball and the decrease in the aspect ratio had no clear positive effect on the stability nor the convergence of the simulations. However, it should be noted that the simulation time increased, as illustrated in figure 4.16.

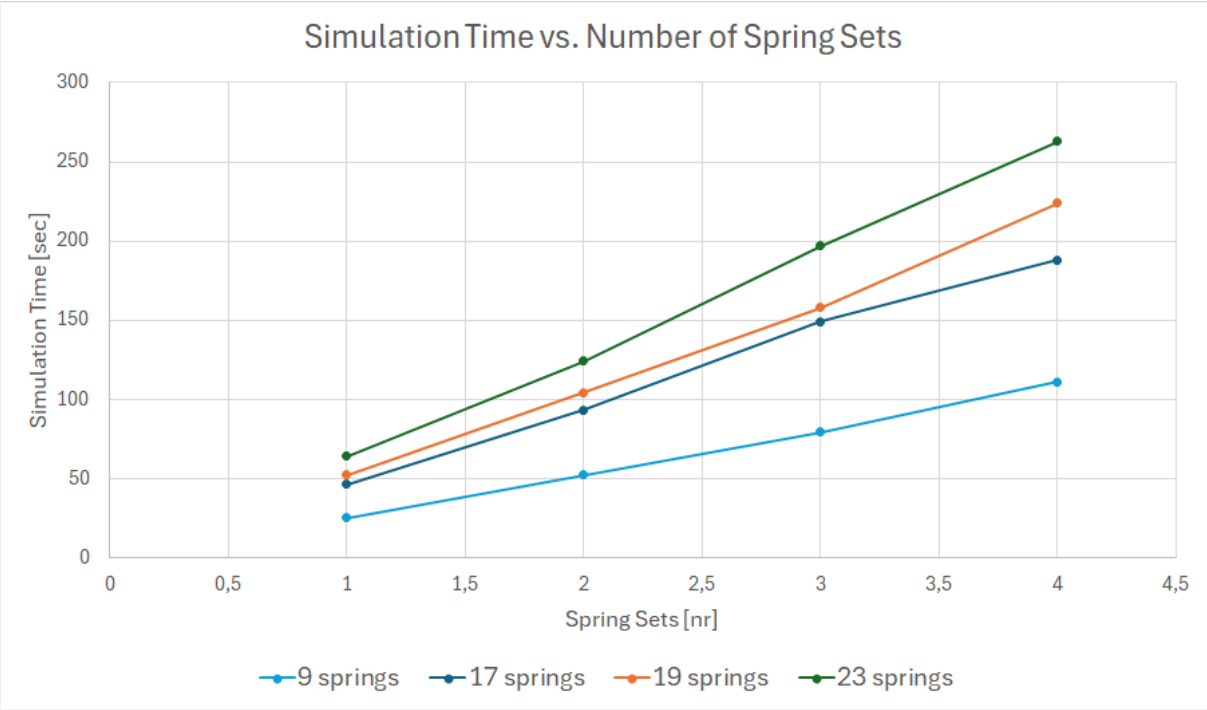

Figure 4.16: Simulation time vs. number of spring sets per ball for four different number of springs per spring set, run on bearing 6216.

4.5.3 Mesh convergence study

The results of changing the number of springs per spring set and the number of spring sets per ball have been evaluated and presented separately. This section details the mesh convergence study, in which both parameters were modified concurrently, while also adjusting the number of elements radially. No alterations were made to the number of elements axially in the flanges, as they already had an aspect ratio much lower than the elements in the raceways.

Firstly, the study focused exclusively on the increase in radial elements. The objective was to assess the response of the aspect ratio to this change, since it was expected to decrease but instead increased, as stated in section 3.10.1. Please refer to figure 4.17 for a visual representation of the results.

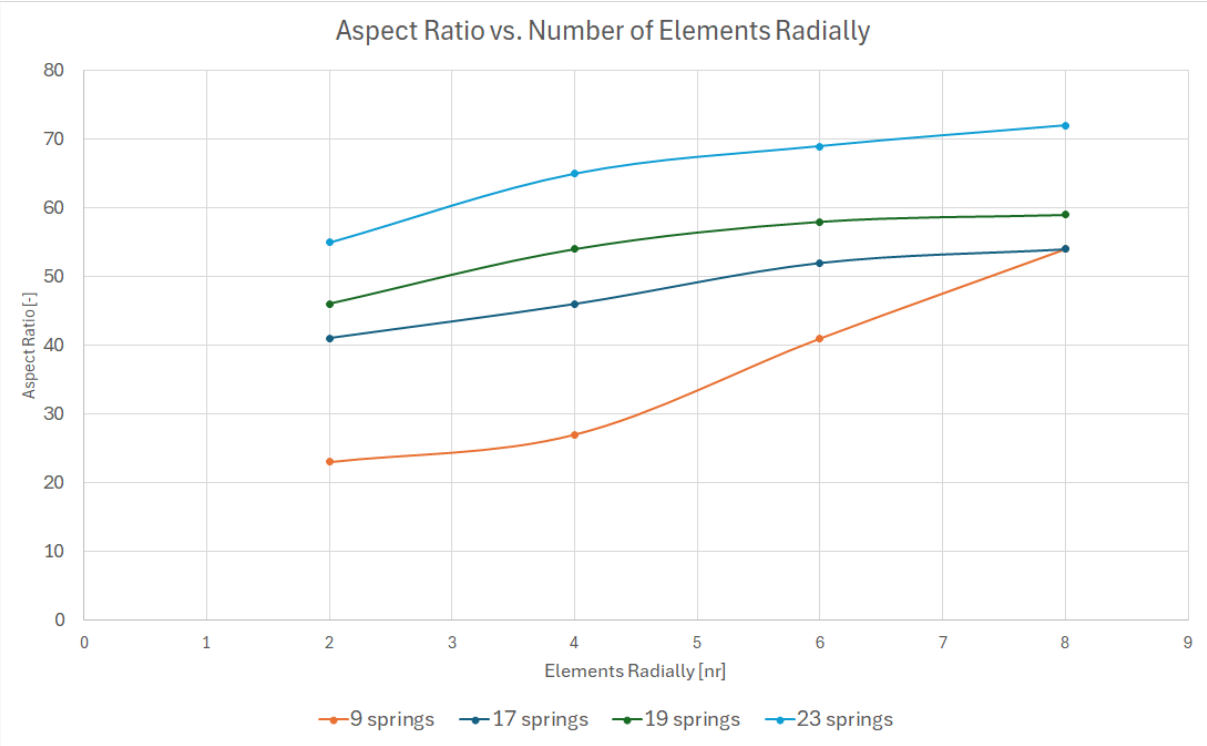

Figure 4.17: Aspect ratio vs. number of elements radially for four different number of springs per spring set, run on bearing 6216.

The figure again show the unexpected results of the aspect ratio increasing with increasing amount of elements radially. An explanation to this behavior is presented in section 5.3.1 in the discussion chapter.

The displacements for the same simulation as has been run previously was also noted and plotted, see figure 4.18.

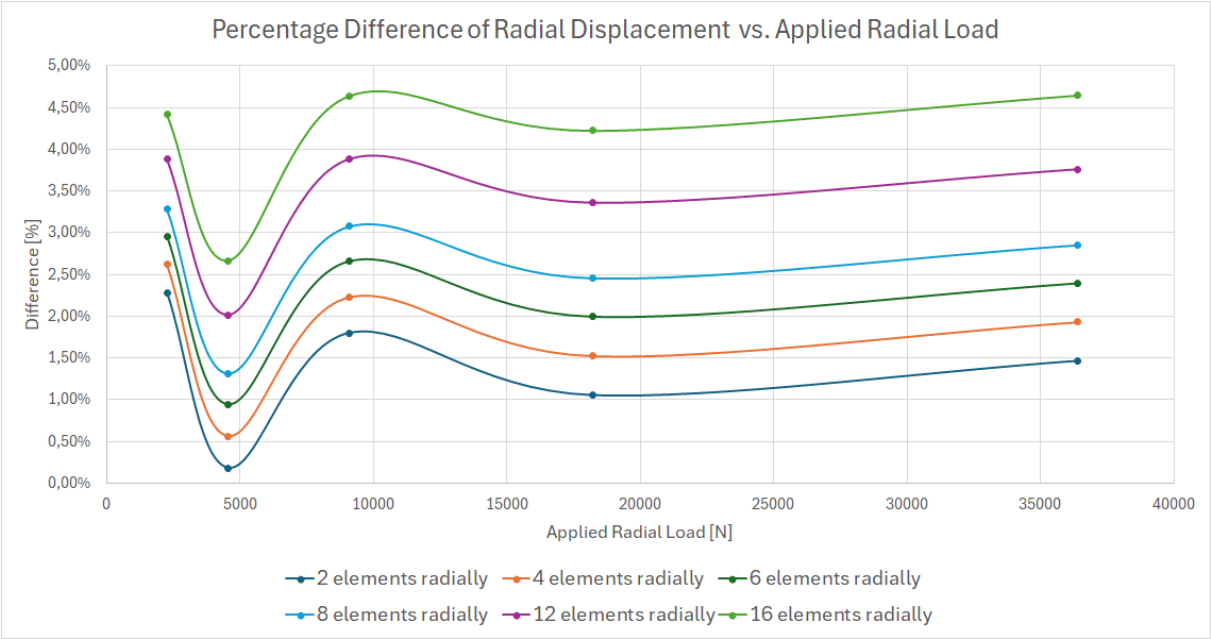

Figure 4.18: Percentage difference of radial displacement vs. applied radial load over five load cases. Run with bearing 6216 with six different number of elements radially, 17 springs per spring set and one spring set.

The figure shows an increase in displacement with each radial element increment suggesting that the model becomes less stiff with increased amount of elements radially.

Discussion

This discussion aims to analyze the results, investigate potential sources of error and reflect on the aspects that were successful. Furthermore, it will lay the foundation for the conclusions and outline directions for future work in chapter 6 and chapter 7, respectively.

5.1 Bearing Model Geometry

The results of the bearing geometry verification presented in 4.1 concluded a partial geometry verification. This was due to the fact that although the Lincoln geometry is correct and have been verified using CAD tools, the Abaqus raceway simulation check does not yield results that align with SABR results. As the loads in the raceway geometry simulation are very small, the margin of error is tiny compared to other load cases of radial, axial and combined loads. It can be concluded that the root cause must be related to the initial contact condition between the springs representing the balls and its raceways. As we have verified that the raceway geometry itself is correct, the error could be connected to the springs initial stiffness. The MetaPost measurements presented in 4.2 show that the Abaqus model is stiffer than the reference data, indicating the the springs initial stiffness is too high. On the other hand, the results from low radial and axial load cases shows good accuracy with an average error of 0.7208 and 5.8624 micrometers, respectively. See table 5.1. However, it is evident that the error in axial direction is larger than in radial direction. It could indicate that there is some kind of discrepancy with the bearing geometries.

Table 5.1: The average absolute error of the lowest radial and axial load case across all bearings. All individual errors are listed as well.

SKF Bearing	6216	6008	6204	6020	6012	6212	6010	6210
Absolute radial error [μm]:	0.864	0.541	0.378	1.534	0.716	0.631	0.509	0.594
Absolute axial error [μm]:	6.858	3.682	4.444	6.750	4.220	6.750	3.947	5.862
							Average absolute radial error [μm]:	0.721
							Average absolute axial error [μm]:	5.314
							Average absolute error [μm]:	**3.017**

Another possible source of error could be the methods used to implement the geometry verification. The methods used in SABR and Abaqus did differ from each other. The axial load was implemented incrementally along with a 50 N radial load in SABR. In contrast, in Abaqus, the axial displacement was imposed incrementally, while the radial load of 50 N was applied as a force allowing the bearing to follow the raceway profile.

5.2 Analytical Solutions

Based on the failed attempts to model ball bearings using analytical relationships, it can be questioned whether or not the analytical solutions of Harris (2001) and Hamrock (1983) are suitable for ball bearing modeling. As discussed in Fang et al. (2014) and Sun and Hao (2012), Hertz theory may not work as well for conformal contact conditions as previously assumed.

5.3 Mesh Study Discussion

The purpose of this section of the discussion is to provide possible explanations for questions that might arise based of the results from the mesh studies.

5.3.1 Aspect Ratio Discussion

Two aspects of the aspect ratios proved to be of particular significance during the course of the project. First, the simulations were executed without any evident issues, even when dealing with highly elongated and stretched elements, i.e., high aspect ratios. Second, the aspect ratio did not decrease despite the introduction of additional radial elements.

The absence of any noted issues with high aspect ratios may be due to the lack of research conducted on the potential risks associated with such ratios, particularly concerning stresses and strains. Please refer to section 3.10.1 for more information on this subject. It is encouraging that the model is sufficiently stable to operate even with suboptimal shaped elements. To assess the model's accuracy with different meshes, a subsequent mesh convergence study is necessary. This study should prioritize the impact on stresses and strains over deformation.

The results indicated a slight increase in aspect ratio with an increase in the amount of elements radially. This was unexpected, but the investigation of how Abaqus calculates the aspect ratio provided a clear explanation. Abaqus will calculate the aspect ratio for 2D and 3D elements using the same method. This involves dividing the length of the longest edge by the length of the shortest edge (Dassault Systemes, 2024d). In the majority of cases, the longest edge will be oriented in the circumferential direction, which is referred to as the "depth." The shortest edge will correspond to the "width," as illustrated in figure 5.1.

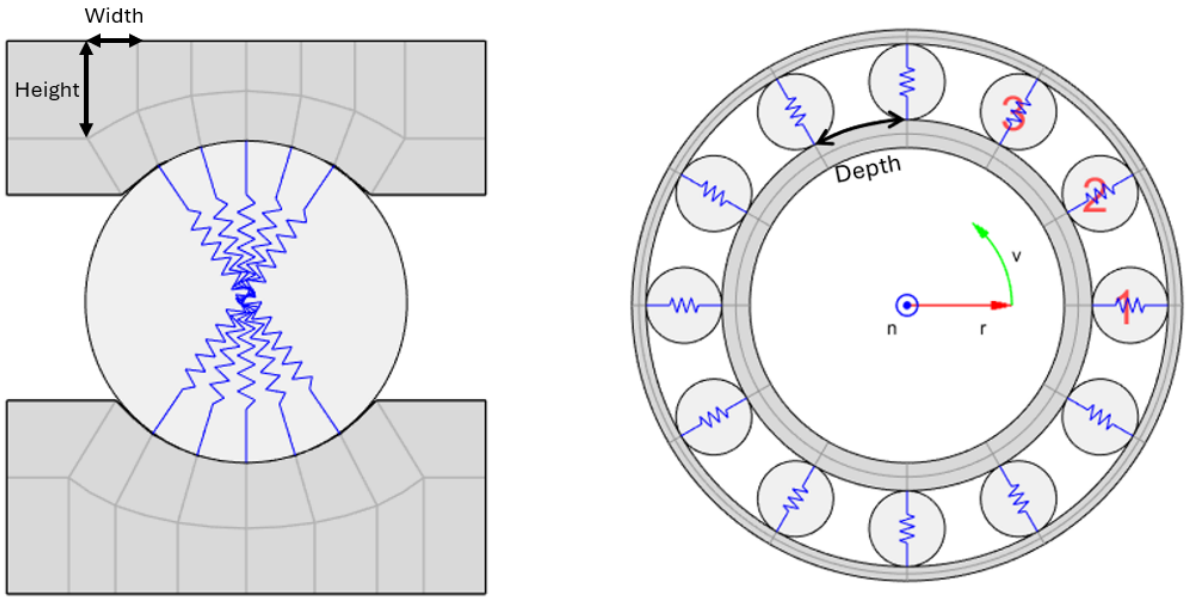

Figure 5.1: Visualization of the width, height, and depth of an element

Provided that the width is smaller than the height, the aspect ratio will not change

when the height changes. If the height is divided so that it is smaller than the width, the aspect ratio neither increase nor decrease. The only reasonable way to decrease the aspect ratio is to decrease the depth of the elements, i.e., increase the number of elements circumferentially, see figure 5.2.

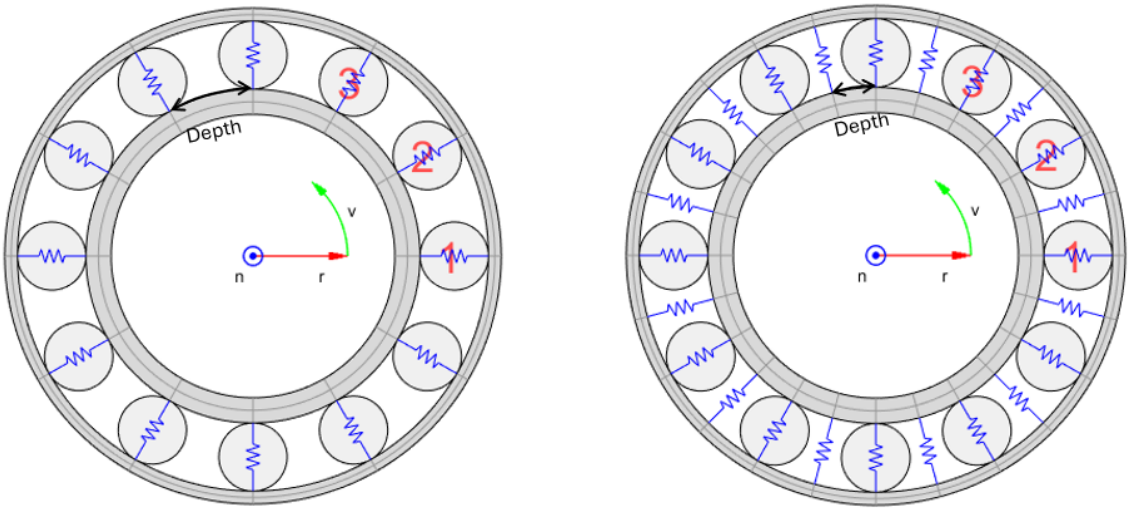

Figure 5.2: Visualization of the depth of an element with one spring set vs. two spring sets per ball

Abaqus's calculation of the aspect ratio is the foundation of this analysis. If an alternative method had been employed, one that considered all three lengths, the outcome would have differed. It is still believed that increasing the number of radial elements could enhance the mesh quality.

5.3.2 Stiffness Changes with Changed Geometry

As demonstrated in section 4.5.2 and 4.5.3, increasing the number of spring sets per ball and elements radially results in similar curves, with values that could be almost identical with a slight scaling factor, see figure 5.3.

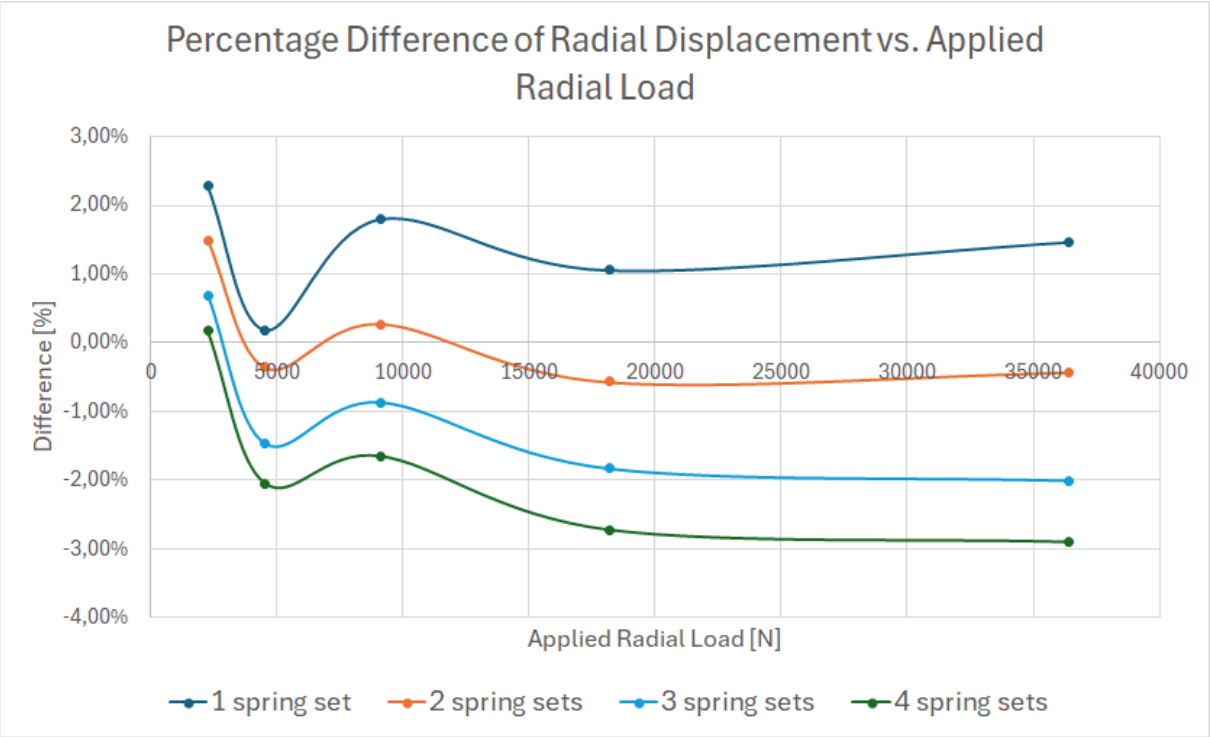

(a) Percentage difference of radial displacement vs. applied load with varying number of spring sets per ball. Elements radially set to 2.

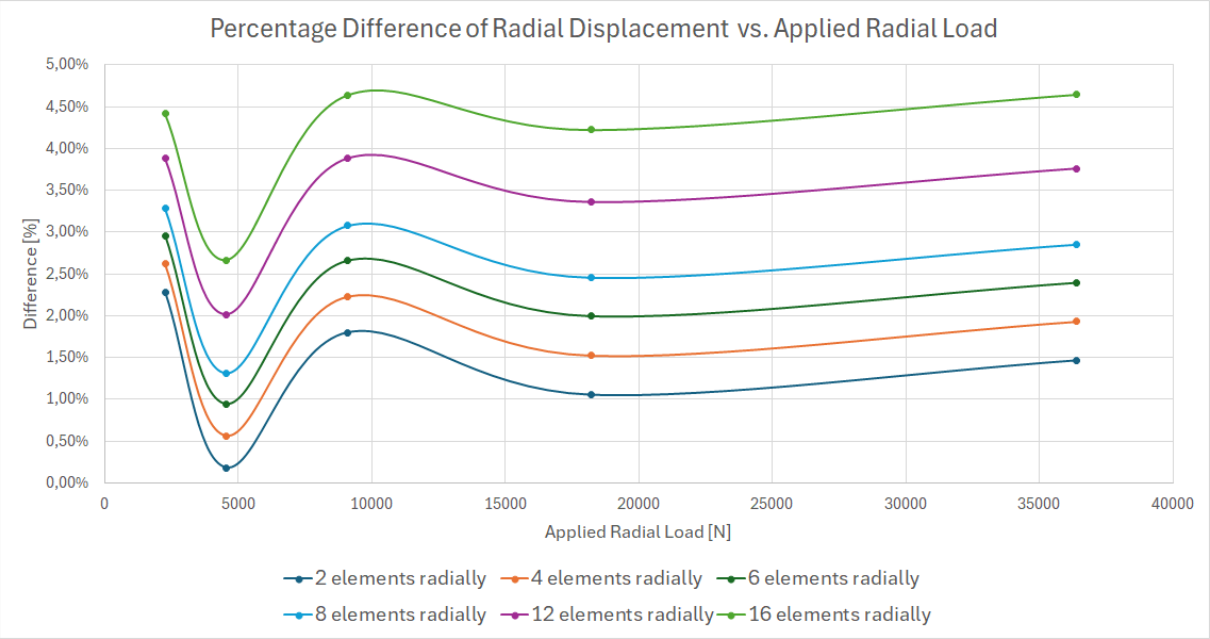

(b) Percentage difference of radial displacement vs. applied load with varying number of elements radially. 1 spring set for all cases.

Figure 5.3: Displacement comparison when varying the number of spring sets per ball and the number of elements radially

As the elements increased radially, the displacements, i.e. the positive error, increased, see figure 5.3(b). This could be due to the fact that smaller elements and finer grids will generally lead to larger displacements in finite element analysis (FEA), (Fidelis FEA,

n.d.) & (SDC Verifier, n.d.). The results showed an opposite behavior when the number of spring sets per ball was increased, see figure 5.3(a). This indicates that dividing the spring stiffness by the number of spring sets per ball does not decrease the value enough to counteract the added stiffness of the new sets. However, as the results demonstrate similar behavior, it suggests that it may be possible to achieve matching results if a correct scaling factor is identified.

The different behavior of refining the mesh in different directions meant that a proper mesh convergence study was not considered feasible, at least at this stage and with the time remaining. In addition, the number of elements increases quite rapidly with each refinement, so that simulations required an excessive amount of computing time and in many cases did not run at all.

Looking at figure 5.3(a), it's clear that the best results were obtained using two sets of springs, at least for bearing 6216. To see if this was the case for other bearings, the same test was run for bearings 6204 and 6020, see figure 5.4.

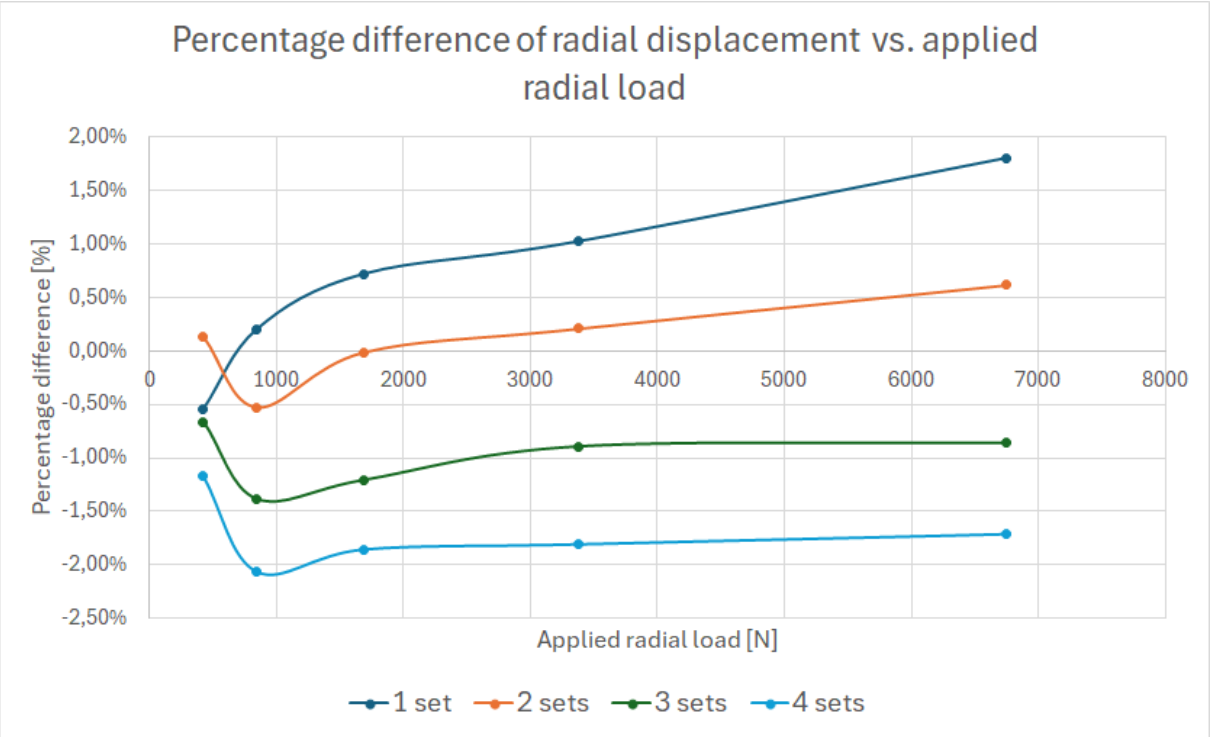

(a) Percentage difference of radial displacement vs. applied load with varying number of spring sets per ball, run on bearing 6204

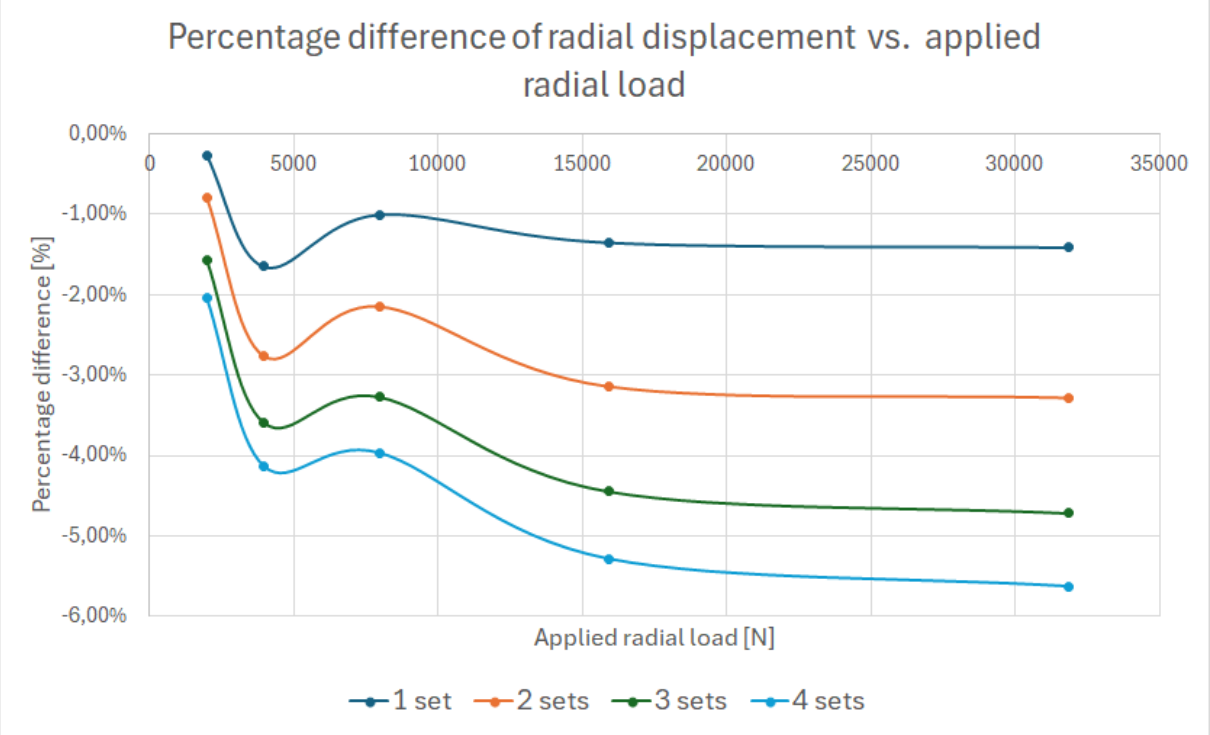

(b) Percentage difference of radial displacement vs. applied load with varying number of spring sets per ball, run on bearing 6020

Figure 5.4: Displacement comparison when varying the number of spring sets per ball for two different bearings

Figure 5.4(a) shows that the displacements of bearing 6204 start to show a similar behavior

with two or more spring sets per ball, with the best results still being for two sets. Figure 5.4(b) however shows that the best results for bearing 6020 were achieved with only one set of springs, but here it should be noted that the curve fitted equation could not reach the desired stiffness of bearing 6020, so this explains the different behavior, see section 3.9. All three figures show the same behavior of increasing stiffness with additional spring sets per ball. The fact that they all behave the same is positive, and it also means that there may be a way to manipulate the curve fit equation by increasing or decreasing the number of spring sets per ball or by adjusting the stiffness depending on the number of spring sets per ball to get an even better fit.

Conclusions

Overall, the results are considered satisfactory as the model is stable throughout all misalignments and yields relatively accurate results. As listed in section 4.3, the average absolute error across all combined load cases listed in table 3.4 to table 3.12 was 7.22% (2.48% with load case 7 and 12 excluded). It is however, too early to state whether or not the model derived in this thesis is general enough to work in the applications it is meant for in the Volvo GTT team. SKF bearing 6020 had a significant impact on the curve-fit results, it affected the overall results negatively when it was included in the curve-fit. The bearing was therefore excluded from the curve fit procedure. As a consequence, the results of bearing 6020 itself show significantly less precise results, see figure 4.4. Further analysis of its distinct properties and other bearings with similar properties could assist in drawing any conclusions on why it does not align with the bearings listed in appendix E.

If the team at Volvo GTT would use the current version of Lincoln, it is reasonable to conclude that, for the cases that have been tested i.e., the bearings listed in appendix E, the optimal settings are 2 elements radially, 2 spring sets per ball for all bearings except 6020, which should only utilize one spring set per ball, and 17 to 29 springs per spring set. This will ensure precise results without compromising the simulation's stability. The most significant challenges are related to simulations involving lower loads, particularly in instances of misalignment. Additionally, there are considerations for bearings that have not been addressed in this thesis, i.e., bearings not included in appendix E.

The questions stated in section 1.4 are answered in the following paragraph. First, it can be concluded that it is possible to accurately model deep groove ball bearings using a set of non-linear springs. The current results are a good first step towards trustworthy results and indicate that future work along the same path can yield a model ready for implementation. Second, the thesis has investigated both radial, axial, and combined loads across all nine misalignments. As there has been some issues with the bearing geometry verification and the axial displacements, the results can deviate in certain cases. On the other hand, the model is stable across all cases and can easily be updated with new parameters in future updates. Last, more results from various types of bearings are needed in order to conclude whether or not the model derived in this project can act as a generalized model. More about this in the future work chapter, see chapter 7.

Future Work

Several aspects of the current work offer opportunities for further development and refinement. One key area is the modeling of stiffness as the number of spring sets per ball increases. In future studies, it will be important to identify an appropriate scaling factor that accurately captures the stiffness behavior as the number of spring elements increases. This will ensure that the model remains both accurate and computationally efficient as complexity increases.

Inconsistencies in the geometric representation within the Abaqus simulations require further investigation. A deeper analysis is needed to understand the source of these inconsistencies and to ensure that the simulation geometry is aligned with the intended design, see section 5.1.

The implementation of angular contact bearings in the Lincoln model is also of interest to Volvo. This addition would allow for a more versatile representation of bearing.

To better understand the mechanical response, future work should also include comprehensive stress and strain analyses. These analyses will help verify that the load distribution in the model behaves as expected and could provide important insight into the structural performance.

Finally, it is important to test the method with a wider range of bearing types to determine its general applicability. If a universal approach proves infeasible, an alternative strategy could be to classify bearings into groups based on their characteristics and apply group-specific stiffness models. This would allow for tailored modeling while maintaining a manageable level of complexity and manual recalibration from the Volvo GTT team.

References

Abaqus. (n.d.). *Abaqus*. Retrieved May 27, 2025, from https://www.3ds.com/products/simulia/abaqus

Brändlein, J., Eschmann, P., Hasbargen, L., & Merkle-Eschmann, U. (1985, January 1). *Ball and roller bearings : Theory, design and application*. https://ci.nii.ac.jp/ncid/BA4086886X

Brewe, D. E., & Hamrock, B. J. Geometry and starvation effects in hydrodynamic lubrication [Work of the U.S. Government. Public use permitted.]. In: In *Meeting of the propulsion and energetics panel symposium on problems in bearings and lubrication*. Work of the U.S. Government. Public use permitted. AGARD. Ottawa, Canada: NASA Lewis Research Center, 1982. https://ntrs.nasa.gov/citations/19820012366

Dassault Systemes. (2024a). *Simulia user assistance 2024: Springs*. Retrieved February 12, 2025, from https://help.3ds.com/2024/english/dssimulia_established/SIMACAEELMRefMap/simaelm-c-spring.htm?contextscope=all&id=91d8fba61b8d45e3b3e9731fcaa3233a

Dassault Systemes. (2024b). *Simulia user assistance 2024: Surface behavior*. Retrieved May 9, 2025, from https://help.3ds.com/2024/english/dssimulia_established/SIMACAEKEYRefMap/simakey-r-surfacebehavior.htm?contextscope=all&id=374eeefee37948d7a0b7ef90faeadcdd

Dassault Systemes. (2024c). *Simulia user assistance 2024: Mpc*. Retrieved May 9, 2025, from https://help.3ds.com/2024/english/dssimulia_established/SIMACAEKEYRefMap/simakey-r-mpc.htm?contextscope=all&id=ccad477ecfd442fa86e3f417656c5f89

Dassault Systemes. (2024d). *Simulia user assistance 2024: Mesh quality control*. Retrieved May 9, 2025, from https://help.3ds.com/2021/english/dssimulia_established/SIMACAECAERefMap/simacae-c-mgnconcpartitionverify.htm?contextscope=all&id=29cb65d71fa44fa4bf5d6d443b4dea29

Fang, X., Zhang, C., Chen, X., Wang, Y., & Tan, Y. (2014). A new universal approximate model for conformal contact and non-conformal contact of spherical surfaces. *Acta Mechanica*, *226*(6), 1657–1672. https://doi.org/10.1007/s00707-014-1277-z

Fidelis FEA. (n.d.). *Element size in fea: Does it matter?* Retrieved May 12, 2025, from https://www.fidelisfea.com/post/element-size-in-fea-does-it-matter

Hamrock, B. J., & Anderson, W. J. (1973). Analysis of an arched outer-race ball bearing considering centrifugal forces. *ASME Journal of Lubrication Technology*, *95*, 265–276.

Hamrock, B. J. (1983, January 1). *Rolling-element bearings*.

Harris, T. A. (2001, January 1). *Rolling bearing analysis* (4th ed.). John Wiley & Sons, Inc.

Hertz, H. (1881). The contact of elastic solids. *J. Reine Angew. Math.*, *92*, 156–171. https://www.researchgate.net/profile/Zhaoyang-Zhao-2/post/How_to_derivate_the_equations_in_Hertzs_paper_1881_ON_THE_CONTACT_OF_ELASTIC_SOLIDS/attachment/630989fedf58b43f60655297/AS%3A1143128108117940 6%401661569534229/download/1881_ON+THE+CONTACT+OF_ELASTIC_SOLIDS.pdf

Jones, A. B. (1946). *New departure engineering data: Analysis of stresses and deflections*. New Departure, Division General Motors Corp.

Matlab. (n.d.). *Matlab*. Retrieved May 27, 2025, from https://se.mathworks.com/products/matlab.html

NE Nationalencyklopedin AB. (n.d.). *Kontakttryck*. Retrieved March 18, 2025, from https://www-ne-se.eu1.proxy.openathens.net/uppslagsverk/encyklopedi/l%C3%A5ng/kontakttryck

Rahani, R. (2021). *An investigation of finite element models of roller bearings*. Chalmers University of Technology.

Realis Simulation. (2025). *Sabr - realis simulation* [Accessed May 2, 2025]. https://www.realis-simulation.com/products/sabr/sabr-bearing-analysis/

SABR. (n.d.). *Sabr*. Retrieved May 27, 2025, from https://www.realis-simulation.com/products/sabr/

SDC Verifier. (n.d.). *The fundamentals of mesh quality in fea*. Retrieved May 12, 2025, from https://sdcverifier.com/structural-engineering-101/the-fundamentals-of-mesh-quality/

Sun, Z., & Hao, C. (2012). Conformal contact problems of ball-socket and ball. *Physics Procedia*, *25*, 209–214. https://doi.org/10.1016/j.phpro.2012.03.073

Appendix

Some appendices may be published as blank due to the NDA agreement between Volvo GTT and the authors of this thesis.

8.1 Appendix A

Dimensionless Contact Parameters from Harris (2001, p.196).

Table 8.1: Dimensionless Contact Parameters

F(p)	**a***	**b***	δ*
0	1	1	1
0.1075	1.0760	0.9318	0.9974
0.3204	1.2623	0.8114	0.9761
0.4795	1.4556	0.7278	0.9429
0.5916	1.6440	0.6687	0.9077
0.6716	1.8258	0.6245	0.8733
0.7332	2.011	0.5881	0.8394
0.7948	2.265	0.5480	0.7961
0.83495	2.494	0.5186	0.7602
0.87366	2.800	0.4863	0.7169
0.90999	3.233	0.4499	0.6636
0.93657	3.738	0.4166	0.6112
0.95738	4.395	0.3830	0.5551
0.97290	5.267	0.3490	0.4960
0.983797	6.448	0.3150	0.4352
0.990902	8.062	0.2814	0.3745
0.995112	10.222	0.2497	0.3176
0.997300	12.789	0.2232	0.2705
0.9981847	14.839	0.2072	0.2427
0.9989156	17.974	0.18822	0.2106
0.9994785	23.55	0.16442	0.17167
0.9998527	37.38	0.13050	0.11995
1	∞	0	0

8.2 Appendix B

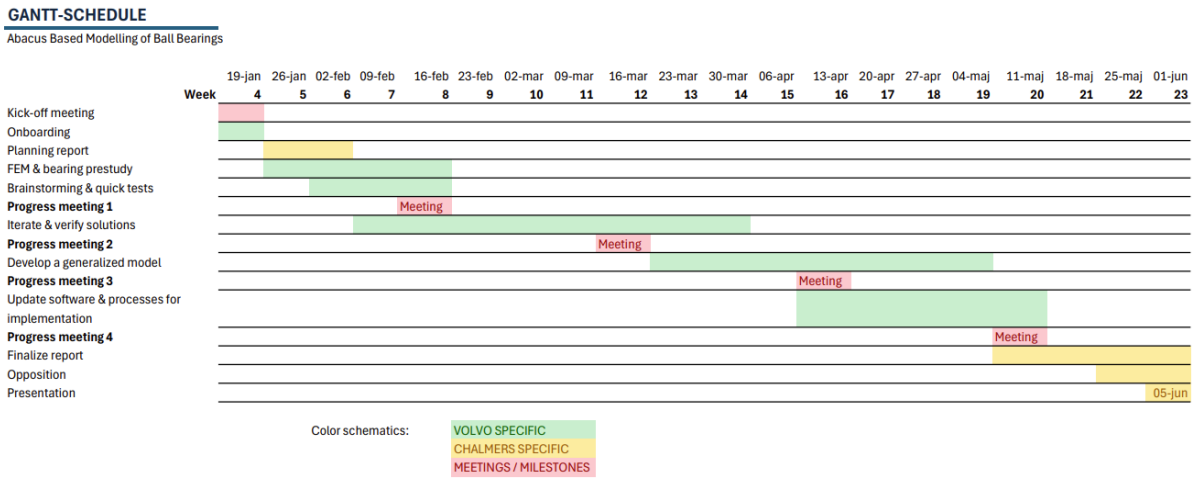

Figure 8.1: Gantt-chart

8.3 Appendix C

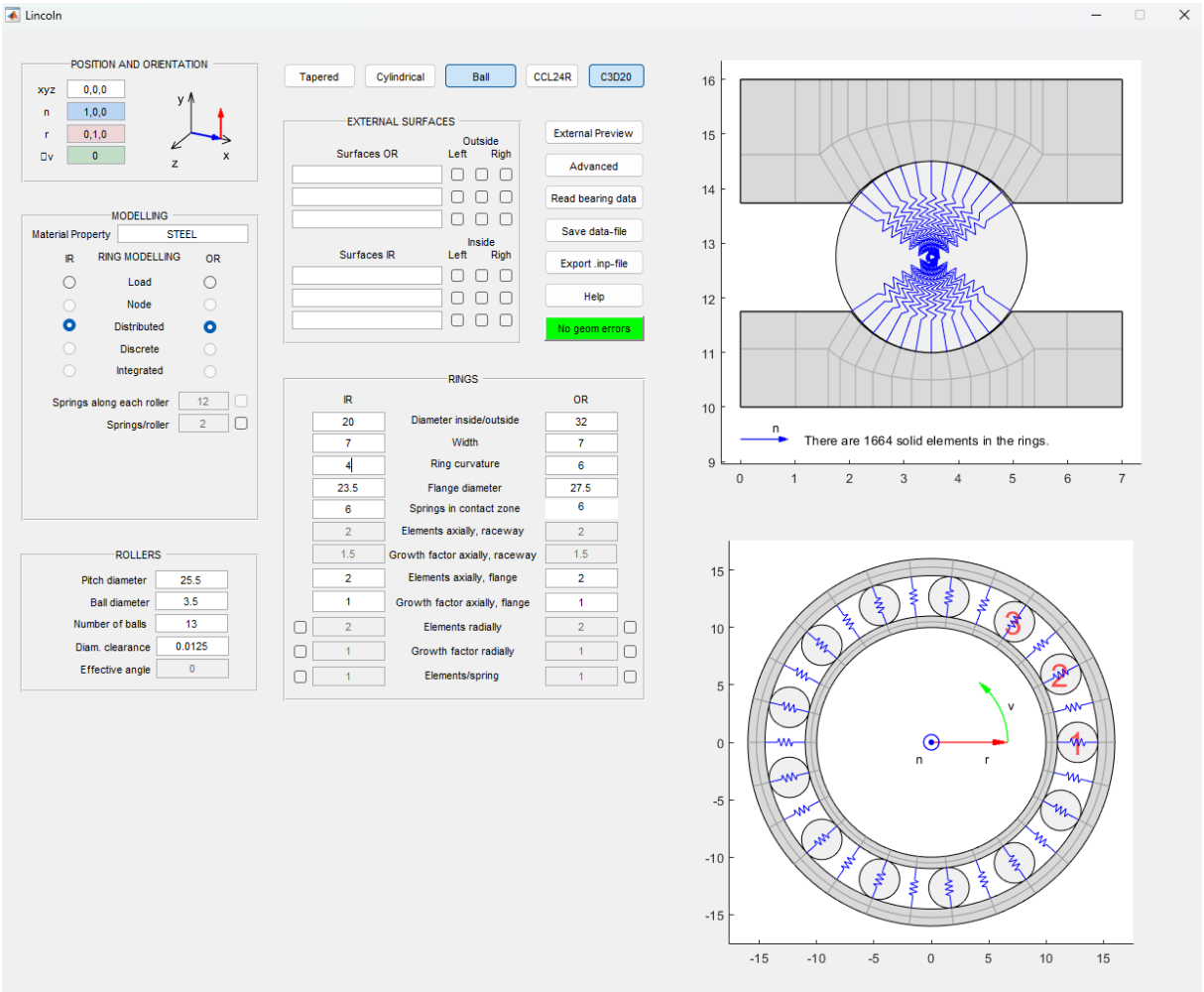

Figure 8.2: Lincoln GUI

8.4 Appendix D

```
clear all
close all
clc

% Harris (2201) theory implemented to calculated deep groove
   ball bearing deflections. Written 2025-03-20 by Arvid
   Angel & Jonathan Cederquist.

%% Bearing geometry input
bearing_name = "6216";
D = 17.462;              % ball diameter
ri = D / 2 *1.04;        % inner groove radius
ro = D / 2 *1.06;        % outer groove radius
dm = 111.7;              % pitch diameter
beta = 0;                % ball bearing angle
Q = [36400 18200 9100 4550 2275]; % bearing radial load cases
dx_SABR = [108.43 70.64 46.82 31.80 22.33]./1000; % SABR
   reference

%% Theory implemented
fi = ri / D;       % ratio inner raceway
fo = ro / D;       % ratio outer raceway
gamma = D * cos(beta) / dm;    % ratio

sumpi = 1/D*(4 - 1/fi + 2*gamma/(1-gamma));
sumpo = 1/D*(4 - 1/fo - 2*gamma/(1+gamma));

Fpi = (  1/fi + 2*gamma/(1-gamma)   )/(   4 - 1/fi + 2*gamma
   /(1-gamma)   );
Fpo = (  1/fo - 2*gamma/(1+gamma)   )/(   4 - 1/fo - 2*gamma
   /(1+gamma)  );

dimensionless_contact_parameters = [0 0.1075 0.3204 0.4795
   0.5916 0.6716 0.7332 0.7948 0.83495 0.87366 0.90999
   0.93657 0.95738 0.97290 0.983797 0.990902 0.995112
   0.997300 0.9981847 0.9989156 0.9994785 0.9998527 1;
1 1.0760 1.2623 1.4556 1.6440 1.8258 2.011 2.265 2.494 2.800
   3.233 3.738 4.395 5.267 6.448 8.062 10.222 12.789 14.839
   17.974 23.55 37.38 inf;
1 0.9318 0.8114 0.7278 0.6687 0.6245 0.5881 0.5480 0.5186
   0.4863 0.4499 0.4166 0.3830 0.3490 0.3150 0.2814 0.2497
   0.2232 0.2072 0.18822 0.16442 0.13050 0;
1 0.9974 0.9761 0.9429 0.9077 0.8733 0.8394 0.7961 0.7602
   0.7169 0.6636 0.6112 0.5551 0.4960 0.4352 0.3745 0.3176
   0.2705 0.2427 0.2106 0.17167 0.11995 0]';
```

```
%% inner raceway interpolation of delta_star
x = dimensionless_contact_parameters(:, 1);
y = dimensionless_contact_parameters(:, 4);
x_input = Fpi;

delta_star_i = interp1(x, y, x_input, 'linear');

%% outer raceway interpolation of delta_star

x_input = Fpo;
delta_star_o = interp1(x, y, x_input, 'linear');

% Harris (2001, s.235)
% inner
Kpi = 2.15 * 10^5 * sumpi^-0.5 * delta_star_i^(-3/2);
% outer
Kpo = 2.15 * 10^5 * sumpo^-0.5 * delta_star_o^(-3/2);
% combined
Kn = (1  /  (  (1/Kpi)^(1/1.5)  +  (1/Kpo)^(1/1.5)  )  )^1.5;

dx_harris = (Q./Kn).^(2/3) ./2;    % calculated displacement

%% plot data comparing the calculated value with SABR
   reference
figure()
plot(Q, dx_harris, '-b','LineWidth'.2)
xlabel("Force [N]")
ylabel("Displacement [mm]")
title("SKF " + bearing_name)
hold on
plot(Q, dx_SABR, '-r', 'LineWidth'.2)
legend("Harris (2001) analytical solution", "SABR " +
   bearing_name + " reference")
```

8.5 Appendix E

Table 8.2: Deep Groove Ball Bearing Geometries. Bearing 6020, 6210, and 6010 have some cells denoted with xx. This is because they were excluded from the curve fit approach detailed in section 3.9.

SKF bearing	**6216**	**6212**	**6020**	**6210**	**6012**	**6010**	**6008**	**6204**
Bore [mm]	80	60	100	50	60	50	40	20
Outer Diameter [mm]	140	110	150	90	95	80	68	47
Width [mm]	26	22	24	20	18	16	15	14
Dynamic Load Rating, C [N]	72800	55300	63700	37100	30700	22900	17800	13500
Ball Diameter [mm]	17.462	15.875	15.081	12.7	10.319	8.731	7.938	7.938
Pitch Diameter [mm]	111.7	85	125	70	77.5	65	54	33.5
Number of Balls	12	10	15	10	14	14	12	8
Radial Play [mm]	0.3219	0.2861	0.2724	0.2338	0.1859	0.1569	0.1434	0.1457
Effective Diametrical Clearance [mm]	0.0104	0.0084	0.0128	0.0065	0.0084	0.0065	0.005	0.0053
Inner Curvature [%]	4	4	4	4	4	4	4	4
Outer Curvature [%]	6	6	6	6	6	6	6	6
Stiffness [N/mm] / displacement at highest loadcase [mm^-3]	22255 / 108.43	19016 / 104.2	xx / xx	xx / xx	8027.2 / 66.81	xx / xx	5126 / 54.97	5562.3 / 59.81
Stiffness [N/mm] / displacement at lowest loadcase [mm^-3]	4242.7 / 22.33	3460.6 / 20.66	xx / xx	xx / xx	1621.4 / 14.74	xx / xx	950.3 / 11.18	1016.4 / 12.1

8.6 Appendix F

```
% Hamrock theory implemented to calculated deep groove ball
   bearing deflections. Written by Arvid Angel & Jonathan
   Cederquist.

gamma = BD.Droll / BD.pitchD; % beta = 0
fe = (BD.Droll * 0.5 * 1.06) / BD.Droll;
fi = (BD.Droll * 0.5 * 1.04) / BD.Droll;
q = pi/2 - 1;
E = 210*10^3; % Steel ball

Rxi = (1 - gamma) * BD.Droll / 2;
Rxe = (1 + gamma) * BD.Droll / 2;
Ryi = fi * BD.Droll / (2*fi - 1);
Rye = fe * BD.Droll / (2*fe - 1);

alpha_inner = Ryi / Rxi;
alpha_outer = Rye / Rxe;

kappa_outer = alpha_inner^(2/pi);
kappa_inner = alpha_outer^(2/pi);

R_inner = 1 / (1/Rxi + 1/Ryi);
R_outer = 1 / (1/Rxe + 1/Rye);

elliptic_intergral_firstkind_inner = pi / 2 + q * log(
   alpha_inner);
elliptic_intergral_firstkind_outer = pi / 2 + q * log(
   alpha_outer);

elliptic_intergral_secondkind_inner = 1 + q / alpha_inner;
elliptic_intergral_secondkind_outer = 1 + q / alpha_outer;

Ke = pi / 3 * kappa_outer * E * sqrt((2 *
   elliptic_intergral_secondkind_outer * R_outer) / (
   elliptic_intergral_firstkind_outer^3));
Ki = pi / 3 * kappa_inner * E * sqrt((2 *
   elliptic_intergral_secondkind_inner * R_inner) / (
   elliptic_intergral_firstkind_inner^3));

% Compute equivalent stiffness
Kn = 1/(((1 / Ki)^(2/3) + (1 / Ke)^(2/3))^(3/2));

% Distribute per spring
Kn = Kn/BD.sp_c/BD.IR_el_05cz;
```

```
x = linspace(0.2.0.40);

Q = Kn.*(x.^3/2);
% assembles and adds extreme values
xF = [-x 1;-Q 100/(BD.IR_el_05cz*2+1)/BD.sp_c];
```

8.7 Appendix G

```
*INCLUDE, INPUT=6216_harris.inp
**
*NODE
       1000000,         13, 0, 0
    2000000,       15,   0,    0
**
**
**
**
** KINEMATIC/DISTRIBUTING COUPLING
**
*COUPLING, CONSTRAINT NAME=COUPLING_961, REF NODE=1000000, SURFACE=Inner_s
*KINEMATIC
       1,        6
*COUPLING, CONSTRAINT NAME=COUPLING_962, REF NODE=2000000, SURFACE=Outer_s
*KINEMATIC
       1,        6
**
**
**
**
** MATERIALS
**
**
**STEEL
**
*MATERIAL, NAME=STEEL
*DENSITY
                7.85E-9,
*ELASTIC, TYPE=ISOTROPIC
                210000.,                      0.3
**
**
**
**
**
** BOUNDARY
**
*BOUNDARY, TYPE=DISPLACEMENT
    2000000,        1,        6,      0.
       1000000,        4,     6,      0.
**
** STEPS
**
**
*STEP, NAME=misalignment, INC=100, NLGEOM=YES
```

```
*STATIC
                    0.2,                         1.,                      0.001,
**
*BOUNDARY, TYPE=DISPLACEMENT
       1000000,       5,        5,           0e-3
       1000000,       6,        6,           0e-3
*OUTPUT, FIELD
*CONTACT OUTPUT
CDISP,
CSTRESS,
*NODE OUTPUT
U,
*ELEMENT OUTPUT, DIRECTIONS=YES
E,
S,
*NODE PRINT, FREQUENCY = 20000
U1, U2, U3
*OUTPUT, FIELD, VARIABLE=PRESELECT
*OUTPUT, HISTORY, VARIABLE=PRESELECT
*END STEP
**
**
** STEP 1
**
*STEP, NAME=preload, INC=100, NLGEOM=YES
*STATIC
                    0.2,                         1.,                      0.001,
**
** CLOAD
**
*CLOAD
       1000000,       2,           100
*OUTPUT, FIELD
*CONTACT OUTPUT
CDISP,
CSTRESS,
*NODE OUTPUT
U,
*ELEMENT OUTPUT, DIRECTIONS=YES
E,
S,
NFORC,
*NODE PRINT, FREQUENCY = 20000
U1, U2, U3
*OUTPUT, FIELD, VARIABLE=PRESELECT
*OUTPUT, HISTORY, VARIABLE=PRESELECT
*END STEP
**
```

```
** STEP 1
**
*STEP, NAME=Step1, INC=100, NLGEOM=YES
*STATIC
                    0.2,                          1.,                    0.001,
**
** CLOAD
**
*CLOAD
       1000000,       2,           2275
*OUTPUT, FIELD
*CONTACT OUTPUT
CDISP,
CSTRESS,
*NODE OUTPUT
U,
*ELEMENT OUTPUT, DIRECTIONS=YES
E,
S,
NFORC,
*NODE PRINT, FREQUENCY = 20000
U1, U2, U3
*OUTPUT, FIELD, VARIABLE=PRESELECT
*OUTPUT, HISTORY, VARIABLE=PRESELECT
*END STEP
**
** STEP 2
**
*STEP, NAME=Step2, INC=100, NLGEOM=YES
*STATIC
                    0.2,                          1.,                    0.001,
**
** CLOAD
**
*CLOAD
       1000000,       2,           4550
*OUTPUT, FIELD
*CONTACT OUTPUT
CDISP,
CSTRESS,
*NODE OUTPUT
U,
*ELEMENT OUTPUT, DIRECTIONS=YES
E,
S,
NFORC,
*NODE PRINT, FREQUENCY = 20000
U1, U2, U3
```

```
*OUTPUT, FIELD, VARIABLE=PRESELECT
*OUTPUT, HISTORY, VARIABLE=PRESELECT
*END STEP
**
** STEP 3
**
*STEP, NAME=Step3, INC=100, NLGEOM=YES
*STATIC
                    0.2,                          1.,                    0.001,
**
** CLOAD
**
*CLOAD
       1000000,       2,           9100
*OUTPUT, FIELD
*CONTACT OUTPUT
CDISP,
CSTRESS,
*NODE OUTPUT
U,
*ELEMENT OUTPUT, DIRECTIONS=YES
E,
S,
NFORC,
*NODE PRINT, FREQUENCY = 20000
U1, U2, U3
*OUTPUT, FIELD, VARIABLE=PRESELECT
*OUTPUT, HISTORY, VARIABLE=PRESELECT
*END STEP
**
** STEP 4
**
*STEP, NAME=Step4, INC=100, NLGEOM=YES
*STATIC
                    0.2,                          1.,                    0.001,
**
** CLOAD
**
*CLOAD
       1000000,       2,           18200
*OUTPUT, FIELD
*CONTACT OUTPUT
CDISP,
CSTRESS,
*NODE OUTPUT
U,
*ELEMENT OUTPUT, DIRECTIONS=YES
E,
```

```
S,
NFORC,
*NODE PRINT, FREQUENCY = 20000
U1, U2, U3
*OUTPUT, FIELD, VARIABLE=PRESELECT
*OUTPUT, HISTORY, VARIABLE=PRESELECT
*END STEP
**
** STEP 5
**
*STEP, NAME=Step5, INC=100, NLGEOM=YES
*STATIC
                    0.2,                          1.,                    0.001,
**
** CLOAD
**
*CLOAD
       1000000,       2,           36400
*OUTPUT, FIELD
*CONTACT OUTPUT
CDISP,
CSTRESS,
*NODE OUTPUT
U,
*ELEMENT OUTPUT, DIRECTIONS=YES
E,
S,
NFORC,
*NODE PRINT, FREQUENCY = 20000
U1, U2, U3
*OUTPUT, FIELD, VARIABLE=PRESELECT
*OUTPUT, HISTORY, VARIABLE=PRESELECT
*END STEP
**
**
```